METHOD DEVELOPMENT TO STUDY THE RESPONSE OF AGED ENDOTHELIAL CELLS TO FLOW USING HUTCHINSON GILFORD PROGERIA PATIENT-DERIVED PLURIPOTENT STEM CELLS

by

Ariane Beland
B. Eng. McGill University, 2016

A THESIS SUBMITTED IN PARTIAL FULFILLMENT OF
THE REQUIREMENTS FOR THE DEGREE OF
MASTER OF ENGINEERING

in

Chemical Engineering
MCGILL UNIVERSITY
(Montréal)

July 2021

ABSTRACT

Aged arteries experience wall thickening, accumulation of plaque and calcification, which are hallmarks of atherosclerosis, an inflammatory disease that causes lesions in arteries. Atherosclerotic plaques can impede flow or detach, potentially leading to severe or even fatal consequences such as cardiac arrest or stroke. Endothelial dysfunction is thought to be an initiating event of atherosclerosis. Atheroprone segments of the vasculature are found in regions of disturbed and turbulent blood flow. Moreover, endothelial cells (ECs) align in the direction of blood flow when exposed to undisturbed laminar wall shear stress. Current methods of studying vascular aging, involving rodents, vascular biopsies from elderly patients and serially passaged ECs are severely limited. Alternatively, accelerated aging diseases such as Hutchinson-Gilford Progeria Syndrome (HGPS) can be used to model vascular aging since they share a lot of similarities. HGPS is caused by a mutation on the gene coding for Lamin A leading to the accumulation of progerin at the nuclear envelope. Vascular cells of HGPS patients are difficult to obtain due to the rarity of the disease and the invasiveness of vascular biopsies. Induced pluripotent stem cell (iPSC) technology allows for the use of somatic cells like fibroblasts that carry the HGPS mutation to be reprogramed to a stem cell state, expanded, and then differentiated into ECs for investigation. Current research featuring these techniques however use traditional static cell culture methods that fail to capture functional defects by neglecting hemodynamic forces experienced by ECs from blood flow. This thesis sought to fill this gap in research by developing a series of methods to investigate the response to shear stress of ECs derived from iPSCs of HGPS patients. The first aim consisted of using a differentiation protocol by Sahara *et al.* to obtain ECs from HGPS-iPSCs, which was found to have an efficiency slightly below 20% via flow cytometry. The resulting ECs were found to be positive for von Willebrand Factor via immucytochemistry. Next, a reliable staining protocol was developed to detect the accumulation of progerin in cells using HGPS fibroblasts as positive controls and use image analysis to assess nuclear deformation. This technique led to the surprising finding that HGPS-iPSC-ECs did express progerin, contrary to most published research suggesting that the expression occurs mainly in VSMCs. Subsequently, using a parallel-plate flow chamber system, HSVECs and HUVECs were exposed shear stress. Alignment after 6 hours at 22 dyn/cm^2 of shear stress was quantified using actin filament staining and Directionality analysis, as well as nuclear staining with shape and orientation

measurements. It was found that both types of ECs aligned in the direction of the flow, and that the image analysis methods chosen were highly reproducible between flow chamber experiments. Lastly, inflammation in response to shear stress exposure in the flow chamber was assessed by developing a leukocyte adhesion model using the perfusion of NB4 cells and counting the cells adhered to the EC monolayer. Inflammation was further examined by interleukin-6 and interleukin-11 cytokine quantification via enzyme-linked immunosorbent assays and using a lactate dehydrogenase cytotoxicity assay on media samples from the perfusion. The results from these assays suggest that due to the low ratio of ECs to perfused liquid volume, future attempts at quantifying inflammation should instead focus on immunocytochemistry for inflammation markers. The stage has been set for future work implementing this platform to study dynamic responses of HGPS-iPSC-ECs to hemodynamic stimuli. The unique combination of methods developed in this thesis constitutes a powerful new tool to study the behaviour of aged human ECs under flow.

RÉSUMÉ

Avec l'âge, les artères s'épaississent, se calcifient et accumulent de la plaque. Ce remodelage est typique de l'athérosclérose, une maladie inflammatoire causant des lésions artérielles. La dysfonction endothéliale est un élément déclencheur de l'athérosclérose. Les plaques d'athérome peuvent obstruer la circulation sanguine ou se rompre provoquant ainsi de dangereuses complications telles que les crises cardiaques et les accidents vasculaires cérébraux. Elles se trouvent principalement dans les régions de la vasculature ou le flux est turbulent. D'ailleurs les cellules endothéliales (CE) s'alignent sous la contrainte de cisaillement de flux laminaire. Les méthodes actuelles pour étudier le vieillissement vasculaire sont souvent limités aux rongeurs, à des biopsies vasculaires de patients âgés et aux CE aux nombres de passages élevés. Hors, les maladies de vieillissement accéléré telles que la progéria, ou syndrome de Hutchinson-Gilford (HGPS), peuvent être utilisées comme modèle de vieillissement vasculaire. La progéria est une maladie génétique rare due à une mutation du gène conditionnant la synthèse de la lamine A causant l'accumulation de progérine à l'enveloppe nucléaire. Il est difficile d'obtenir des CE de patients ayant la progéria puisque la maladie est rarissime et que les biopsies vasculaires sont plutôt invasives. Les cellules souches pluripotentes induites (CSPi) permettent l'investigation de CE « vieillies » en utilisant des fibroblastes HGPS reprogrammés en cellules souches qui sont ensuite différenciées. Toutefois, les recherches exploitant cette approche sont pour la plupart limitées à l'usage de techniques de culture statiques qui négligent les impacts fonctionnels des forces hémodynamiques sur les CE. L'objectif de ces travaux était ainsi de remédier à cette lacune en développant un ensemble de méthodes pour étudier la réponse au cisaillement de CE obtenues à partie de CSPi-HGPS. Dans un premier lieu, des CE ont été obtenues à partir de CSPi, grâce à un protocole par Sahara *et al.*, avec une efficacité légèrement sous les 20% selon la cytométrie en flux. Les cellules différenciées contenaient le facteur de von Willebrand lors d'expériences immunohistochimiques. Ensuite, la mise en place d'un protocole de détection de la progérine par immunofluorescence a permis la quantification de la déformation nucléaire de cellules contenant de la progérine par analyse d'image avec des fibroblastes HGPS comme contrôles positifs. Cette technique a aussi confirmé que les CE de CSPi-HGPS accumulaient la progérine, même si la plupart des publications à ce sujet suggéraient que la progérine était principalement détectée dans cellules musculaires lisses vasculaires plutôt que dans les CE.

Dans un deuxième lieu, une chambre de flux a été employée pour exposer des CE de veine saphène et de veine ombilicale à une contrainte de cisaillement à la paroi de 22 dyn/cm^2 pour 6 heures. L'alignement des CE a été quantifié en analysant la direction des filaments d'actine, et en examinant la forme et l'orientation des noyaux. Les deux types de CE se sont alignées dans la direction du flux, et la reproductibilité des méthodes d'analyse a été validée. Puis, la réponse inflammatoire des CE exposées au cisaillement a été étudié grâce à un modèle d'adhésion leucocytaire impliquant la perfusion de cellules NB4 dans la chambre de flux. À partir d'échantillons de milieu, les interleukines 6 et 11 ont été quantifiées par méthode immuno-enzymatique ELISA et les déshydrogénases lactiques ont été mesurés pour évaluer la cytotoxicité. Ces expériences ont suggéré que le nombre de CE était trop bas pour le volume de liquide perfusé dans le système de chambre de flux. Par conséquent, les expériences futures devraient plutôt se centrer sur l'immunohistochimie de marqueurs inflammatoires. Pour conclure, la combinaison unique des méthodes développée pour cette thèse constitue une plateforme prometteuse pour l'étude du vieillissement des CE sous flux.

STATEMENT OF CONTRIBUTIONS

Ariane V. Beland performed all the experiments and data analysis presented in this thesis based on prior work by Jonathan Brassard on iPSC differentiation into endothelial cells and by Corinne A. Hoesli on the design of a parallel-plate flow chamber system, with the exception of leukocyte adhesion studies, which were performed with Marième D. Boulanger. In addition to the thesis hereby presented, AVB contributed to the redaction of four manuscripts:

"Bags versus flasks: a comparison of cell culture systems for the production of dendritic cell–based immunotherapies" was a literature review published in 2018 in *Transfusion* 58 (7): 1800-1813, Copyright © 2018 by Wiley Periodicals, Inc. on behalf of AABB. Authors: Natalie Fekete Ariane V. Beland Katie Campbell Sarah L. Clark Corinne A. Hoesli[1]. **AVB contributions:** visualization, writing – review and editing.

"Dynamics of Endothelial Cell Responses to Laminar Shear Stress on Surfaces Functionalized with Fibronectin-Derived Peptides" was published in 2018 in *ACS Biomaterials Science and Engineering* 4 (11): 3779-3791, Copyright © 2018 American Chemical Society. Authors: Corinne A. Hoesli, Catherine Tremblay, Pierre-Marc Juneau, Marième D. Boulanger, Ariane V. Beland, Si Da Ling, Bruno Gaillet, Carl Duchesne, Jean Ruel, Gaétan Laroche, Alain Garnier[2]. **AVB contributions:** methodology, investigation, formal analysis, visualization and writing – review and editing.

"Protein film formation on cell culture surfaces investigated by quartz crystal microbalance with dissipation monitoring and atomic force microscopy" was published in November 2019 in *Colloids and Surfaces B: Biointerfaces* 183, Copyright © 2019 Elsevier. Authors: Andreas Wargeneau, Natalie Fekete, Ariane V. Beland, Gad Sabbatier, Olivia M. Bowden, Marième D. Boulanger, Corinne A. Hoesli[3]. **AVB contributions:** methodology, investigation, formal analysis, visualization and writing – original draft, review and editing.

"Closing the system: production of viral antigen-presenting dendritic cells eliciting specific CD8+ T cell activation in fluorinated ethylene propylene cell culture bags" was published in October 2020 in the *Journal of translational Medicine* 18 (1): 383, Copyright © 2020 Springer. Authors: Jean-Philippe Bastien, Natalie Fekete, Ariane V. Beland, Marie-Paule Lachambre, Veronique Laforte, David Juncker, Vibhuti Dave, Denis-Claude Roy, Corinne A. Hoesli[4]. **AVB contributions:** investigation, methodology and formal analysis.

TABLE OF CONTENTS

LIST OF FIGURES

LIST OF TABLES

NOMENCLATURE

ATRA	All-trans retinoic acid
bFGF	Basic fibroblast growth factor
BMP-4	Bone morphogenic protein-4
BSA	Bovine serum albumin
CD	Cluster of differentiation
DAPI	4',6-diamidino-2-phenylindole
DAPT	N-[(3,5-Difluorophenyl)acetyl]-L-alanyl-2-phenyl]glycine-1, 1-dimethylethyl ester
EBM-2	Endothelial basal media
EC	Endothelial cell
ECM	Extra cellular matrix
EDTA	Ethylenediaminetetraacetic acid
EGF	Epidermal growth factor
eNOS	Endothelial nitric oxide synthase
EPC	Endothelial progenitor cell
ESC	Embryonic stem cell
FBS	Fetal bovine serum
HGPS	Hutchinson Gilford Progeria Syndrome
HSD	Honestly significant difference
HSVEC	Human saphenous vein endothelial cell
HUVEC	Human umbilical vein endothelial cell
IGF-1	Insulin-like growth factor 1
IL	Interleukin
iPSC	Induced pluripotent stem cell
KDE	Kernel density estimate
KDR	Kinase insert domain receptor
LDH	Lactate dehydrogenase
LMNA	Lamin A gene
MAPK	Mitogen-activated protein kinases
MGV	Mean gray value
NADH	Reduced nicotinamide adenine dinucleotide
NF-κB	Nuclear factor kappa-light-chain enhancer of activated B cells
NO	Nitric oxide
OSKM	Oct4, Sox2, Klf4 and c-Myc
PBMC	Peripheral blood mononuclear cells
PBS	Phosphate Buffered saline
VEGF	Vascular endothelial growth factor
VSMC	Vascular smooth muscle cells
vWF	von Willebrand Factor
ELISA	Enzyme-linked immunosorbent assay

Symbols

τ	Wall shear stress
Q	Volumetric flowrate
μ	Kinematic viscosity
W	Width of flow chamber
H	Height of space between parallel plates

ACKNOWLEDGEMENTS

First, I would like to acknowledge that McGill University is situated on the traditional territory of the Kanien'kehà:ka, a place which has long served as a site of meeting and exchange amongst nations. I recognize and respect the Kanien'kehà:ka as the traditional custodians of the lands and waters on which this work was conducted. Thank you to Stephanie Fernandez for helping me realize my privilege and my responsibility to contribute to a more diverse, equitable and inclusive community.

I am sincerely thankful to have had Prof. Corinne Hoesli as my supervisor during my undergraduate and master's studies. She introduced me to a field of research where my curiosity for biology could co-exist with my engineering and problem-solving interests. Joining her lab in 2015 was a turning point in my journey. Prof. Hoesli's guidance, and mainly her trust in my abilities as a researcher, truly helped shape who I am today. She believed in me more than I did myself at times and never stopped supporting me. I have found in her a mentor for life. I am also grateful to have worked with Dr. Natalie Fekete, who guided me through my first years in the lab. Her experience and work ethic truly inspired me. Ich danke Ihnen von ganzem Herzen.

Thank you to the members of the Stem Cell Bioprocessing Laboratory for helping me shape this work in so many ways. Dr. Andreas Wargeneau showed me how to use critical thinking and intense discussions to devotedly learn in research. Lisa Danielczak's support and guidance were instrumental in my journey. Without Jonathan Brassard's previous projects, I could not have completed this thesis. I would also like to thank my friend and colleague Marième Boulanger for all the laughs and efforts we put in our work together. I was fortunate to work with diligent and caring individuals like Raymond Tran, Omar Bashth, Mohamed A. Elkhodiry, Olivia Bowden and Julia Manalil.

I am grateful to have been surrounded by my best friends Julia, Caroline, Kayley, KC and Katie, who have made me feel loved and grounded through all the highs and lows. Finally, I am indebted to my mother Élizabeth and my grandmother Suzanne for being my source of motivation, my inspiration and my safe haven.

1. INTRODUCTION

Cardiovascular diseases are broadly defined as disorders of the heart and blood vessels that represent the leading cause of mortality in the world[5]. It is estimated that cardiovascular diseases cause 31% of all global deaths[5] and claim over 52,500 Canadian lives in 2019[6]. In addition to contributing to mortality and morbidity, cardiovascular diseases represent a major economic burden. In 2016, the Heart and Stroke™ Foundation estimated the costs of heart failure alone in Canada to be around 2.8 billion CAD per year[7]. The societal drain caused by cardiovascular diseases is likely to continue to increase due to the growing rates of risk factors such as obesity and, more importantly, the aging of populations[5,8]. The 2016 census data highlights this since, for the first time, the Canadian population aged 65 and above exceeded the number of children under 15 years[9].

Age correlates with the incidence of chronic diseases. Even in seemingly healthy individuals, risks of developing cardiovascular diseases increase with age-related changes in vascular function and structure. Tissues forming blood vessels experience a great deal of biomechanical stress and strain[10]. Arterial aging causes remodeling of these vessels leading to vessel stiffening and reduced compliance[11,12]. Inflammation, calcification and increased matrix deposition are hallmarks of both vascular aging and atherosclerosis, a important inflammatory disease linked to vascular pathologies[11–14]. Endothelial dysfunction is an initiating event of atherosclerosis. Molecular mechanisms in aging vascular cells and biomechanics from blood flow are intimately related when it comes to phenotypic and functional changes occurring in cardiovascular diseases. An improved understanding of this interplay could lead to the development of more effective therapies or targeted treatments in the context of aging.

In vitro models are an essential tool in biogerontology to gain insight into the molecular and biological mechanisms involved in vascular aging and atherosclerosis. Cellular models of accelerated aging have been useful when examining age-related vascular deterioration[14]. As reviewed elsewhere[14–17], accelerated aging disorders such as Hutchinson-Gilford progeria syndrome (HGPS) can provide useful insight into mechanisms of cellular aging and senescence. HGPS is a rare laminopathy with only 179 afflicted individuals identified worldwide[18]. On average, children with progeria die of atherosclerosis and associated cardiovascular complications in their teenage years[14,19]. Given the molecular and phenotypic similarities between this

accelerated aging disease and normal aging, understanding the mechanisms leading to vascular dysfunction in HGPS can help identify methods to prevent or treat progeria and age-related vascular diseases[14,20]. Access to cells harbouring the HGPS mutation remains limited by the rarity and young age of potential tissue donors, as well as the invasiveness of biopsies. Induced pluripotent stem cells (iPSCs) from HGPS patients offer an appealing alternative given their theoretically unlimited expansion potential and capacity to differentiate into any somatic cell type in the adult human body, including vascular lineages such as endothelial cells (ECs). However, most existing *in vitro* studies using ECs derived from HGPS-iPSCs (HGPS-iPSC-ECs) using this approach neglect to consider flow-induced stress present in blood vessels. This thesis seeks to improve current vascular aging models by developing reproducible methods of investigating the response to shear stress of ECs in the context of vascular aging. Only one study has been published so far investigating specifically HGPS-ECs under biologically-relevant shear-stress using 3D tissue-engineered blood vessels[20]. This thesis aims to complement this research using a different platforms. Using HGPS patient-derived iPSCs to obtain ECs in combination with a parallel-plate flow chamber system is a completely novel endeavour. Robust methods of assessing the response to flow of these cells also need to be implemented to compare healthy and aged samples. In the future, such a platform could help not only gain mechanistical insight into vascular aging, but also serve as a model to test potential treatments and drugs.

2. LITERATURE REVIEW

CARDIOVASCULAR AGING

Cardiovascular System Overview

The cardiovascular system is comprised of the blood, the heart and its vasculature, also called blood vessels, which include veins, arteries and capillaries[21]. As illustrated in **Figure 1**, all blood vessels aside from capillaries have the same basic structure consisting of an outer layer, a middle layer, and an inner respectively called *tunica externa* or *adventitia, tunica media* and *tunica intima*[21]. Veins are larger in diameter than arteries, but their vessel walls are thinner and less rigid. The outermost layer, the *tunica externa* or *adventitia*, serves as structural support for the vessel and is thus mainly composed of connective tissue including collagen fibers and some elastic fibers, as well as longitudinally-oriented vascular smooth muscle cells

(VSMCs)[21]. The *tunica media* provides both muscular support and elastic stretch to the vessel. It is formed by circumferentially-oriented VSMCs and elastic fibers. For arteries, this layer is the thickest and more clearly organized in multiple layers of VSMCs separated by the elastic lamina[22]. The tunica intima is the layer closest to the lumen. It mainly consists of the endothelium, formed by ECs, which are in direct contact with the blood. In arteries, the endothelium lies on a supportive matrix of connective tissue composed of collagen and elastic fibers called the basal lamina[21,22]. Veins have specialized valve structures that extend into the lumen to prevent blood backflow. Arterial ECs are thicker than venous ones; they are also longer, narrower and aligned in the direction of laminar blood flow. This is due to physiological venous shear stress being lower than arterial shear stress (1-5 dyn/cm^2 versus 10-40 dyn/cm^2)[21]. Capillaries consist only of ECs and a basal lamina, with scattered pericytes, which are contractile cells[22].

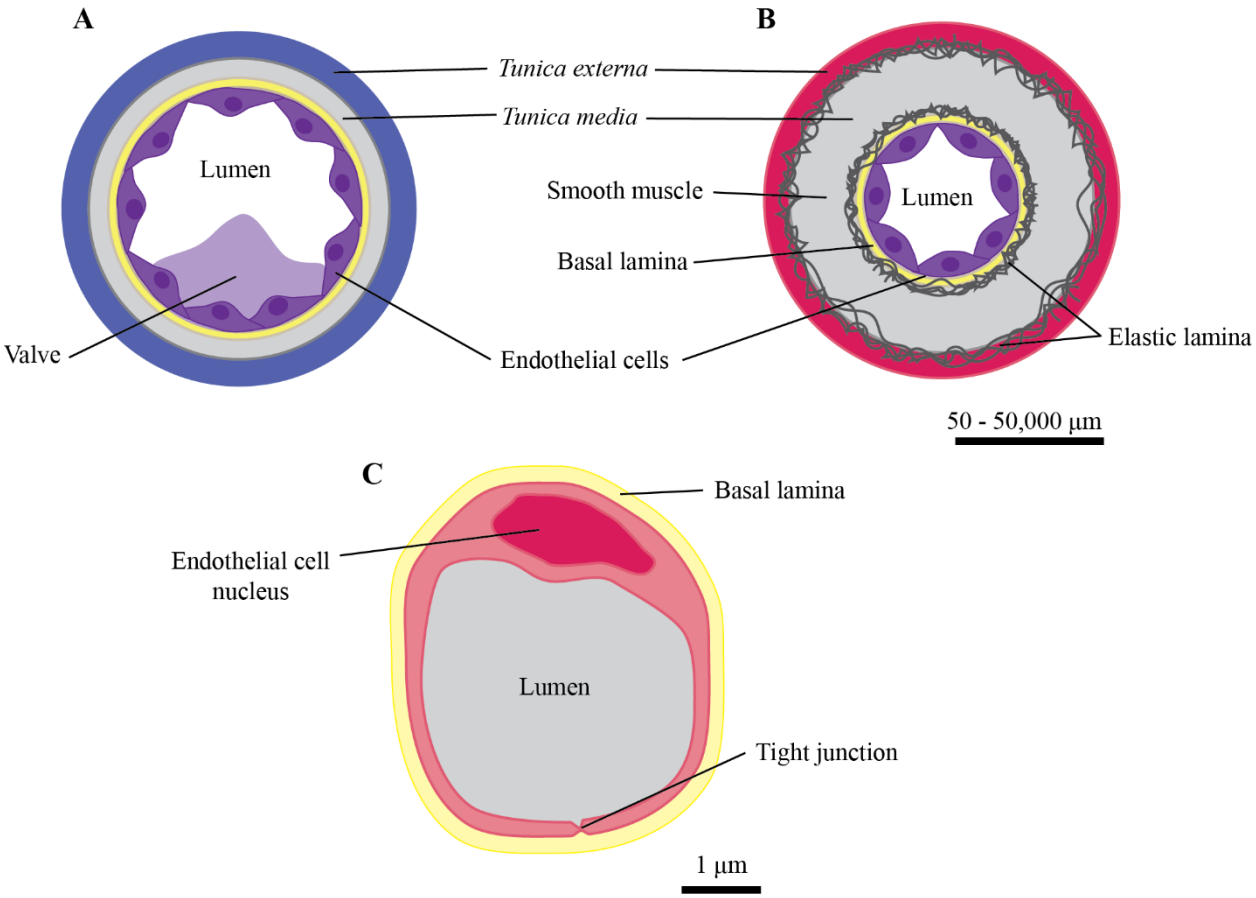

Figure 1: *Schematic cross-section of blood vessels*: veins (A), elastic arteries (B) and capillaries (C).

Endothelial function varies according to the vessel type and the location[23]. For instance, vascular tone defined by the degree of a vessel's constriction compared to it maximally dilated

state, is an arterial function that occurs primarily at the level of the arterioles[21]. Vasodilators and vasoconstrictors cause the VSMCs in the *tunica media* to relax and contract, respectively, in order to lower and raise the blood pressure. Molecules such as nitric oxide, bradykinin, and adenosine are considered vasodilators, while endothelin and angiotensin II are vasoconstrictors[21]. Another important function of the endothelium is the migration of leukocytes circulating in blood to underlying tissues. This mainly takes place in post-capillary venules due to lower flow rate, thinner walls, and fewer tight junctions compared to arterial vessels[21]. The initial attachment and rolling of the leukocytes is mediated by glycoprotein ligands on the surface of immune cells interacting with selectin proteins on the surface of ECs "primed" by cytokines[21]. Firm adhesion, which is the next stage of leukocyte migration, involves the interaction of integrins on leukocytes with adhesion molecules which are members of the endothelial immunoglobulin superfamily. Finally, transmigration of leukocytes appears to involve among others platelet endothelial cell adhesion molecule-1 (or CD31), the transmembrane protein CD99 and the junctional adhesion molecule-1[21,24–26].

Origin of Endothelial Cells

Blood supply in the body is imperative for the survival of almost all tissues. This blood supply depends on blood vessels and their creation, a process called vasculogenesis in the early embryo and angiogenesis for the subsequent growth and branching of vessels[22]. This process occurs mainly by the proliferation and movement of ECs. During embryonic development, the hemangioblast, a mesoderm-derived progenitor cell, gives rise to hematopoietic stem cells and angioblasts. Angioblasts can develop into ECs and possibly VSMCs[27]. Another pathway to obtain ECs is from endothelial precursor cells (EPCs) found in circulation and isolated from the spleen and bone marrow[27]. Understanding these pathways is essential in designing efficient directed differentiation protocols to obtain ECs from iPSCs.

Arteriovenous specification is thought to occur by the developmental expression of multiple genes encoding ligands, receptors and transcriptional factors summarized in Appendix A and in FIGRUE? of Appendix B. The signals for transcriptional regulation of EC specification are complex but a few key markers have been investigated. For the purposes of this thesis, the main concept of interest involved in both arterial and venous fate specification is vascular endothelial growth factor (VEGF or VEGF-A). VEGF is the main signalling

molecule in the endothelium. It is an endothelial mitogen and angiogenic factor, in addition to stimulating EC migration and survival, as well as controlling vessel permeability via the induction and maintenance of fenestrations[21,28–30]. In embryonic development, as well as in directed differentiation protocols VEGF signaling occurs via the VEGF receptor 2 and neuropilin-1 complex[21,31–33]. Identifying this complex is important for endothelial fate assessment, especially to confirm the adequacy of using iPSC-ECs as functional models of ECs.

Phenotype of Vascular Aging

Age is the dominant risk factor for coronary heart disease, congestive heart failure, hypertension and stroke. It is said that cardiovascular diseases are true diseases of aging[34]. This is primarily due to blood vessels being altered in structure and function through life[35]. Vascular aging is summarized by increased stiffness and decreased vessel compliance caused by a loss of endothelial control of vascular tone combined with vascular remodeling[14,36]. Endothelial dysfunction broadly encompasses the alteration of ECs their role in vascular homeostasis[36]. Endothelial dysfunction is thought to be an initiating event of atherosclerosis, which is ultimately an inflammatory disease leading to the formation of plaque or atheroma[37]. The atherosclerosis cascade of events is illustrated in **Figure 2**. Under normal conditions, circulating leukocytes adhere poorly to the healthy endothelium. However, when inflammation occurs, expression of molecules like vascular cell adhesion molecule 1 increases on ECs. During leukocyte attachment and rolling, pro-inflammatory cytokines expressed by the cells in the atheroma stimulate the leukocytes to migrate into the *tunica intima*[36,37]. For instance, monocyte chemoattractant protein-1 was identified as a molecule responsible for the emigration of monocytes into the lesion and macrophage colony-stimulating factor was found to direct differentiation of those monocytes into macrophage foam cells. Other pro-inflammatory signalling molecules perpetuate this cascade, including γ-interferon and lymphotoxin or tumor necrosis factor, which can not only stimulate leukocytes, but also ECs and VSMCs[37]. These activated cells then release fibrogenic factors causing the invasion of VSMCs in the subendothelial space, due to their growth and improved migration capacities. This leads to a reorganization of the extracellular matrix (ECM), defined as the non-cellular component of tissues and organs (crucial for scaffolding, biochemical and biomechanical cues)[38]. Consequently, the intimal medial thickness, usually measured by ultrasound, increases. As plaque accumulates, the lumen dilates to compensate[14]. However, the vessel decreases in elasticity with age, mainly due to the accumulation and crosslinking of collagen, in addition to the degeneration of elastic

fibers[38]. VSMCs in the medial section of the artery on the other hand, undergo apoptosis, causing a net decrease in arterial VSMC numbers, which is hypothesized to be the main trigger of calcification[39]. Ultimately, inflammation also precipitates the thrombotic complications of atherosclerotic plaques[36]. Activated macrophages present in the atheroma can produce proteolytic enzymes capable of degrading the collagen making up the fibrous cap protecting the plaque. Collagen renewal in VSMCs is also halted via γ-interferon secreted by T-lymphocytes. The lesions then find themselves susceptible to rupture. Finally, thrombosis is worsened by the presence of procoagulant molecules produced by leukocytes[37].

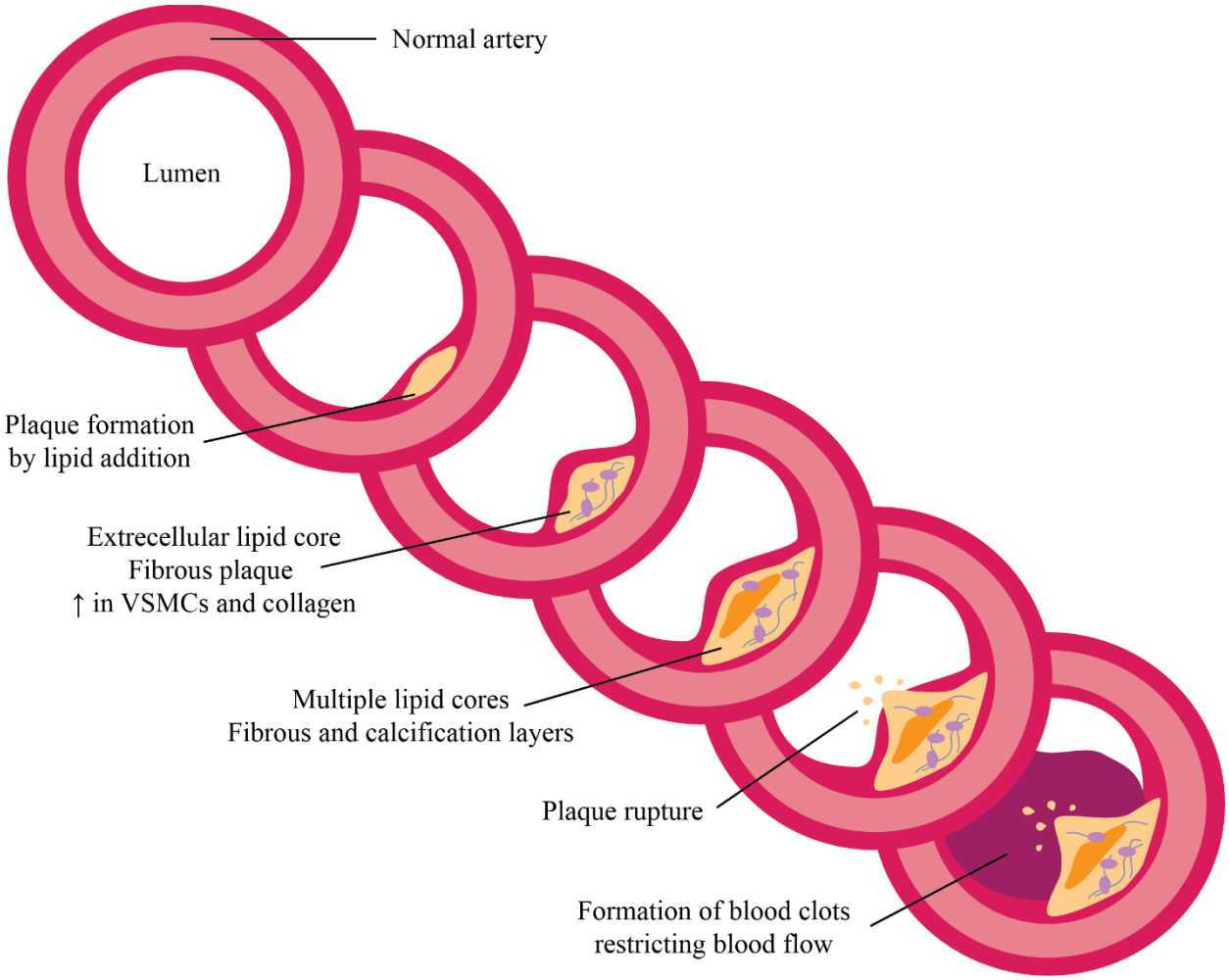

Figure 2: *Schematic of atherosclerosis progression adapted from Mayo Clinic[40]. VSMCs: vascular smooth muscle cells.*

To summarize, inflammation, calcification and increased matrix deposition are hallmarks of both vascular aging and atherosclerosis[13,14]. The decreased production of vasodilators such

as nitric oxide (NO), anticoagulants and anti-inflammatory molecules that indicate endothelial dysfunction constitute early signs of vascular aging[12,13,41]. Further proof that atherosclerosis and aging are related lies in the high number of senescent ECs observed in atherosclerotic plaques[42–44]. This is consistent with the high cell turnover rate in atheroma[42]. Telomere shortening can induce replicative senescence and shorter telomeres have been observed in aged ECs, as well as in the endothelium of atheroprone regions of the vasculature[42,43]. Replicative senescence is accelerated by certain genetic mutations (such as those found in HGPS), cell division, DNA damage, and oxidative stress[45]. In ECs, the glutathione-dependent antioxidant system normally plays an important role against oxidative stress and disruption of this redox cycle was found to accelerate telomeric erosion[46]. Cellular senescence can also be triggered independently of telomeres via DNA damage, mitogenic factors and chromatin changes or genomic instability caused by stress factors or inflammation[45]. Oxidative stress, leading to the prolonged exposure of macromolecules to reactive oxidizing species, is known to damage both genomic and mitochondrial DNA, in addition to depleting vasodilator NO[46].

Mechanotransduction: Endothelial Cells and Shear Stress

Mechanotransduction is defined as the mechanisms by which cell transduce mechanical stimuli into biochemical signals. This complex set of signals is summarized in **Figure 3**. Extracellular forces can stimulate stretch-sensitive ion channels, activate integrins and other focal adhesion proteins (through which the cell is anchored to the ECM), modify the concentration and conformation of cytoskeletal crosslinking proteins, and/or reorder the cytoskeleton by changing the conformation of actin, intermediate filaments or microtubules[47–52]. Since ECs form the inner layer of blood vessels, they interact closely with the flowing blood and are thus highly responsive to flow patterns and shear stress. When exposed to weak hemodynamic forces, nuclei are more rounded and have no preferred direction[53]. The cell body morphology is also rounded, which is characteristic of an increased permeability to plasma constituents, cell turnover rate and intimal penetration[53,54]. Low oscillatory flows are also responsible for this cell behaviour[54]. Conversely, in the presence of undisturbed laminar wall-shear stress, ECs align in the direction of flow and increase their production of anti-inflammatory and atheroprotective molecules such as NO.

Evidence suggests that cells respond to flow in such as way as to minimize the total force exerted by the flowing fluid on their nuclei[53]. Mechanosensing proteins such as integrins, tyrosine

kinase receptor VEGFR-2, G proteins and G protein-coupled receptors, CD21, stretch-activated ion channels, intercellular junction proteins and membrane structures like caveolae, gap junctions, membrane lipids and glycocalyx propagate the force to the nucleus via the cytoskeleton[55]. Integrins transmit and modulate the tensions between focal adhesion sites, membrane receptors, and the ECM to cytoskeletal proteins like actin filaments via the phosphorylation of focal adhesion kinase among others, which then leads to the activation of mitogen-activated protein kinases (MAPKs) using Ras GTPase[55]. Alignment of ECs under shear stress via cytoskeletal reorganization also occurs due to the activation of Rho family GTPases that lead to the formation of stress fibers and focal adhesions. Another mechanism of interest consists of VEGFR-2 activating mechanotransduction especially via the phosphatidylinositol-3-kinase (PI3K) and Akt complex pathway [55]. PI3K/Akt can in turn activate endothelial NO synthase (eNOS) in ECs, NO being a known atheroprotective molecule.

Nuclei also reorient in the direction of shear stress to decrease their apical height. The nuclear lamina is formed by nuclear lamins, which are type V intermediate filament proteins of critical importance for the structure of the nucleus[56]. B-type lamins confer elasticity and A-type lamins give stiffness to the nucleus. Force transmission from the ECM to the nucleus can occur via the linker of nucleoskeleton and cytoskeleton complex binding to the actin filaments as well as A-type lamins[57]. There is inside-out signaling from the nucleus to the cytoskeleton and the ECM via the assembly state of lamin A to balance forces inside and outside[57]. Hence, external stimuli does not only elicit a response of the nucleus in terms of its position in the cell, it also affects subnuclear structures and clearly affects gene expression[58]. Among others, mitogen-activated protein MAPKs are upregulated and the pro-inflammatory transcription factor nuclear factor kappa-light-chain enhancer of activated B cells (NF-κB) is localized to the nucleus[55,58]. Nuclear abnormalities characteristic of HGPS could disrupt these mechanotransduction processes.

To summarize, the activity of AP-1 [59], pathways like Notch/P13K and ERK/Akt as well as VEGF expression have all been shown to respond to shear stress in ECs[21]. The endothelium in regions of the vasculature susceptible to atherosclerosis is exposed to turbulent flow rather than laminar. Curved regions, branch points, and bifurcations are considered atheroprone[55]. The

wall-shear stress at these regions being irregular, ECs do not align in the direction of the flow. In other words, the endothelium in the atheroprone regions, shows activation of pro-proliferative and pro-inflammatory gene expressions, reduced production of NO, increased leukocyte adhesion and permeability, as well as other atheroprone phenotypes[55].

Finally, aging cells have increased mechanosensitivity in the sense that they have an altered reaction to forces and impaired rearrangement ability. For instance, eNOS is up-regulated in young ECs exposed to laminar shear stress but not in old ECs. Consequently, the atheroprotective effects of NO are limited in old ECs, making them more sensitive to apoptosis[60]. This accentuates how critical it is to study ECs under physiological flow. Most reports on human endothelial cell biology in the context of aging remain limited by experimental platforms utilizing static culture conditions. Alternatively, rodent models do not suitably replicate human vascular physiology or flow conditions. There is a significant gap between conventional *in vitro* and *in vivo* models of vascular aging. Studying aged human endothelial cell biology under flow *in vitro* can partially fill this gap.

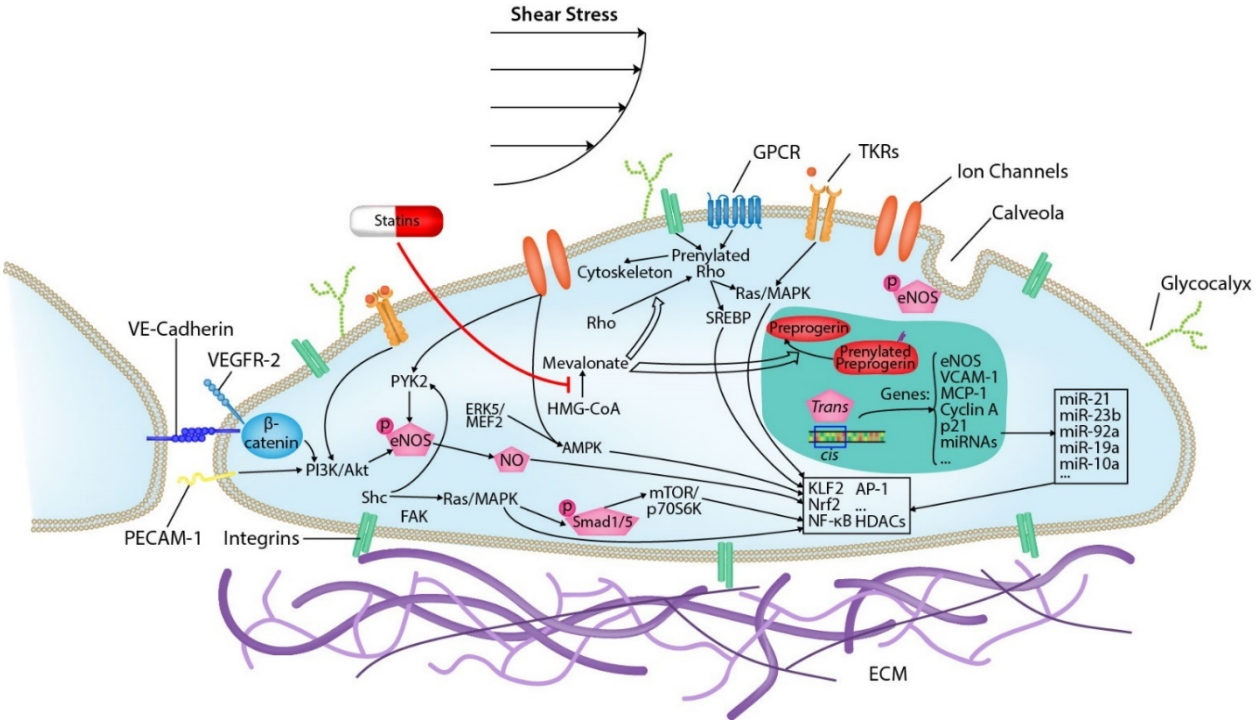

Figure 3: *Mechanotransduction pathways in ECs and their potential interactions with compounds used to treat atherosclerosis. Figure adapted from Zhou et.al*[55]

Models to study Vascular Cells under Shear Stress

Live-cell imaging is a useful technique to study the rearrangement of cells in response to shear stress in real time. Blood vessels *in vivo* do not allow for studying of isolated mechanical forces. Various *in vitro* devices have been engineered to allow for visualization and analysis of cells under shear stress, or tangential stress. For instance, multi-well plates placed on an orbital shaker can be used to study cells under shear stress induced by the swirling of the culture media. Although this method allows for high throughput, it does not lend itself to live-microscopy imaging and exposes the cells to inhomogeneous mechanical stresses[61]. Flow chambers of various geometries can be used to study the effect of shear stress on cells under various controlled flow conditions on cells. Cone-and-plate systems have been used to generate wall shear stresses over a surface ranging from 0 to over 200 dyn/cm^2 [2]. Parallel-plate designs allow for slightly higher throughput experiments than cone-and plate[2]. They are particularly popular systems since they can be designed to generate well-defined, potentially fully laminar uniform shear stress, while having an ideal geometry for live microscopy[61–63]. The relationship between the flow rate and the resulting wall-shear stress in a parallel-plate system can be accurately approximated by the following formula:

$$\tau = \frac{3Q\mu}{2WH^2} \quad \text{(Eq. 1)}$$

Where τ is the wall shear stress, Q is the volumetric flowrate, μ is the kinematic viscosity of the liquid or media, W is the width of the flow chamber and H is the height separating the parallel plates.

In collaboration with the laboratory of Prof. Jean Ruel in the Department of Mechanical Engineering at Université Laval, Prof. Hoesli designed a multi-well flow chamber system, with dour isolated chamber, to image cell-surface interactions and alignment dynamics under flow conditions[2]. The sterile imaging chamber and closed circulation loop can be placed in an incubator at 37ºC and 5% CO_2, or under a live-cell imaging microscope in the same conditions. The perfusion is driven by peristaltic pumps with in-line pulse dampers to reduce flow pulsatility[2]. Textural image analysis was implemented to quantify cell alignment in response to step changes in shear stress using phase-contrast images of ECs under flow[2].

Quantifying cell and nuclear alignment in the direction of flow

Although useful as simplified flow models, most parallel-plate systems are complex to set up and require a high level of technical expertise to avoid leakage and air bubbles[61]. Microfluidic devices are another common approach to investigate the effects of flow on cells. They have relatively high throughput, but more importantly can be rapidly prototyped for a variety of spatial arrangements. However, due to their very small size, boundary effects create inhomogeneous wall-shear stress profiles across microchannels[61]. By design, parallel-plate systems are limited to the study of well-developed laminar shear stress. More complex geometries are required to study shear stresses in typical arteries, especially in the atheroprone regions of the vasculature exposed to turbulent flows. Cylindrical models are an alternative to meet these design conditions. For instance, Prof. Richard Leask, of the Chemical Engineering Department at McGill University, developed a leukocyte-adhesion-to-endothelium assay in 3D culture models perfused by peristaltic pumps[64].

When studying EC responses to flow, the extent of cytoskeletal alignment can be quantified by measuring the angle between individual actin filaments and the horizontal plane defined as the direction of the flow. Image analysis allows the determination of the preferred orientation of structures in an input image using a Fourier component analysis[65]. Nuclei morphology and alignment can also be analyzed by automatically detecting nuclei and assessing the relative level of the signal they emit, when exposed to consistent exposure across samples, via the mean gray value (MGV). The mean gray value is defined by the equation below[66].

$$MGV = \frac{sum\ of\ gray\ values\ for\ all\ selected\ pixels}{number\ of\ pixels} \qquad \text{(Eq. 2)}$$

This number can be interpreted as a measure of signal intensity when the areas of the particles detected are similar. Image analysis tools can fit an ellipse on the detected area and calculate its major and minor axis, in other words, its aspect ratio, as well as provide its orientation. The function also allows for the calculation of circularity and roundness, defined as follows[66].

$$Circularity = \frac{4\pi\,[Area]}{[Perimeter]^2} \qquad \text{(Eq. 3)}$$

$$Roundness = \frac{4\,[Area]}{\pi\,[Major\ Axis]^2} \qquad \text{(Eq. 4)}$$

Circularity is the measure between 0 and 1 of how circular, as opposed to angular the shape detected is. The closer to a perfect circle, the more the value approaches one. One can hypothesize that this value would be affected by the presence of blebbing of the nuclear envelope creating a ragged edge, as seen in aged or HGPS-ECs[67]. Roundness is the inverse of the aspect ratio.

Ultimately, although these flow models have been used repeatedly with ECs, they have rarely been combined with the study of aged ECs. Only one study looked at vascular cells from HGPS-iPSCs under biomechanical strain using microfluidics, but it involved VSMCs not ECs[10]. A gap in research has to be filled by combining these types of platforms with customized models to study aged EC biology specifically.

Models of Vascular Aging and their Limitations

Studying organismal aging in humans is no easy feat since, under normal conditions, it requires the passage of multiple years, even decades. Cardiovascular disease also tends to be discovered in patients with the onset of symptoms, which is too late in the timeline to study the origins of aging. Vascular aging can be studied in animal models with shorter life lifespans, such as aged mice. However, this strategy is cost, labour and time-intensive. Rodents are also not optimal models since they tend to not develop cardiovascular disease and have high telomerase activity when fed a normal diet[68]. The aging of the heart in mice is similar to that of humans, but atherosclerosis phenotypes require genetic modifications[69]. To study the progression of atherosclerotic lesions, lipoprotein metabolism genes were manipulated to provoke hypercholesterolemia[69]. Hence, mice that were genetically modified to be low-density lipoprotein receptor -deficient, apolipoprotein E-deficient, Forkhead box protein O1 -deficient or some combination of the three have were found to develop atheroma lesions[69]. The clinical utility of these model in drug or treatment development is limited since they do not reproduce the contribution of aging and inflammation in the progression of the disease. To circumvent this, senescence-accelerated mouse models considered to be prone display morphological alterations and endothelial dysfunction with diminished eNOS expression[69,70]. Genes associated with ageing like Sirtuin1 have also been manipulated in some mice. Finally, some rodent models have been refined by including accelerated aging pathologies such as laminopathies likes HGPS[68]. While these models have significantly advanced our understanding of aging, they are severely limited by hemodynamic profiles in rodents being

vastly different from larger animals[68]. Furthermore, molecular mechanisms associated with vascular aging are difficult to isolate from other interacting factors *in vivo*.

Fundamental biomolecular studies are performed *in vitro*, where EC cultures allow for an array of assays to be performed under controlled conditions. Senescent ECs are usually obtained from elderly donors or by serial passaging. Biopsies from aged donors are difficult to obtain in large quantities and donor variability complicates reproducibility. Passaging as an accelerated means of *in vitro* aging also leads limitations since factors like trypsinization time can have a significant impact on cell spreading and migration for instance[71]. This method also mainly models replicative senescence, which is not the only physiologically relevant contribution to vascular aging.

Assessment of Biomolecular Markers of Inflammation

On leading strategy when it comes to assessing the development of vascular aging and dysfunction has been the measurement of markers of inflammation[72]. This has proven to be a difficult endeavour clinically, but *in vitro*, the study of biomolecular markers is more straight forward. Inflammation is involved in all stages of atherosclerosis, from the initiation, to the growth of plaques and the rise of complications[72]. The inflammatory cascade might even be compared to an inflammatory response to injury. The presence of proinflammatory cytokines represent early indicators of systemic inflammations. Increased cytokines levels can arise directly from the atheroma and initiate, or at least be directly involved in the inflammatory cascade[73]. For instance, interleukin-6 (IL-6) is thought to cause the upregulation of C-reactive protein in the liver, which is a marker of systematic inflammation[73]. Additionally, IL-6 has shown to increase endothelial barrier permeability, and it is known that the subsequent vascular leakage is a hallmark of inflammatory response[74]. It is also known that other cytokines like TNF-α and IL-1 can stimulate Il-6 expression as well as that of effector molecules like the leukocyte adhesion molecule ICAM-1 known to be involved in the growth of the atherosclerotic plaque[73]. On the other hand, IL-11 has been shown to reduce tissue injury in animal models of vascular inflammation[75]. This cytokine has shown anti-inflammatory, immunomodulatory and cytoprotective effects[75,76]. In HUVECs, its cytoprotective effects have been thought to depend on MAPK and extracellular signal-related kinase kinase-1 inhibitor activation[77]. Exposure to low concentrations of IL-11 protected the ECs against lysis without inhibiting tumour necrosis factor activation of NF-κB, intercellular-adhesion

molecule 1 or E-selectin[75]. The absence of IL-11 could indicate an inability of vascular tissue to protect itself from immune-mediated injury.

Investigating cell death is also an important aspect when studying cellular aging and endothelial dysfunction, especially when exposing aged cells to mechanical stresses. Necrosis and apoptosis are the two main forms of cell death in both normal and diseased tissue. Necrosis is closely associated with inflammation[78]. It can be a programmed event or cytokines in the TNF family can also trigger this kind of death[78]. Permeabilization of the cell membrane is a hallmark of necrosis[78]. When this occurs, the plasma membrane leaks intracellular contents into the extracellular milieu. Cytotoxicity assays are based on two different approaches: (1) the uptake of DNA binding dies like propidium iodide that cannot enter the plasma membrane of normal living cells, and (2) the aforementioned leakage of intracellular contents[78]. Lactate dehydrogenase (LDH) assays are often used to quantify cytotoxicity *in vitro*. (see **Figure S3** for more details)

Hutchinson Gilford Progeria Syndrome and Biological Aging

Phenotype and Biomolecular Overview of HGPS

Hutchinson-Gilford progeria syndrome (HGPS), also called progeria, is a rare and fatal genetic disorder that causes premature aging. At birth, the children affected by HGPS appear normal, but their condition rapidly degrades within their first two years of life[79]. The clinical presentation of this disease includes growth retardation, skeletal muscle atrophy, decreased joint range of motion, failure to thrive, sclerodermatous/hardened skin changes, prominent eyes, alopecia, micrognathia or undersized jaw, decreased subcutaneous fat and pronounced atherosclerosis[14,19,80]. On average, children with progeria die of atherosclerosis and associated cardiovascular complications in their teenage years[14,19].

Laminopathies are a group of diseases caused by a mutation of the lamin A gene (LMNA). HGPS is one of the 11 known laminopathies caused by over 180 known mutations of LMNA, which codes for nuclear lamins A and C[14,19,81]. Nuclear lamins are type V intermediate filament proteins of critical importance for the structure of the nucleus[56]. Lamin A plays a diverse but extremely important structural and regulatory role in nuclear scaffolding, nuclear pore formation, chromatin organization, DNA repair mechanisms, mitosis, gene regulation such as transcription and epigenetics, and cell differentiation[56]. LMNA mRNA is first translated into

prelamin A, which undergoes extensive posttranslational modifications, including farnesylation, methylation and proteolytic cleavages[14,82]. The ultimate stage of modification of prelamin A consists of the proteolytic cleavage of the C terminus of the preprotein to generate the mature unfarnesylated and unmethylated lamin A protein, when the zinc metalloproteinase ZmpSte24 recognizes a 50 amino-acid sequence and cleaves a specific site[82].

With an incidence between 1 in 4-8 million live births worldwide, HGPS is a rare and sporadic disorder[81]. Approximately 90% of HGPS cases consists of a de novo silent heterozygous mutation at G608 in exon 11 on the LMNA gene[81,83,84]. This mutation in the LMNA gene increases the probability of errors during transcription by activating a alternative cryptic splice site in part of the transcript that would not be spliced otherwise. The alternatively spliced form of LMNA results in an internal deletion of 150 amino acids, where the proteolytic cleavage recognition site for ZmpSte24 is located[81,84]. As illustrated in **Figure 4**, the resulting isoform of lamin A, called progerin, thus remains farnesylated. The hydrophobicity of the farnesylated region causes progerin to accumulate on the nuclear side of the nuclear envelope, due to hydrophobic interactions, increased electrostatic interactions and aggregation[67,85]. Additionally, the tail of progerin is more compact and less heterogeneous than that of lamin A. Hence, progerin is dysfunctional due to both its accumulation at the membrane, as well as the faulty interactions between its tail and DNA and other proteins[14,86]. The presence of progerin causes significant changes in the shape of the nucleus hallmarked by lobulation of the nuclear envelope, the nuclear lamina thickening, peripheral heterochromatin loss, and nuclear pores clustering[67]. This aberrant morphology of the nucleus is sometimes referred to as blebbing. Cells of the mesenchymal lineage such as VSMCs, adipocytes and fibroblasts express the highest levels of progerin[14]. Mesenchymal stem cells are pluripotent progenitor cells which divide and differentiate into cells that give rise to skeletal tissue such as cartilage, bone, tendon, ligament, marrow stroma and connective tissue[87]. ECs of HGPS patients were also positive for progerin, although at lower levels than VSMCs[13].

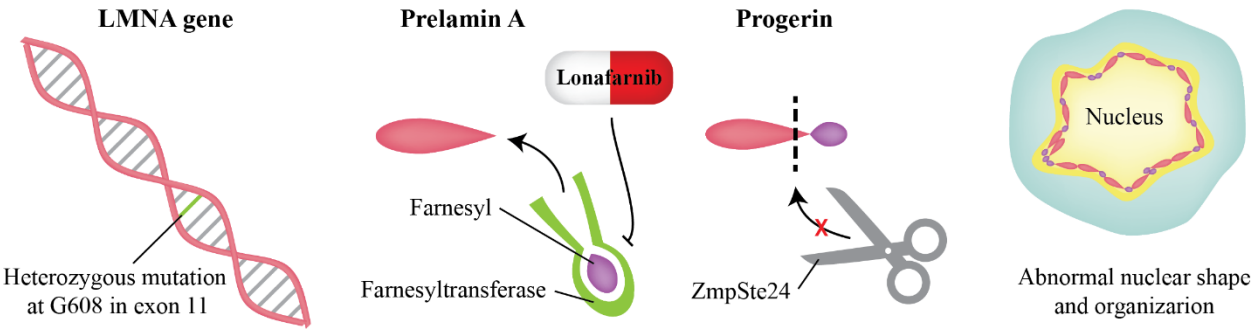

Figure 4: *Schematic of the accumulation of progerin in the nucleus in HGPS due to a mutation in the gene coding for lamin A (LMNA) causing the deletion of the recognition site for ZmpSte24, which leads to the presence of a hydrophobic farnesyl tale on progerin. Farnesyltransferase inhibitors like Lonafarnib (Zokinvy™) are a current treatment for progeria.*

Although the mutation responsible for HGPS is known and diagnosis is highly reliable, there is currently no cure for children suffering from progeria. In 2012, farnesyltransferase inhibitors were shown to prolong lifespan by ameliorating some aspects of cardiovascular and bone disease[88]. Lonafarnib, now Zokinvy™, was granted approval by the FDA in 2020 as the first-ever treatment for progeria and processing-deficient Progeroid Laminopathies[89,90]. Lonafarnib binds to farnesyltransferase, inhibiting it from adding the problematic farnesyl tail to prelamin A. Farnesyl transferase is also involved in the post-translational modification and activation of Ras proteins[91]. More recently, genetic editing to correct point mutations leading to progeria have shown promising outcomes in preclinical models[92,93].

Progerin Contributes to Vascular Disease and Normal Aging

Cellular aging is the precondition to overall aging in an organism[15]. Progerin accumulation caused by a mutation in HGPS causes cellular aging characterized by cell division defects, limited replicative lifespan, and nuclear abnormalities, which has clinical repercussions for the patients who exhibit an aged phenotype. Physiologic similarities between HGPS and normal vascular aging include increased arterial stiffness, calcification and ECM deposition decreased number of VSMCs in the *tunica media*, increased inflammation, higher blood pressure and increased risk of arteriosclerosis, which is the overall thickening and stiffening of arteries[14,94].

The relevance of using HGPS as a model for vascular aging was confirmed when it was discovered that progerin is also expressed in normal aged cells[81]. Cell nuclei of fibroblasts from elderly donors acquired similar defects as those from HGPS patients. Not only was there noticeable nuclear blebbing, but there were changes in histone modifications including the

downregulation of heterochromatin protein 1 and of lamin-A-associated proteins 2, as well as altered histone modification patterns, such as reduced heterochromatin-specific trimethylation of Lys^9 on histone H3 (Tri-Me-K9H3)[95]. Additionally, cultured cells from old donors, as was the case for HGPS donors, had increased unrepaired DNA damage indicated by the presence of foci containing phosphorylated histone H2AX[95]. Although the presence of progerin and thus aberrant lamin A splicing was detected in long-term culture, mRNA levels of progerin in "healthy" old cells were low[81,95]. This suggests that there is sporadic use of the same cryptic splicing site of lamin A that is responsible for HGPS in physiological aging[81,95]. Research in normal human fibroblasts showed that telomere damage due to cellular senescence plays a role in the alternative splicing that leads to progerin production[96]. Directly blocking the cryptic splicing site LMNA reversed nuclear defects[95]. In normal but aged VSMCs, disruption of lamin A processing led to accelerated atherosclerosis. In other words, the accumulation of prelamin A caused calcification and VSMC attrition[97]. Progerin-positive cells have been detected in non-HGPS ages arteries[13], but the extent to which ECs are involved in the progerin accumulation-to-atherosclerosis timeline remains unclear.

HGPS cells show defects in mechanotransduction which are similar to those observed in aged ECs leading to the lack of eNOS upregulation in response to shear stress. Since A-type lamins play a critical role in sensing and balancing forces from the inside-out, disruptions in the nuclear lamina caused by faulty prelamin A processing can impact signal transduction[57]. Nuclei in cells producing progerin are stiffer, but their interior is softer and more compliant[98]. A stiffer nucleoskeleton dampens external shear and compression forces making the softer nuclear inside less responsive to the force propagation[98]. It was hypothesized that the reduced deformability of the HGPS nuclear lamina is due to the presence of oriented and ordered microdomains caused by the more homogenous tail of progerin compared to the disordered lamin in healthy nuclei[99]. The same nuclear stiffening phenomenon was reported in aged cells[100]. Lamin A/C deficient cells display nuclear deformation and defective mechanotransduction as shown by attenuated NF-κB–regulated transcription in response to mechanical and cytokine stimulation[101]. Furthermore, ECM becomes stiffer with age and with the progression of HGPS[100]. This phenomenon, compounded with a stiffer nucleus, was associated with changes in cell migration[100]. As such, it is imperative to investigate the role of progerin and age-associated prelamin A accumulation on EC mechanosensing and related effect on EC dysfunction initiating atherosclerosis in vascular aging.

Induced Pluripotent Stem Cells

Embryonic stem cells (ESCs) are derived from the cells located on the inside of mammalian blastocysts[102,103]. They have the ability to differentiate into cells from all three germ layers: the ectoderm, endoderm and mesoderm, and they can multiply indefinitely while maintaining their pluripotency[102,103]. For these reasons, they are an appealing platform to study development and treat a variety of diseases or disorders. On the other hand, the use of ESCs in research and medicine raises ethical difficulties[103]. Alternatively, somatic cells can be reprogrammed to gain totipotency or pluripotency to form induced pluripotent stem cells (iPSCs) [103]. Reprogramming can occur by transferring nuclear contents of somatic cells into enucleated oocytes, fusing somatic cells with ESCs transducing transcription factors (typically *Oct 4*, *Sox2*, *Klf4* and *c-Myc* using retroviral induction), as summarized in **Figure 5**. This approach provides the opportunity to create personalized iPSC lines from any adult individual in order to study the effect of genetic differences on cellular differentiation and function, as well as develop personalized medicines. In the case of HGPS, most but not all patients have the heterozygous mutation at G608 in exon 11 on the LMNA gene. Variations in the mutation and the rest of the genetic makeup of those individuals could be accounted for by using iPSC technology to help delineate heterogeneous traits of aging depending on this genetic background. By extension, this approach could potentially be used to study interactions between genetic variants or background and cellular aging [103–114].

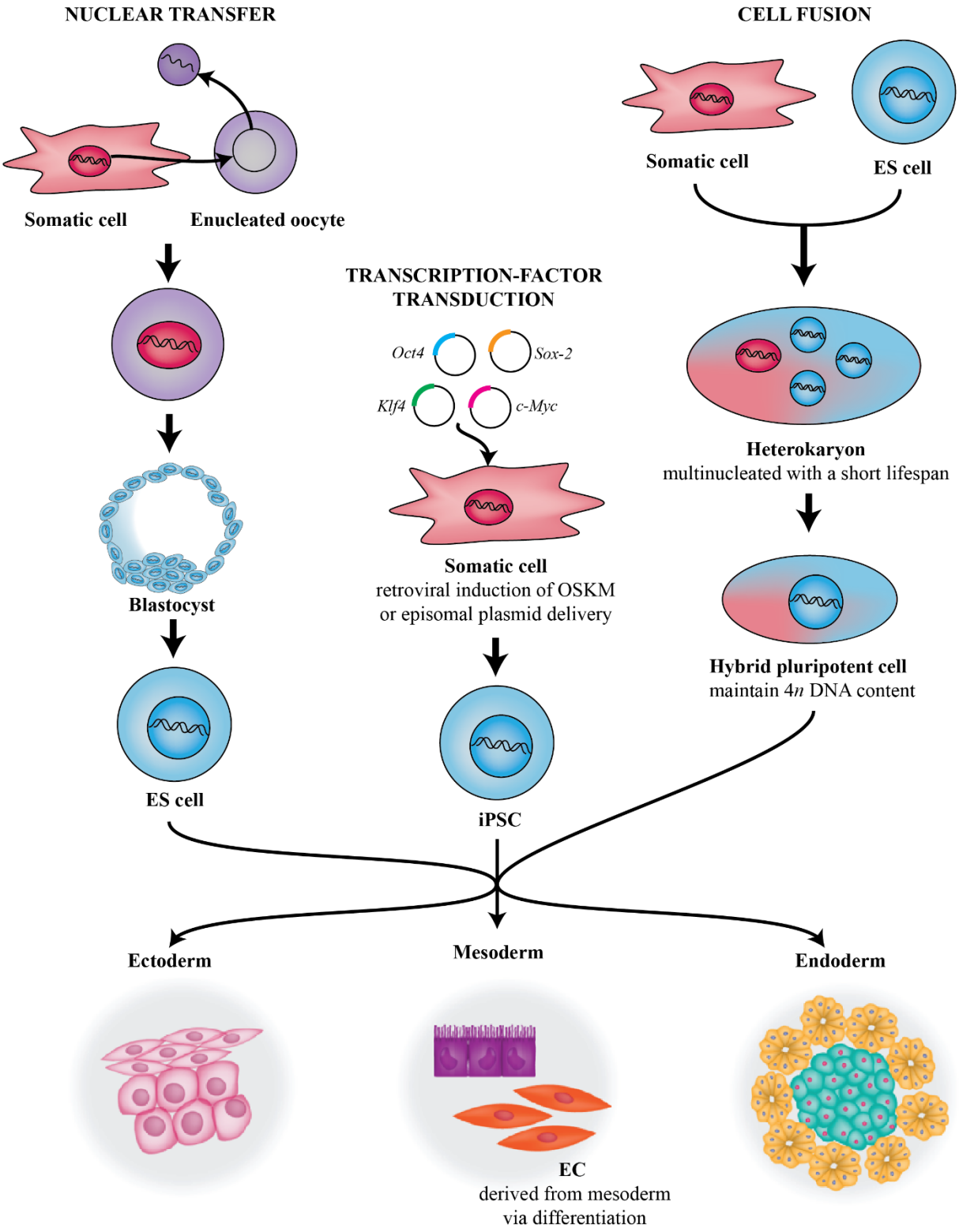

Figure 5: *Schematic of reprograming of somatic cells to pluripotency via nuclear transfer, cell fusion and transcription-factor transduction adapted from Yamanaka and Blau*[104] *and the subsequent ability of pluripotent cells to be differentiated to all three germ layers, being the ectoderm, the mesoderm and the endoderm. ECs are obtained via the mesoderm.*

HGPS-somatic cells have successfully been reprogrammed into HGPS-iPSCs using the four Takahashi and Yamanaka factors[105–107]. It was reported that reprogrammed donor fibroblasts exhibited high levels of genes associated with undifferentiated pluripotent stem cells after retroviral OSKM induction[105]. Furthermore, the HGPS-iPSCs lost cellular defects characteristic of the starting somatic cells, such as the abnormal nuclear morphology, as well as the altered epigenetic modifications and gene expression[105–107]. The reprogramming of HGPS-fibroblasts proved to be less efficient than that of control-fibroblasts[105,107,108]. This is possibly related to the negative correlation between the level of lamin A expression and reprogramming efficiency[105,107,108]. Indeed, lamin A is not found in ESCs but is strongly expressed in the nuclear envelope of somatic cells[108]. Hence, lamin A expression is a marker of differentiation[109]. It was also shown that progenitor cells have a higher reprogramming efficiency than more differentiated cells, hence that stemness facilitates reprogramming, and that cell senescence impairs reprogramming[110]. The conclusion was drawn that higher lamin A expression, which is also associated with aging, negatively influences reprogramming of somatic cells to iPSC status[108]. This also points to the possibility that progerin expression leading to changes in the nuclear scaffold could hinder the cascade of pluripotency gene expression or the chromatin remodelling events involved in reprogramming[14].

Importantly, HGPS-iPSC differentiation was shown to lead to nuclear aberrations similar to primary HGPS-fibroblasts. Two research groups noted that lamin A and progerin were upregulated during differentiation towards VSMCs, resulting in increased DNA damage, expression of senescence-associated markers and miss-localization of the nuclear protein LAP2[14,105,107]. This is consistent with the previously discussed upregulation of A lamins and progerin genes during the differentiation of pluripotent stem cells into fibroblasts, MSCs and VSMCs[105,109]. In the mesodermal lineage, terminally differentiated VSMCs showed higher progerin expression levels than their progenitors[14,105]. Increasing progerin levels may alter differentiating cells fate. For instance, progerin-expressing cells have the abnormal tendency to differentiate spontaneously[111]. It was found that progerin expression in mesenchymal stem cells activated effectors downstream from the Notch signalling pathway, which changed their differentiation potential[14,111,112]. In brief, there is exhaustion and altered differentiation of HGPS stem cells toward the mesodermal and mesenchymal lineages and the resulting VSMCs and fibroblasts, mainly, show an accumulation of progerin with age. Consequently, the

regeneration of potential vascular tissues decreases, even more so when under heavy mechanical stress causing high cell turnover or continuous growth[14]. Although most of the evidence so far shows that vascular aging in the context of HGPS is predominantly an issue of VSMCs, EC aging could also be part of the equation. It is thus important to study EC aging and endothelial dysfunction as it could impact both treatments for HGPS and help understand the physiology of vascular aging in general.

Directed differentiation of iPSCs into Endothelial Cells

Studying the underlying mechanisms of vascular aging and endothelial dysfunction in HGPS has been challenging due to the difficulty in obtaining primary vascular cells from HGPS patients. Most studies have thus relied on studying more easily obtained HGPS-fibroblasts, mouse models of HGPS and cells engineered to overexpress progerin. iPSCs offer a unique platform to study the native expression of progerin and its effect on vascular cells by providing a virtually unlimited source of ECs once differentiated *in vitro*.

ECs can be derived from stem cells using monolayer-culture methods, embryoid body-based protocols and co-culture methods. Embryoid body-based approaches take advantage of attempting to mimic the 3D cell micro-environment in development obtain vascular ECs[113,114]. Systems where iPSCs and a mouse bone marrow stromal cell line OP9 are co-cultured were able to generate hematopoietic progenitors and ECs quite reliably[115]. However, these two approaches face handling and reproducibility limitations compared to monolayer protocols[116–122].

In 2015, under the supervision of Prof. C. Hoesli at McGill University, Jonathan Brassard compared the differentiation of iPSCs into ECs using two protocols. The first approach, which is summarized in **Figure 6**, consisted of a stepwise combination of treatment of human ESCs with glycogen synthase kinase 3β (GSK-3β) inhibitor and culturing with VEGF[118]. More specifically, the 10-day protocol involved the differentiation, isolation of ECs and expansion for up to around 30 days[118].

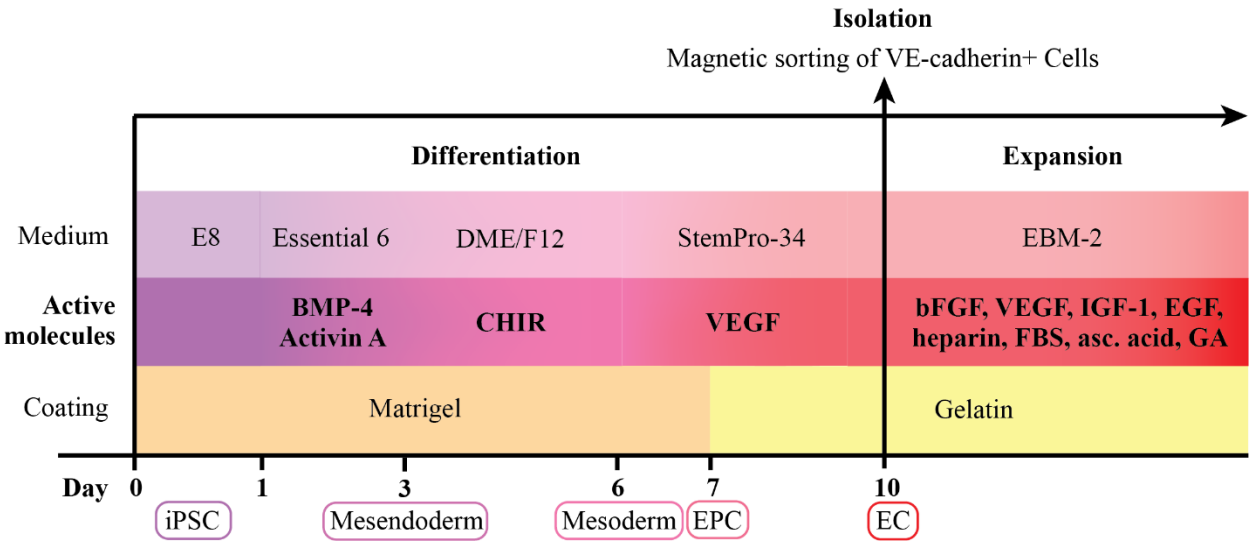

Figure 6: *Schematic of the differentiation protocol used by Tatsumi et. al to obtain ECs from iPSCs. Pluripotent stem cells cultured on Matrigel™ were committed to the mesendoderm by supplementing bone morphogenic protein 4 (BMP-4) and activin A to the growth medium, consisting of basal medium E8 with essential 6, for 3 days. Mesodermal commitment was then induced by 3 days of culture in DMEM-F12 supplemented with CHIR99021, an aminopyrimidine used in cardiomyocyte differentiation that inhibits glycogen synthase kinase-3β. Then, the addition of VEGF-165 in the basal medium StemPRO™ 34 caused further differentiation to the endothelial progenitor cell (EPC) stage after a day and to ECs after 72 hours on gelatin. Following the 10-day protocol, positive magnetic selection of ECs expressing VE-cadherin was performed using a magnetic sorting system, followed by cell expansion on gelatin with the basal medium EBM-2. Basic fibroblast growth factor (bFGF), VEGF-165, insulin-like growth factor 1 (IGF-1), epidermal growth factor (EGF), heparin, Lonza fetal bovine serum (FBS), ascorbic acid and the antibiotics Gentamicin and Amphotericin were supplemented to the culture[118].*

The second protocol investigated by Mr. Brassard was shorter in duration, being 6 days compared to 10 days, and the yields were slightly higher. Sahara *et. al* discovered that more efficient differentiation of human ESCs into ECs could be obtained in two steps: (1) mesoderm specification and (2) vascular commitment[116]. Mesoderm specification was performed with the administration of BMP-4 and CHIR to mTeSR-1 treated stem cells in N2/B24 medium and cultured on Matrigel™ for 3 days. The addition of VEGF-A together with inhibiting the Notch signalling pathway led to the commitment to the endothelial lineage after 3 additional days[116]. As previously discussed, the Notch signalling pathway is a highly conserved pathway responsible for some inductive events in animal development. Notch signalling helps maintain stem-cell fate since it mediates lateral inhibition, a competitive interaction that drives neighboring cells toward different fates[22]. Notch inhibition in this protocol was achieved by the addition of DAPT, as γ-secretase inhibitor[116,123]. The same separation via magnetic microbeads as Tatsumi *et. al* was performed to select for VE-cadherin + cells[116]. However, the

reported yield of the protocol was much higher, with over 50% conversion efficiency, and the subsequent EC expansion was performed on fibronectin rather than on gelatin-coated culture surfaces[116]. **Figure 7** in the Methods section summarizes the adapted Sahara et. al protocol used for this thesis work. Using this type of iPSC to EC differentiation can be a powerful tool in the context of HGPS to gain understanding into the disease progression in ECs and to identify new targets for treatment, while simultaneously shed light on physiological EC aging and, potentially, on ways to intervene.

Assessment of endothelial cell differentiation

A reliable method to identify cell phenotype is to study surface markers. Various membrane-bound molecules can give clues as to how far along the differentiation stages a cell is. For instance, **TRA-1-60** is a human pluripotent stem cell marker lost during EC cell differentiation[124]. **CD34** is a transmembrane glycoprotein that serves as a hematopoietic progenitor cell antigen involved in cell-cell adhesion. It is normally found on hematopoietic cells in the umbilical cord and the bone marrow, in certain mesenchymal stem cells, EPCs, blood vessel ECs, mast cells and some dendritic cells[125,126]. **CD105**, also called endoglin, is a component od the transforming growth factor-β receptor complex expressed on a subset of CD34+ progenitor cells from the bone marrow, peripheral blood or cord blood[127]. It is a positive marker of EC differentiation. **CD140 a and b** are platelet-derived growth factor receptor α and β respectively. CD140a is expressed on fibroblasts, VSMCs, glial cells and chondrocytes[128]. The substrate, platelet-derived growth factor is a mitogen (a chemical substance that triggers mitosis) in connective tissue and glial cells. It also acts as a chemoattractant for fibroblasts, VSMCs glial cells, monocytes and neutrophils. The β subunit is responsible for chemotaxis[128,129]. Platelet-derived growth factor receptor is a positive marker for ECs. **CD31**, also known as platelet endothelial cell adhesion molecule 1 is a transmembrane glycoprotein present on the surface of monocytes, granulocytes platelets and ECs. Anti- platelet endothelial cell adhesion molecule 1 has been used histochemically to identify ECs and angiogenic blood vessels[130]. Somewhat similarly, **CD146**, initially called melanoma cell adhesion molecule, is also a transmembrane glycoprotein, although it also has a soluble form, expressed in blood cells forming blood vessels, especially ECs[131]. It plays an important role in signalling since it acts directly on motility and due to its involvement in angiogenesis and inflammation via vessel permeability and leukocyte transmigration[131]. Next, VEGF receptor 2 (VEGFR-2) is also known as kinase insert domain receptor (KDR) and designated **CD309**[132]. During development, is

expressed in mesodermal blood island progenitors, EPCs, and ECs. However, during adulthood, VEGFR-2 regulates vascular EC function and varying levels of expression were also detected on neuronal cells, megakaryocytes and hematopoietic stem cells[132]. **CD144** also called vascular endothelial (VE)-cadherin, which is a strictly endothelial adhesion molecule of the cadherin family locates at the junction between ECs. It plays an important role in controlling vascular permeability and leukocyte infiltration of the tunica intima, as well as a vital role in regulating cell proliferation and apoptosis due to its involvement with VEGFR functions[133].

An important endothelial cell intracellular marker is **Von Willebrand factor** (vWF) - an adhesive and multimeric glycoprotein found in ECs and megakaryocytes to perform haemostasis functions. It does so by mediating platelet adhesion to damaged vascular subendothelium in regions of high wall-shear stress and subsequently platelet aggregation[134]. Following a vascular injury, vWF has been shown to bind to type I and III collagen fibers[134]. Before being released, vWF is either secreted directly into the blood plasma by the ECs that synthesized it, or it is stored in rod-shaped organelles known as Weibel-Palade bodies in the cytoplasm[134]. The presence of vWF in the cell body visualized by immunostaining is indicative of endothelial phenotype.

3. GOALS AND HYPOTHESIS

The overall goal of this thesis was to develop methods to investigate the response to shear stress of ECs in the context of vascular aging. The central hypothesis was that ECs derived from iPSCs of HGPS patients could model aged cells exposed to shear stress in a flow chamber system. To test these hypothesis, specific aims were to:

(1) Assess the differentiation of HGPS-iPSCs into ECs using an adapted version of the Sahara *et al.* protocol and investigate the accumulation of progerin in HGPS-iPSC-ECs compared to fibroblasts from HGPS patients, which are positive controls for progerin
(2) Establish assays to assess the effect of laminar shear stress on aged EC alignment and inflammatory responses.

4. MATERIALS AND METHODS

CELL CULTURE

Induced Pluripotent Stem Cells (iPSCs)

The iPSCs used were donated directly by the Stanford lab at OHRI (University of Ottawa) with authorization from the Progeria Research Foundation (McGill IRB A04-M23-20A and material transfer agreement from Progeria Research Foundation). The lines generated by the Stanford lab were obtained by OSKM viral vectir reprogramming of fibroblasts donated by 3 patients and 3 unaffected controls. The cell lines used are detailed in **Table 1**. iPSCs were maintained in CELL+ culture treated 6-well plates (#83.3920.300, Sarstedt, Germany) coated with Matrigel® Matrix (#354277, Corning, Discovery Labware Inc., Bedford MA, USA) diluted in DME/F-12 (1:1) (with w.50 mM L-Glutamine and 15 mM HEPES Buffer) (#SH30023.01, HyClone Laboratories, Logan UT, USA) with TeSR™-E8™ Basal media (#05940, Stemcell™ Technologies, Vancouver BC, Canada) supplemented with 500X and 20X components provided in the kit. This later changed for the newer version of the same medium (#05990) with only one 25X supplement. The cells were frozen in mTeSR™1 Basal Medium (#85851, StemCell™ Technologies) with 5X supplements provided in the kit.

Table 1: *List of iPSCs used from the Progeria Research Foundation*[135]

Cell Line Number	Relation to Proband	Mutational Analysis	Passage
HGADFN003 iPS1C	Proband	LMNA Exon 11, heterozygous c.1824C>T (p.Gly608Gly)	x+15 to18
HGADFN003 iPS1D	Proband	LMNA Exon 11, heterozygous c.1824C>T (p.Gly608Gly)	x+22 to 26
HGADFN167 iPS1Q	Proband	LMNA Exon 11, heterozygous c.1824C>T (p.Gly608Gly)	31 to 32
HGADFN167 iPS1J	Proband	LMNA Exon 11, heterozygous c.1824C>T (p.Gly608Gly)	19 to 21
HGMDFN090 iPS1B	Mother of 167	LMNA Exon 11, Negative	33+6 to 8
HGFDFN168 iPS1D2	Father of 167	LMNA Exon 11, Negative	31 to 34
HGFDFN168 iPS1P	Father of 167	LMNA Exon 11, Negative	32 to 42

Directed differentiation of iPSCs into ECs

The differentiation protocol used was adapted from Sahara *et al*. and is summarized in **Figure 7**.[116] T75 cell culture treated flasks (#833911002, Sarstedt, Germany) were coated with Matrigel® Matrix (#354277, Corning, Discovery Labware Inc., Bedford MA, USA) diluted in DME/F-12 (1:1) (#SH30023.01, HyClone Laboratories, Logan UT, USA), as previously described. iPSCs cultured in 6-well plates were washed with phosphate-buffered saline (PBS) (without Ca^{2+} and Mg^{2+},#21600-051, Life Technologies). mTeSR™1 Basal Medium (#85851, StemCell™ Technologies) with 5X supplements and 10 µM γ-27632 dihydrochloride (Rock inhibitor) (#ab120129, Abcam, Cambridge, United Kingdom) was added for 3 hours. Following this incubation, the cell clusters were dissociated with 1mL TrypLE™ (#12604013, Life Technologies Corporation, Grand Island, NY USA) for 5 minutes. The cells were counted using hemocytometer and resuspended in mTeSR™ with Rock inhibitor to obtain a concentration of 10,000 cells/cm^2once seeded in the T75 flasks. After 24h, the medium was replaced with DME/F-12 (1:1) (with w.50 mM L-Glutamine and 15 mM HEPES Buffer) (#SH30023.01, HyClone Laboratories, Logan UT, USA) supplemented with N-2 and B-27® Supplements (#17502-148 and #17504-044 respectively, Life Technologies Corporation), as well as 6.7 µM CHIR 99021 (#4423, Tocris Bioscience, Bristol, United Kingdom) and 20 ng/mL rhBMP-4 (#314-BP, R&D Systems®, Minneapolis MN, USA). 72h later, the medium was once again changed, this time for StemPRO®-34 SFM (#10639011, Life Technologies Corporation) supplemented with 50 ng/mL rhVEGF (#293-VE, R&D Systems®) and 10 µM Dapt (#D5942, Sigma Aldrich, Saint-Louis MO, USA). On the sixth day of differentiation VE-cadherin-positive cells were selected using the EasySep™ magnetic sorting technology

(#18000, StemCell™ Technologies) jointly with the Human PE Selection Kit (#18551, StemCell™ Technologies) and PE-conjugated CD144 antibodies (#130-102-737, MACS/Miltenyi Biotec, Bergisch Gladbach, Germany), according to the manufacturer's instructions. Cell culture treated T-75 flasks (#833911002, Sarstedt, Germany) were coated with 0.2% gelatin (type A from porcine skin, #G1890-100G, Sigma Aldrich, Saint-Louis Missouri, USA) for 20 minutes at room temperature. VE-cadherin-positive cells were seeded in these flasks and expanded in Endothelial Cell Basal Medium-2 (EBM™-2)(#CC-3156, Lonza, Walkersville, MD USA) supplemented VEGF and bFGF for the next week until used in further experiments.

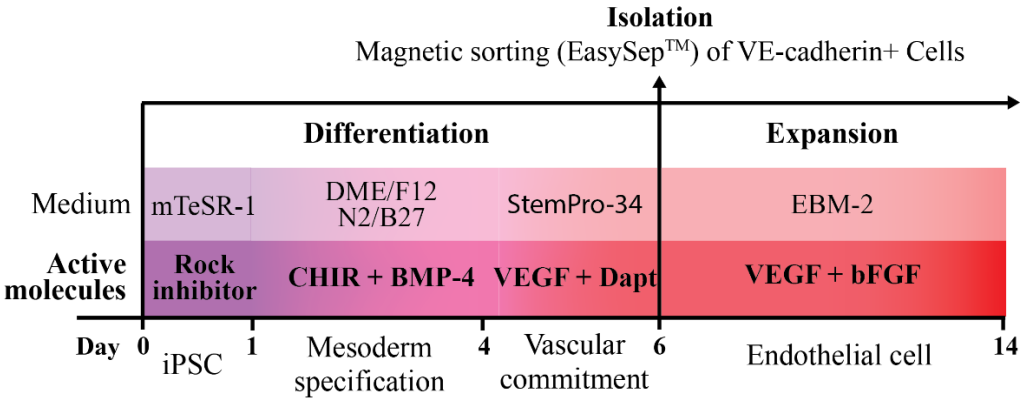

Figure 7: *Schematic of differentiation protocol adapted from Sahara et al. (2014).*

Culture of human umbilical vein endothelial cells (HUVECs)

HUVECs (#CRL-1730, ATCC) at passage 8 were thawed from the liquid nitrogen storage and seeded in cell culture treated T-75 flasks (#833911002, Sarstedt, Germany) previously coated with 0.2% gelatin (type A from porcine skin, #G1890-100G, Sigma Aldrich, Saint-Louis Missouri, USA) for 20 minutes at room temperature. The cells were counted manually using a hemocytometer in order to be seeded at 6,500 cells/cm^2 in EBM™-2(#CC-3156, Lonza, Walkersville, MD USA) supplemented with EGM™-2 SingleQuots® (#CC-4176, Lonza, Walkersville, MD USA), 10% exosome-depleted FBS (#A27208, Life Technologies Corporation, Grand Island, NY USA) and Pen/Strep (50 Units/mL Penicillin, 50 µg/mL Streptomycin) (#15140-122, Life Technologies Corporation, Grand Island, NY USA).

Culture of human saphenous vein endothelial cells (HSVECs)

In order to complete the work required to publish research on the "Dynamics of endothelial responses to laminar shear stress on surfaces functionalized with fibronectin-derived peptides",

HSVECs were transferred from cryostorage at Laval University to McGill. The cells were obtained with the informed consent of healthy donors at the CHU de Québec, Saint- François d'Assise Hospital and isolated via a protocol described in the article[2] (Comité d'éthique de la recherche du CHUQ-HSFA – researchers Laroche & Douville). The HSVECs were thawed and cultured using the same method as the HUVECs detailed above.

Culture of human fibroblasts from Progeria donors and parents

Four fibroblast cell lines were generously provided by the Progeria Research Foundation (with material transfer agreement mentioned earlier) The lines HGADFN003 and HGADFS167 came from patients clinically affected by HGPS, while HGDFDN168 and HGMDFN090 came from the non-affected father and mother of the donor of HGADFN167 respectively. The cells were maintained in cell culture treated T-75 flasks (#833911002, Sarstedt, Germany) and in DMEM supplemented with 2mM of L-Glutamine (), Pen/Strep (50 Units/mL Penicillin, 50 µg/mL Streptomycin) (#15140-122, Life Technologies Corporation, Grand Island, NY USA) and 15% exosome-depleted FBS (#A27208, Life Technologies Corporation). All experiments were performed with fibroblasts between passages 8 and 11.

Culture of a neutrophil-like cell – NB4 cells

NB4 cells were a generous gift from Prof. Richard Leask from the Department of Chemical Engineering at McGill University. They were thawed and cultured at a density of 500,000 cells/mL in RPMI medium with ATCC modifications (#A10491-01, Life Technologies, Grand Island, NY USA) supplemented with 10% FBS (#SH 30396, Hyclone Laboratories, Logan, UT USA), 50 Units/mL penicillin and 50 µg/mL Streptomycin (#15140-122, Life Technologies Corporation, Grand Island, NY USA). 72h prior to perfusion, 10µM of all-trans retinoic acid (ATRA) (#R2625, Sigma Aldrich, Saint-Louis Missouri, USA) was added to the cell suspension.

FLOW CHAMBER

Preparation of test surfaces

Glass or silane-coated (Aminoalkysilane, Electron Microscopy Sciences, Hatfield, PA, Cedarlane 63411-01) slides were cut to 30 mm length using a glass cutter on a smooth clean hard surface. Cut slides were labeled in the upper right-hand corner (typically "I", "II", "IV" and "X") using the engrave pen as to identify the direction of flow during subsequent staining

and microscopy experiments.. Glass slides were coated on one side with 0.2% gelatin (Porcine Skin # G1890, Sigma Aldrich, in UltraPure Water, dissolved at 56ºC and sterile filtered) for 20 minutes at room temperature. Functionalized silane-coated slides were used for the inflammation investigation part of this thesis. CWQPPRARI (referred to as CWQ) and RGD-TAMRA peptides were used to functionalize surfaces, either on their own, mixed or micropatterned using a method previously described[2,136]. All slides were sterilized in the dark for 20 minutes in 100% ethanol. Sterile slides were stored in the dark up to a month in sterile PBS until use.

Flow chamber design and assembly

A multi-well flow chamber system was designed by Hoesli et. al. [2] to provide fully developed laminar flow over a 1.13 cm^2 imaging surface area in each chamber with a uniform wall shear stress ranging from 0.2 to 40 dyn/cm^2.

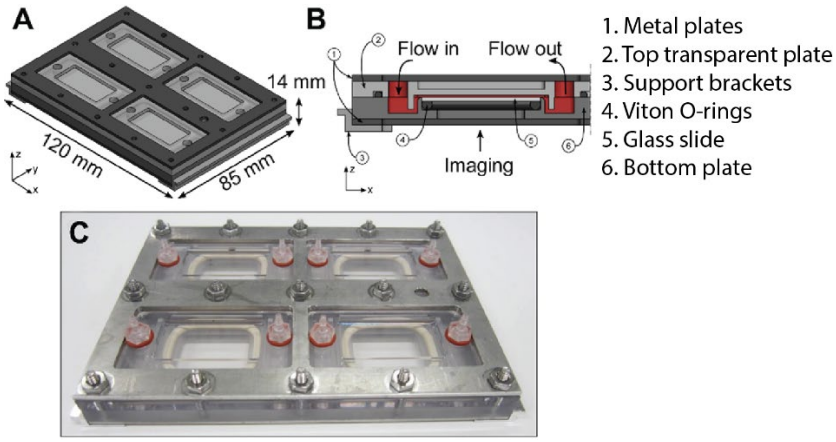

Figure 8: *Flow chamber schematics and picture from Hoesli et al.[2]. (A) shows the overall schematic and outside dimension of the chamber to be mounted on the microscope stage, (B) shows a cross-sectional view of one of the chambers with the path of the liquid and key components indicated, (C) is a photograph once assembled*

Prior to assembly, the two polycarbonate plates, metal plates, support brackets, 9 screws and 9 bolts were sterilized in 100% ethanol for 20 minutes and left to dry in the BSC. The remaining pieces, including the 8 small plastic connectors (#006 9396K11 McMaster-Carr, Elmhurst, IL) with red o-rings, 4 small Viton o-rings (#120 5577K312, McMaster-Carr, Elmhurst, IL) and 4 larger Viton o-rings (#032 5577K12, McMaster-Carr, Elmhurst, IL) were autoclaved along with the tweezers required for assembly using the Prevac 30 cycle.

The flow chamber was assembled aseptically, in the BSC, a day prior to use for live-cell imaging to avoid leaks and slide breakage once mounted on the microscope stage. The connectors linking each chamber to the outside were blocked until their connection to the rest of the flow path using clear C-Flex tubing folded shut with tie-wraps and autoclaved.

Flow path assembly

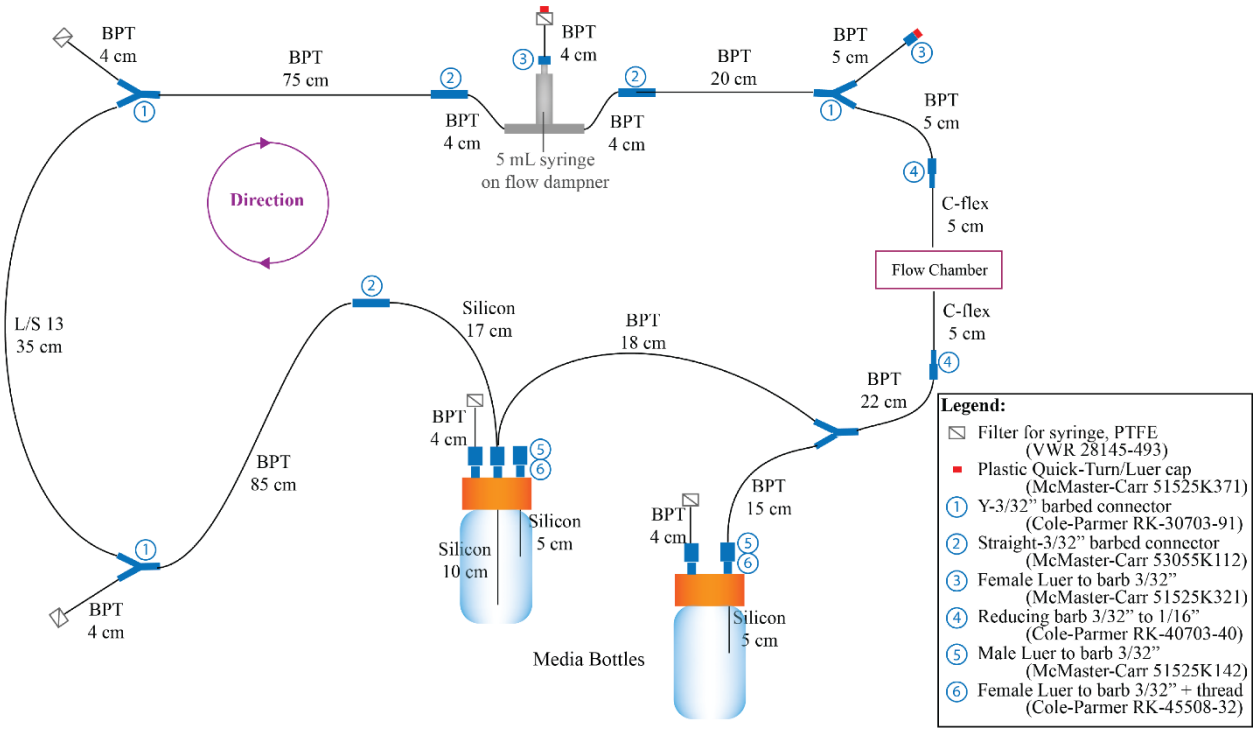

Figure 9: *Diagram of the flow path with tubing type and length written in black, as well as blue connectors, numbered in reference to the legend containing their product ID. The pump heads connect to the L/S 25 and/or L/S 13 tubing segments, with flow going in the clockwise direction on the diagram, the liquid is pushed into the flow dampener consisting of 5 mL syringes mounted on a plastic bubble trap, toward the flow chamber system. The orange rectangles represent the caps of glass bottles used as media reservoir and waste collectors.*

BPT Extension, L/S 13, L/S 25 and platinum-cured silicon tubing (product information detailed in **Table 2**) were cut into blunt-ended segments of the length illustrated in **Figure 9** to generate four separate flow paths. They were linked to connectors as depicted to the diagram and each connection was solidified using tie-wraps, except for the c-flex segments connected

to connector number 4. The c-flex ends were not immediately connected to the flow chamber and thus gently wrapped in aluminum foil for sterilization.

Flow direction was indicated on the segments using arrows marked directly on the tubing or on pieces of tape color coding each flow path to facilitate installation in the incubation chamber. L/S 25 and L/S 13 segments were meant to receive the peristaltic movement of the pumps, pushing liquid toward a flow dampener consisting of four 5-mL Luer-lok™ syringes (one for each flow path), with the piston removed. From each piston, the black seal was removed to gently pierce a hole using a tie-wrap cutter, before being re-installed on a four-channel bubble trap. The end of the syringes was blocked with a short BPT extension tubing segment connected to a PTFE 0.22 µm syringe filter, closed off with a plastic Luer-lok™ cap to allow for aseptic depressurization of the flow dampener once the flow began. Liquid would exit the flow dampener toward the flow chamber, upstream of which a seeding port can be found.

Table 2: *List of components required to assemble the flow chamber*

Name	Company	Cat. No
Masterflex PharMed BPT Tubing L/S 13 25’	Cole Parmer	RK-06508-13
Masterflex PharMed BPT Tubing L/S 25 25’	Cole Parmer	RK-06508-25
Platinum-cured silicon tubing 1/16” ID 1/8” OD 25’	Cole Parmer	RK-95802-02
Clear C-flex Tubing 1/16” ID 1/8” OD 25’	Cole Parmer	RK-06422-02
Masterflex PharMed BPT Extension Tubing 2.29mm ID 100’	Cole Parmer	RK-95809-44
Tie-wraps 1.1 pound solid PP autoclavable cable/zip ties 4” L	Cole Parmer	RK-06830-85
Spectra/Por RC Dialysis Tubing Closures Orange 55mm	Cole Parmer	RK-02899-86
Spectra/Por RC Dialysis Tubing Closures Orange 35mm	Cole Parmer	RK-02900-50
4-Channel Bubble Trap	BioSurface Technologies Corp.	FC 34
Red O-rings (#008) (for bottles)	McMaster-Carr	9396K13
Rainbow tape	Fisher	159015R
100ml PYREX bottles (caps drilled in house)	Fisher	06-414-1A
5mL syringes Luer-Lok™	Fisher	B309646

Live-cell imaging of ECs

EGM™-2 complete medium (#CC-4176, Lonza, Walkersville, MD USA) with Pen/Strep (50 Units/mL Penicillin, 50 µg/mL Streptomycin) (#15140-122, Life Technologies Corporation, Grand Island, NY USA) and 10% exosome-depleted FBS (#A27208, Life Technologies Corporation, Grand Island, NY USA) or serum-free with 0.4% bovine serum albumin (BSA)(heat shock fraction, #A9647-50G, Sigma-Aldrich, Saint-Louis Missouri, USA) was aliquoted in T75 vented-cap flasks (#83.3911.502, Sarstedt, Germany) and placed in an incubator at 37ºC and 5%

CO_2 to adjust for a few hours. The incubation chamber surrounding an IX81 microscope (Olympus Corporation, Shinjuku City, Tokyo, Japan) equipped with a programmable Prior® stage (Prior Scientific Inc., Rockland, MA) was prepared by setting a heater to 37ºC. The temperature on the stage was double-checked using a separate thermometer in water in a 15 mL tube located inside the heated chamber. Air and CO_2 gas cylinders were connected to flowmeters which then merge into a single to a tube entering the imaging chamber. This tube was connected to a filter and then a parafilm sealed Erlenmeyer flask filled with RO water. The gas line then extended into a closable plastic bag in which the media reservoirs were stocked. Gas cylinders were opened at 15 psi and flow meters were adjusted to obtain 5% CO_2. This concentration was confirmed using a CO_2 sensor (series CozIR®, GC-0017, model GSS-20%) connected via USB to a laptop running GasLab® software (v2.0.8.14) (GasLab.com, Ormond Beach FL, USA). The parallel-plate flow chamber apparatus connected the appropriate tubing was tapped onto the stage of the microscope and the same for the flow dampener and some of the tubing or lines to ensure they would not hinder with imaging.

With the incubation chamber ready, the media reservoirs of all four lines were filled with 40 mL of medium previously stored in the incubator. The tubes leading to the waste reservoirs were blocked with dialysis clamps. The flow paths were primed by starting the pumps at low flowrates, making sure no bubbles were trapped in the lines and, mainly, no leaks. At this point, Metamorph® Software (v. 7.10.4)was used to set four stage positions in each imaging chamber and begin timelapse acquisitions. Finally, the ECs of interest were harvested using TrypLE™ (#12604013, Life Technologies Corporation, Grand Island, NY USA) for 5 minutes. They were counted using a hemocytometer before being centrifuged and resuspended to obtain 600,000 cells/mL. Approximately 3 mL of the cell suspension were taken in four 5 mL luer-lok™ syringes (#B309646, BD via Thermo Fisher Scientific, Waltham MA, USA) to seed each imaging chamber individually. At this stage, L/S 13 tubing was connected to the pumps, which were off, the flow path toward the flow dampener was blocked using dialysis clips and the clips blocking the way to waste reservoirs were switched onto the media reservoir lines. Carefully, the cells were introduced into the system through the seeding port equipped with a female Luer-Lok™. The presence of the cells was validated on the microscope and they were left to adhere to the glass surfaces for 3 hours.

After letting the cells adhere, the cells that remained in suspension were flushed from the system by starting the pumps at a very low flow rate (after removing the dialysis clamp from the flow dampener). With a few milliliters removed, the clamps on the media reservoir lines were switched back to the waste lines and the pumps were set to generate 0.5 dyn/cm^2 wall-shear stress overnight with microscope acquisitions every 10 minutes. The next day, the L/S 13 tubing was replaced by L/S 25 tubing in the pump heads, and high wall-shear stress at 22 dyn/cm^2 was started for 6 hours. Microscope acquisitions were increased in frequency to every 3-5 minutes. During this stage, due to the elevated flowrate, almost permanent surveillance of the set-up was required to monitor for visible leaks, decreased media levels in the reservoirs, excessive bubbling, excessive liquid height in the flow dampener syringes and imaging chamber movement causing a loss in focus due to the movement of the tubing connected to the pumps.

Leukocyte adhesion study

To study their adhesion under flow in live-cell imaging, the NB4 cells were stained with 5 x 10^{-7} M Calcein AM dye (Invitrogen) for 30 minutes, protected from light at 37ºC and 5% CO_2. The Cells were then washed twice and resuspended in EGM-2 medium at a concentration of 2.5 x 10^6 cells/mL.

Following 6h of exposure at high wall-shear stress (22 dyn/cm^2), the pumps were paused. 10 mL of medium were collected from the four media bottles using a syringe with luer-lok™. The collected samples were centrifuged for 7 min at 600xg. The supernatants were then aliquoted and stored at -20ºC for further analysis. The NB4 cell suspension was added to each circulation loop with 10 mL of new media to obtain a circulating cell concentration of 500,000 cells/mL. The pumps were restarted to study the adhesion at 2 dyn/cm^2. Phase contrast images at 10X magnification and 5ms exposure were captured every minute at four pre-programmed positions per imaging chamber. After an hour, the perfusion was stopped for good. The flow chamber was carefully removed from the microscope and disconnected from the pumps by cutting the c-flex tubing. The glass surfaces covered with endothelial and NB4 cells were pulled out of the chamber with tweezers and fixed in 4% paraformaldehyde (#J61899, Alfa Aesar, Ward Hill MA, USA) for 10 min[2].

IL-6 and IL-11 quantification via ELISA

IL-6 and IL-11 levels from flow chamber experiments were quantified by enzyme-linked immunosorbent assays (ELISAs) using commercial kits from Abcam (Cambridge, United Kingdom). As previously described, medium samples were collected from the circulation loop right after exposure to high shear stress, prior to the injection of NB4 cells. The supernatants were kept at -20°C until the day of analysis, when they were thawed and centrifuged at 1000xg for 10 min.

For IL-6 quantification, first the Human IL-6 SimpleStep™ ELISA kit (#ab178013, Cambridge, United Kingdom) was used according to the manufacturer's guidelines. The measurements were taken on a Benchmark plate reader (Bio-Rad, Berkeley, USA). belonging to Prof. Leask from the McGill University Chemical Engineering Department. The IL-6 levels in the samples were found to be under the detection levels of this kit. Thus, the IL-6 High Sensitivity Human ELISA kit (#ab46042, Abcam, Cambridge, United Kingdom) was used on the same samples, with the same plate layout, following the manufacturer's instructions. For IL-11 quantification, the IL-11 Human Elisa kit from Abcam was used (#ab100551) according to the manufacturer's specifications.

LDH cytotoxicity assay

Media samples were tested a first time using a Pierce LDH cytotoxicity assay (#88953, ThermoFisher Scientific, Rockford IL, USA) according to the manufacturer's instructions in clear 96 well-plates (#83.3924.300, Sarstedt Inc., Newton NC, USA). The results were found to be under the detection level of the test. Thus, 2 mL of the media samples were transferred to 15 mL conical tubes and frozen, slanted, at -80°C, to lyophilize them. The samples were reconstituted in UltraPure water (#10977015, ThermoFisher Scientific, Rockford IL, USA) to concentrate them 10-fold. The Pierce LDH cytotoxicity assay was then repeated on those concentrated samples. The measurements were taken on a Benchmark plate reader (Bio-Rad, Berkeley, USA). belonging to Prof. Leask from the McGill University Chemical Engineering Department.

FLOW CYTOMETRY

Adherent cells, harvested using TrypLE™ (#12604013, Life Technologies, Grand Island, NY USA), and suspension cells were suspended at a concentration around 500,000 cells/mL in FACS buffer consisting of 0.22 µm sterile-filtered PBS (without Ca^{2+} and Mg^{2+},#21600-051, Life Technologies) with 0.5% BSA (heat shock fraction, #A9647-50G, Sigma-Aldrich, Saint-Louis Missouri, USA) and 2 mM ethylenediaminetetraacetic acid (EDTA) (#15575020, Life Technologies) and kept on ice for the duration of the experiment. Cells were incubated with 2 µL Fc blocking solution (#564220, BD Biosciences, San Jose CA, USA) for 10 min. Surface markers were then studied using the conjugated antibodies listed in **Table 3** and live cells were labelled with 1µL BD Fixable Viability Stain 660 (#564405, BD Biosciences) for 20-30 minutes. Cells were washed twice and resuspended in FACS buffer for analysis. Single compensation controls were created by incubabing UltraComp eBeadsTM (#01-2222, ThermoFisher Scientific, Rockford IL, USA) with PE or FITC-conjugated antibodies for 20-30 min., washing once and resuspending in FACS buffer.

Flow cytometry was performed using a FACSCalibur™ (Becton Dickinson, Franklin Lakes NJ, USA) equipped with CellQuest™ Software v3.3 and a BD Accuri C6 (Becton Dickinson). All acquired flow cytometry data was further analyzed with FlowJo software v.10 (FlowJo, LLC, Ashland OR, USA).

Table 3: *Flow cytometry antibody list*

Name	Conjugate	Clone	Company	Cat. No
CD144 (VE-Cadherin) (Mouse anti-Human)	FITC	55-7H1	BD Biosciences	560411
CD105 (Mouse anti-Human)	FITC	266	BD Biosciences	561443
CD34 (Mouse anti-Human)	FITC	581	BD Biosciences	555821
CD31 (Mouse anti-Human)	PE	WM-59	BD Biosciences	555446
CD309 (VEGFR-2) (Mouse anti-Human)	PE	89106	BD Biosciences	560494
CD146 (Mouse anti-Human)	PE	P1H12	BD Biosciences	550315
TRA-1-60 (Mouse anti-Human)	FITC	TRA-1-60	BD Biosciences	560380
CD49b (Mouse anti-Human)	FITC	AK-7	BD Biosciences	555498

IMMUNOSTAINING

Static culture samples were generated by cultivating ECs and fibroblasts on glass slides (sterilized in 100% ethanol for 20 min.) equipped with an autoclaved flexiPERM® (#94.6077.434

and #94.6077.435 Sarstedt Inc., Newton NC, USA). Dynamic samples consisted of glass slides removed from the flow chamber set up. All samples were washed with PBS (Ca^{2+} and Mg^{2+}depleted, #21600-051, Life Technologies, Grand Island, NY USA) and fixed for 10 min. with 4 % paraformaldehyde (#J61899, Alfa Aesar, Ward Hill MA, USA). After being permeabilized with Triton-X 0.1% (#T878-250ml, Sigma Aldrich, Saint-Louis Missouri, US) for 15 min., the samples were washed twice with 0.05% TWEEN® in PBS (TWEEN®20 # P1379, Sigma Aldrich). Non-specific binding sites were blocked by incubating in Dako Serum-Free Protein Block (#X090930-2, Cedarlane, Burlington ON, Canada) for 15 min. Primary antibodies consisting of mouse anti-progerin clone 13A4 (1:500) (#05-1231, Millipore Sigma, Darmstadt, Germany), rabbit anti-Lamin A (1:500) (#ab26300, Abcam, Cambridge United Kingdom), rabbit anti-von Willebrand Factor (1:200) (#F3520-100UL, Sigma Aldrich) and rabbit anti-PARP1 (cleaved form) (1:500) (#ABC26, Millipore Sigma) were diluted in Dako Antibody Diluent (#S302283, Cedarlane) and incubated overnight at 4ºC. The next day, following two washing cycles with 0.05% TWEEN®, the samples were incubated in the dark for 1 hour at room temperature with the secondary antibody cocktail made of FITC phalloidin (1:200) (#P5282-.1MG, Sigma Aldrich), AlexaFluor™ 647 phalloidin (1:40) (#A-22287, ThermoFisher Scientific) or , Alexa Fluor® 555 Goat anti-Rabbit IgG (1:500) (#A-21428, ThermoFisher Scientific) and Alexa Fluor® 488 Goat anti-Mouse IgG (1:500) (#A-11001, ThermoFisher Scientific) or Alexa Fluor® 647 Goat anti-Mouse IgG (1:500) (#A-21235, ThermoFisher Scientific) once again in DAKO Antibody Diluent. After washing with 0.05% TWEEN®, the nuclei were labeled with DAPI (1:1000) (#D9542-1MG, Sigma Aldrich) for 10 min. One last round of washing, this time in PBS was required before mounting the slides with VECTASHIELD® Antifade Mounting Medium (#H-1000-10, Vector Laboratories Inc., Burlingam CA, USA) and a coverslip sealed with clear nail polish.

Confocal Microscopy and Image Analysis

Images were acquired on a laser scanning confocal microscope Zeiss LSM 5 Exciter (Carl Zeiss AG, Oberkochen, Germany) at 20X magnification. Other images, specifically for nuclei analysis, were acquired on an IX81 microscope (Olympus Corporation, Shinjuku City, Tokyo, Japan) using FITC, TRITC, and DAPI filter sets under oil immersion at 40X. Image analysis was performed using ImageJ™. For progerin and lamin A quantification, as well as nuclei morphology, the exposure was kept constant across all samples. Nuclei were detected with the

lamin A channel, the image was transformed into a binary one to generate a mask via which the Particle Analysis function could be performed on the original progerin and lamin A channels. The results obtained included the number of nuclei analyzed per image, the area, the mean gray value for each particle detected as well as its maximum and minimum gray values, the circularity and roundness, previously described. Cytoskeletal alignment studies were performed by feeding unaltered LSM files to the Directionality plug in and extracting the direction, the amount, the dispersion and the goodness of the fit. An average of 25 images were acquired per sample for both nuclei analysis and for the Directionality plug in.

STATISTICAL ANALYSES

All quantitative results were compiled and organized automatically in macro-enabled Excel™ files. Results were then either entered into JMP13™ and JMP14™ (SAS Institute, Cary NC, USA) or handled in Python using Pandas for statistical analysis. Significant interactions were first identified via ANOVA, then comparisons of means were performed with Tukey-Kramer HSD, using $\alpha=0.05$. Graphs were made with GraphPad Prism v. 6.01 (GraphPad Software, San Diego CA, USA), as well as seaborn and matplotlip.pyplot in Python.

5. RESULTS

The first part of this thesis consisted in obtaining ECs from iPSCs using a differentiation protocol adapted from Sahara *et. al*. The phenotype of the differentiated cells was studied via microscopy and surface marker analysis via flow cytometry. This gave an idea of how efficient the differentiation protocol used was when using both healthy and HGPS iPSCs. More functionally, endothelial phenotype was confirmed by staining for VWF. The second objective was to develop a staining protocol to detect progerin reliably in positive controls consisting of HGPS fibroblasts, as well as to determine whether ECs derived from the differentiation protocol displayed progerin accumulation. Lastly, as a first step towards assessing the effect of aging on iPSC-EC function, this thesis aimed at exposing different model EC types to shear stress using a parallel-plate flow chamber system and identifying methods to analyze their response to this shear stress. These included looking at the morphology with and without shear stress using confocal imaging. Focussing on cytoskeletal and nuclear rearrangements, actin filament alignment was quantified and particle analyses on stained nuclei was performed. Methods of studying the

inflammation of the cell milieu were also investigated by attempting to quantify inflammatory cytokine IL-6 and protective IL-11, as well as cell necrosis and cytotoxicity via LDH.

Assessment of Differentiation of ECs from HGPS-iPSCs

Morphological changes during HGPS-iPSC differentiation towards ECs

One method used to assess the progression of differentiation was to visualize changes in morphology from iPSC to EC using light microscopy. As seen in **Figure 10**, iPSCs exhibit a tightly packed rounded morphology in colonies with distinct borders and well-defined edges characteristic of stem cell colonies. Somewhat visible on the image is their larger nucleus and much less cytoplasm. The differentiation was then initiated by separating the cell aggregates to expose single cells to Rock inhibitor. The lower-left image shows how drastically different the iPSCs look when no longer in colony formation, as they appear much less rounded. During commitment to the mesoderm lineage, the cells were exposed to CHIR and BMP-4. The upper-right microscopy image indicates that the cells remained proliferative. Some cells, especially on the outside edges of what could be referred to as colonies, slightly more elongated than others, still exhibiting a more rounded morphology, although with a larger cell body than at the beginning of the protocol. Next, treatment with Dapt and VEGF pushed the cells towards the vascular lineage, generating EPCs and finally ECs visible in the lower-right image. The confluency has increased notably due to proliferation during the protocol. Some cells appear more elongated, with a morphology reminiscent of ECs. Morphology was visibly heterogeneous prior sorting due to the presence of more rounded cells, as well as dead cells, in white, floating around. In brief, the differentiation protocol appeared to cause changes in the morphology of the cells consistent with gaining an EC phenotype. However, morphology is not a quantifiable nor an absolute method of identifying this phenotype.

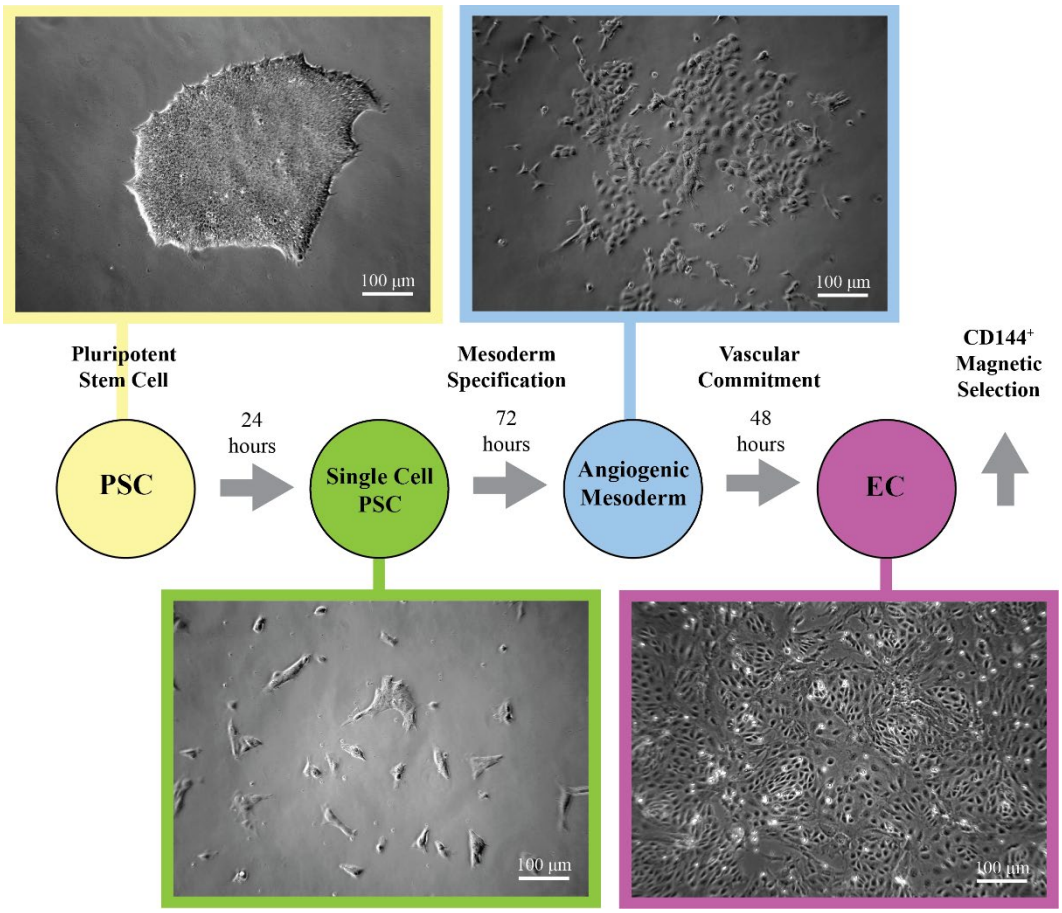

Figure 10: *Representative phase contrast images at 10x magnification showing the morphology throughout the differentiation protocol from iPSC to EC . The upper-left image shows an iPSC colony prior to the beginning of differentiation; the lower-left shows single-cell iPSCs after one day of exposure to Rock inhibitor; upper-right depicts some cells that have committed to the mesoderm lineage after three days of exposure to CHIR and BMP-4; lower-right shows the cells resulting from exposure to VEGF and Dapt prior to cell sorting, a fraction of which are ECs. Dead cells are visible in white. Protocol was performed 3 times with each cell line and ~5 images were captured at each stage.*

Surface marker profiling during HGPS-iPSC differentiation towards ECs

On day 6 of the differentiation protocol, prior to cell sorting, endothelial cell phenotype was assessed by studying cell surface markers via flow cytometry as shown in **Figure 11**. Overall differentiation efficiency could be determined by looking at the percentage of $CD144^+$ events in the live-cell population. When comparing ECs obtained from HGPS-iPSCs to those obtained from healthy donors' iPSCs, differentiation efficiencies were found to be respectively 23.39% ± 9.06% and 17.61% ± 10.01%, but not statistically significant. This differentiation efficiency around 20% is much lower than the >50% reported by Sahara *et al.*[116] TRA-1-60 expression was mostly lost

after six days of differentiation. However, around 12.7% of HGPS and 15.28% of control cells seemed to retain some degree of pluripotency, but there is no statistically significant difference between the two types. The presence of pluripotent cells was puzzling when considering that nearly the entire cell population expressed CD146 based on flow cytometry. This suggests that CD146 may not be an appropriate marker of differentiation for this specific protocol. No statistically significant differences in the proportion of $CD31^+$ and $CD34^+$ populations were noted between HGPS and non-HGPS cells. On average, 16.8% of cells were $CD31^+$ and 18.7% were $CD34^+$, which is statistically close to the differentiation efficiency of 20%. This suggests the expected presence of a population of ECs and EPCs that are $CD144^+$, $CD31^+$ and $CD34^+$. Looking at CD309, there is once again no statistically significant difference the rate of positive events between mutated and control samples. $CD309^+$ events seem to have a higher incidence level at around 40% of live cells, which could indicate the presence of a progenitor cells that have not yet differentiated into EPCs or ECs.

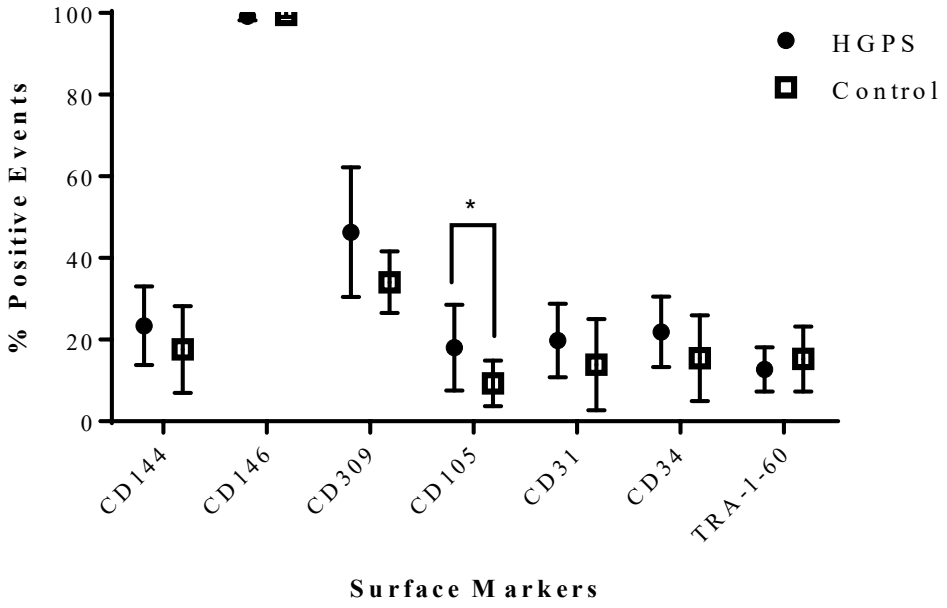

Figure 11: *Flow cytometry analysis of surface markers prior to VE-cadherin $^+$ selection shows no statistically significant difference between ECs derived from iPSCs with and without the HGPS mutation, except for CD105, which appears to be slightly higher in the HGPS group when comparing means using Tuckey Kramer HSD with $\alpha=0.05$. Graph depicts the mean with standard deviation (n=9).*

As seen in **Figure 11**, the only statistical difference between HGPS and non-HGPS groups in terms of endothelial marker expression at the endothelial specification stage of differentiation seems to be in the rate of $CD105^+$ events, when performing a comparison of means using Tuckey Kramer HSD (honestly significant difference). Around 18% of HGPS cells were $CD105^+$ compared to only 9.28% in the control group. When looking more closely at levels for the three iPSC cell lines used for each of the two conditions, it seems that the difference in $CD105^+$ rates between HGPS and control stems from iPSCs HGFDFN 168 1D2 and 1P, which are from a parent control, being significantly lower than iPSCs HGADFN 003 1C, which carry the mutation. As shown in **Figure 12**, Tuckey Kramer HSD analysis indicates that no other pair shows a statistically significance in $CD105^+$ occurrence. In other words, the difference is most likely due to heterogeneity between the different iPSC cell lines instead of being caused by the presence of the HGPS mutation. Consequently, surface marker analysis shows that HGPS-iPSCs and control-iPSCs respond similarly to the differentiation protocol, yielding around 20% VE-cadherin$^+$ cells with comparable surface marker expression. Although efficiencies can vary, after isolation, the cells obtained are 99% $CD144^+CD105^+CD31^+$. However, these cells were found to have extremely low proliferation, especially after cryopreservation. This led to low cell numbers for further analysis. Additionally, the iPSC-ECs that did manage to proliferate enough to warrant passaging showed a decrease in CD144-positivity rate.

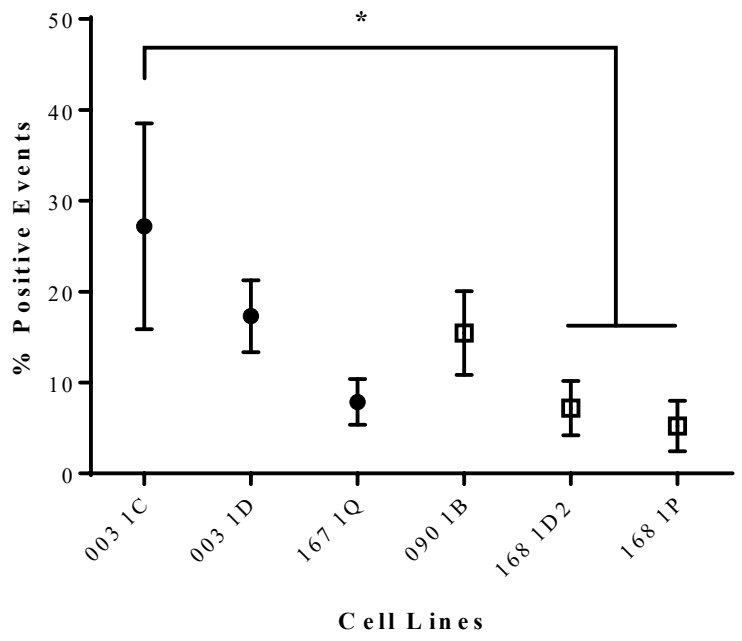

Figure 12: *Flow cytometry analysis of CD105 on iPSC cell lines after 6 days of differentiation . Circles represent the mean cell lines with the HGPS mutation and squares are the mean for control cell lines. Error bars are the standard deviation (n=3). Comparison of means using Tuckey Kramer HSD analysis indicates that the only significant difference in expression levels is between the cell line HGADFN 003 1C and the two cell lines originating from healthy donor #168.*

Following $CD144^{+}$ cell sorting, endothelial phenotype was confirmed by staining for vWF and visualizing via confocal fluorescence microscopy. As seen in **Figure 13**, there is no qualitative difference between levels of vWF in ECs originating from both HGPS and control iPSCs. The slight difference in red fluorescence in the pictures chosen is due to the height of the section imaged by the laser confocal microscope. vWF was also detected in the positive control consisting of HUVECs, which are known to express this glycoprotein. In all three images, vWF seems to be localized in the cytoplasm, primarily around the nucleus, which is consistent with what has been reported in the literature for intracellular vWF. Furthermore, the images show a similar morphology for the HGPS and control iPSC-ECs compared to the positive control. Consequently, this result validates the staining protocol used for vWF and the confirms endothelial phenotype of the cells to be used in subsequent experiments.

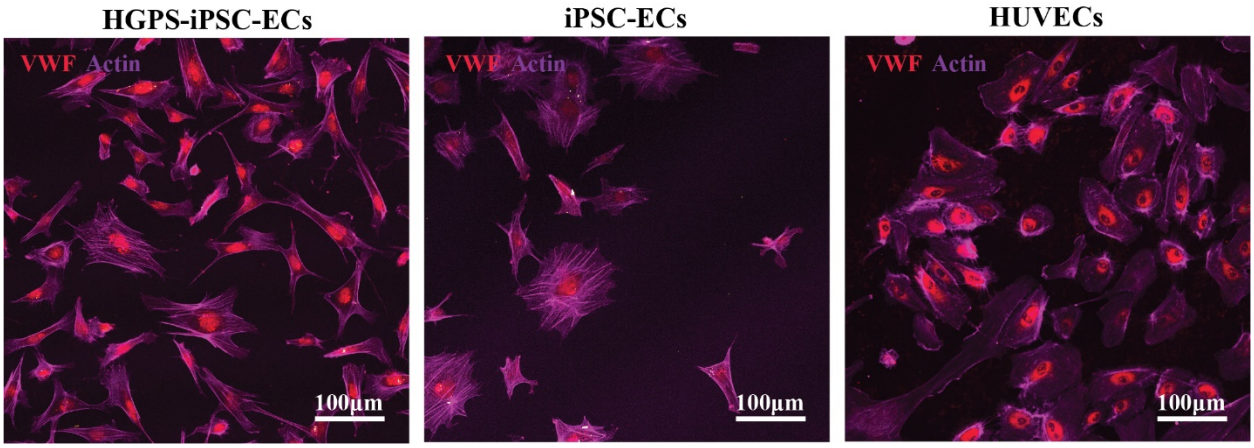

Figure 13: *Representative confocal microscopy images showing the presence of von Willebrand Factor (in red) detected in ECs derived from iPSCs with and without the HGPS mutation as well as in HUVECs, which act as a positive control of endothelial lineage. Actin filaments stained with phalloidin are visible in purple. Although there appear to be fewer iPSC-ECs, there was no quantifiable difference in confluence between HGPS and normal iPSC-EC slides.*

Assessment of Nuclear Scaffolding Abnormalities during HGPS-iPSC differentiation towards ECs

Since the long-term goal is to assess how HGPS-iPSC-ECs respond to hemodynamic stress, it must first be determined whether progerin is expressed in those cells. Robust and reproducible detection methods are required to investigate the role of progerin and age-associated prelamin A accumulation on EC mechanosensitivity and the impact that may have on EC dysfunction initiating atherosclerosis in vascular aging. To this end, progerin was stained using a monoclonal antibody from Millipore Sigma. Antibodies from other companies had also been tried, but the one from Millipore Sigma performed the best in the positive and negative controls. The positive control was chosen to be fibroblasts from HGPS patients, since they are a cell type known to express high levels of progerin. Negative controls consisted of the same cell type, this time from the parents of patients who do not carry the HGPS mutation. As seen in **Figure 14**, progerin was detected in the HGPS fibroblasts and not in healthy fibroblasts. Most, but not all, HGPS nuclei had elevated signals for progerin. Concurrent staining of both samples were also stained with lamin A showed that the elements labelled by the anti-progerin and the anti-lamin A antibodies are not the same. This means that the antibodies used are specific enough for the purposes of this research, and that the staining protocol allows for the accurate visualization of both lamin A and its aberrant form, progerin. The nuclear envelope of the HGPS fibroblasts seems less smooth than that of the negative

control. The nuclei are less uniform and exhibit a blebbed morphology. There is a visible decrease in the nucleoplasmic pool of lamin A. Conversely, the HGPS fibroblasts with less to no progerin accumulation displayed a normal morphology with uniform DAPI staining intensity – i.e. DNA distribution.

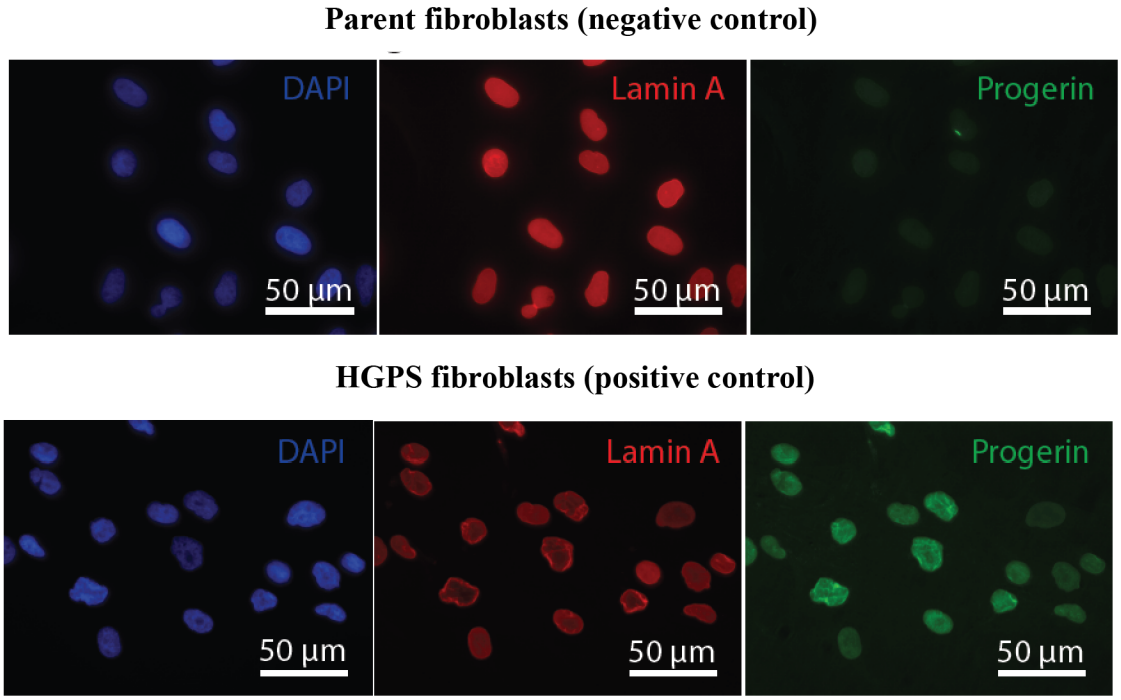

Figure 14: *Representative fluorescence microscopy images showing the presence of progerin (green) in fibroblasts from donors with HGPS compared to their parent's . HGPS fibroblasts also show blebbing of the nuclear envelope, as well altered nuclear shape and chromatin organization, visualized by lamin A (red) and DAPI (blue).*

This qualitative assessment of nuclear morphology was consistent with morphological hallmarks of progerin accumulation in HGPS. However, to improve on this methodology, a quantitative image analysis was required. Fluorescent signals acquired by using the same and exposure and capture settings for samples stained for progerin and lamin A were compared using the Particle Analysis feature of ImageJ™. **Figure 15** shows color-coded beeswarm SuperPlots generated by calculating the mean gray value for the fluorescence signals of progerin and lamin A of many nuclei in three separate samples for both HGPS and control fibroblast cell lines[137]. Pooling all the HGPS nuclei detected to compare them to the control nuclei lead to a large sample size n. However, this pooling is not statistically robust since the nuclei are not truly independent samples, and only three biological replicates were performed.

Using a large n can lead to smaller p-value that is in fact not representative of the reproducibility of the experiment. Thus, beeswarm plots were used to identify whether variability between experimental replicates eclipsed cell-level variability. Looking at **Figure 15**, the levels of progerin were significantly higher in HGPS samples than in the controls since the mean gray value for the former was of 332 ± 255 compared to 86 ± 176. Colour-coding shows that, especially for progerin, there also visible variation between biological replicates, especially HGFDFN168 sample 2. Both HGPS lines were still consistently at higher levels than the two controls. The variation on HGPS samples was higher than in the controls. This is hypothesized to be due to HGPS nuclei expressing different levels of progerin, some potentially not expressing any. The non-zero mean gray values for the controls, mainly caused by a cluster of HGFDFN168 sample 2 nuclei, should have been nearly fully negative for progerin, in other words close to zero. This phenomenon may be due to bleeding from the TRITC channel to the FITC channel and background fluorescence. These factors cannot be neglected when looking at progerin detection with microscopy. When it comes to the lamin A signal, **Figure 15** shows that, once again, there was clustering of the biological replicates with slight variation between each group of nuclei. However, this variation between the groups did not seem to dominate over the variability at the level of detected nuclei. When pooled, HGPS samples showed a significantly different lamin A mean gray value compared to the control group, with 595 ± 110 compared to 552 ± 95 mean gray units. This result is somewhat inconsistent with the decrease in nucleoplasmic A-type lamins normally associated with progeria. The statistical significance of this result mainly came from the large n used when pooling. The difference between the two groups was small (-43.00 ± 8.885) compared to the variation within samples. It is also probable that the fluorescence signal from progerin contributed to the lamin A signal. To avoid this caveat for future experiments using this specific analysis method, single stain controls could be used to correct for compensation numerically, or samples could not be stained with the two antibodies at the same time. However, the latter is both more time and resource consuming, and does not allow for the colocalization of progerin and lamin A. Alternatively, the conjugates could be chosen to have emission wavelengths further apart in the spectrum, but the filter sets in the fluorescence microscope available pose a limit to this.

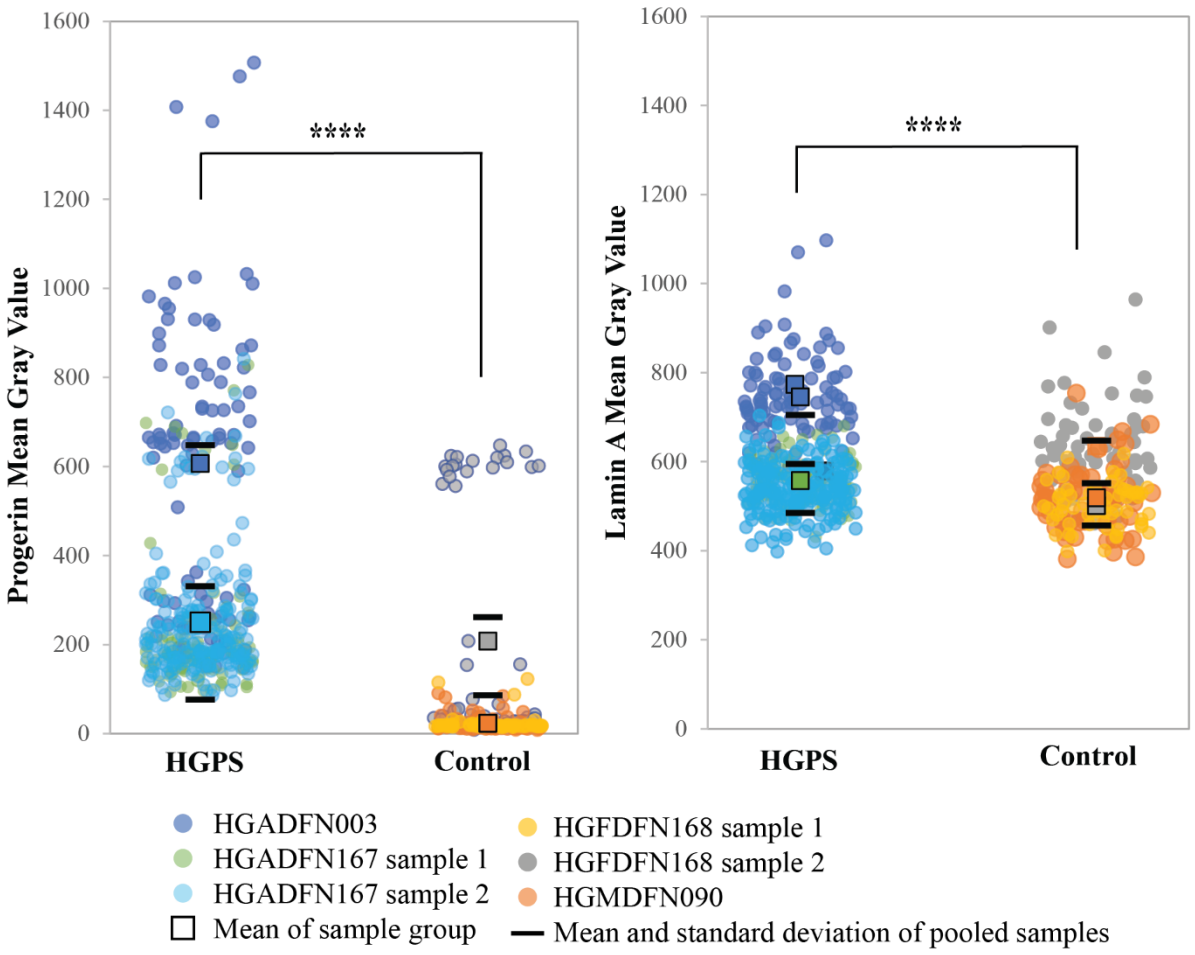

Figure 15: *SuperPlots of mean gray values obtained from Particle Analysis performed on progerin and lamin A channels of two fibroblast lines positive for the HGPS mutation and two parent fibroblast lines. Graphs show the mean and standard deviation, number of images analyzed between 18 and 34, number of analyzed particles between 62 and 292. Comparison of means using Tuckey Kramer HSD analysis shows that HGPS cell lines have higher progerin and lamin A fluorescence signals than control cells (**** means $p<0.0001$)*

Further analysis was performed on detected nuclei to examine their shape and determine whether circularity and roundness could be used to assess blebbing or abnormal nuclear morphology associated with HGPS. **Figure 16** shows color-coded beeswarm SuperPlots generated by calculating the circularity and roundness of many nuclei in three separate samples for both HGPS and control fibroblast cell lines[137]. For both roundness and circularity, the color-coding shows that there is no visible clustering of the biological replicates. In other words, the variability at the level of the detected nuclei dominated. When pooled, HGPS samples had lower circularity, with an average of 0.46 ± 0.18, compared with the controls, which had an

average of 0.72 ± 0.11. This result was statistically significant when using the number of biological replicates (n=3) to perform a comparison of means test with a computed p-value of 0.0124. This result is consistent with nuclear blebbing, which would cause an increased perimeter for the detected particles compared to the more uniform edge of healthy nuclei, and therefore a decreased value for circularity according to Equation 3. When it comes to roundness, as seen on the right of **Figure 16**, there was no statistically significant difference between HGPS and control samples when n=3 was used. This suggests that the cell-level variability was too high to draw reproducible conclusions distinguishing the roundness of either group. However, roundness investigation may be more relevant under dynamic conditions as opposed to static.

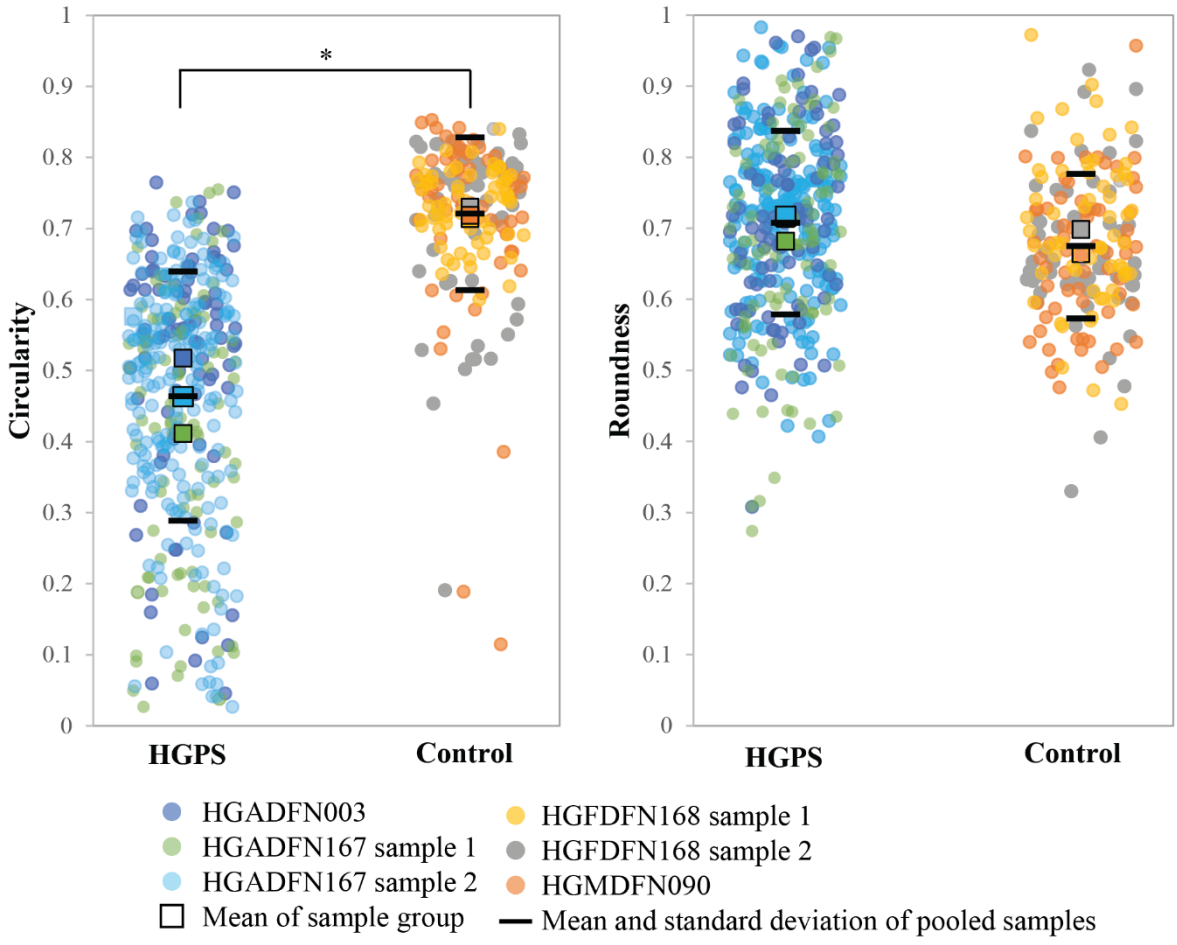

Figure 16: *Circularity and roundness SuperPlots obtained from Particle Analysis performed on lamin A channels of two fibroblast lines positive for the HGPS mutation and two parent fibroblast lines.. Graphs show the mean and standard deviation for each sample group (with n between 62 and 292 for each group. Comparison of means using Tuckey Kramer HSD analysis with n=3. (* means p<0.05)*

After successfully detecting progerin via fluorescence microscopy in positive and negative control fibroblasts, the next step involved determining whether progerin could also be detected in ECs obtained from differentiating iPSCs. **Figure 17** compares representative images of iPSC-ECs with and without the HGPS mutation to the positive control consisting of HGPS-fibroblasts. The ECs derived from progeria patients, visible on the right-hand side, show most nuclei being positive for progerin, with some nuclei having a much stronger signal than others. This pattern is reminiscent of the positive control. Interestingly, some ECs derived from healthy iPSCs also expressed progerin based on immunofluorescence detection. iPSC-ECs with and without the mutation both showed a high number of multinucleated cells and nuclei with aberrant morphologies characteristic of laminopathies and aging. Combined with the low proliferation of the iPSC-ECs, this suggests that the differentiation protocol used yields a population of aged-like ECs. This is a big caveat when studying aging, accelerated aging diseases and atherosclerosis.

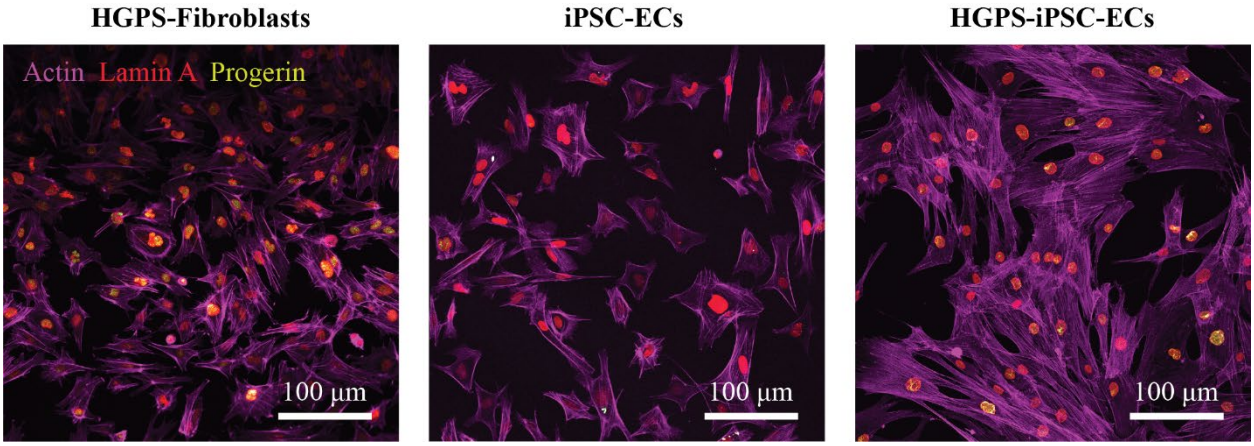

Figure 17: *Representative confocal microscopy images showing the presence of progerin (yellow-green) in the nuclei of ECs obtained from differentiating iPSCs derived from HGPS donors compared to the positive control chosen as being HGPS-fibroblasts. A small amount of progerin is also visible in ECs derived from healthy iPSCs. The pictures also show lamin A (red) at the nuclear envelope and actin filaments (purple) stained with phalloidin. Images were chosen from 75 images obtained via 3 experimental replicates.*

Quantification of actin filament alignment in the flow direction

Cytoskeletal alignment in the direction of the flow was investigated by staining HSVECs and HUVECs cultured under both static conditions and after shear-stress exposure in the flow chamber system with phalloidin to visualize actin filaments using a confocal microscope. The results were obtained by feeding 25 images for all test conditions (static and dynamic, HUVECs and HSVECs, and three separate perfusion experiments) into ImageJ™ and using the Directionality plug in to find the preferred orientation of pixels. **Figure 18 A** and **C** show representative images of the microscopy pictures fed into the software, and how the Fourier transform identifies the direction of pixels corresponding to actin filaments. From these images, multiple cells within each picture thus participate in the making of corresponding direction or orientation graphs (**B** and **D**). However, the number of cells in each image was not computed, and therefore not used to weigh more heavily the contribution of more densely populated images in the combined averages of conditions. Graphs B and D show how a static sample was associated with more isotropic pixel orientation, which lead to a flat histogram, whereas a dynamic sample displayed a preferred orientation in the direction of the flow, made visible by a broad peak in the histogram around 0°.

Figure 18 D displays actin filament alignment of HSVECs and HUVECs in the direction of shear stress in a similar fashion. The shape of their preferred orientation histogram was also significantly different from the histogram generated by their static counterparts. Fitting a curve to dynamic samples resulted in a bell-shaped probability density function centered around 0°, suggesting that the probability of finding actin filaments aligned in the direction of the flow is higher under dynamic conditions. Alternatively, static conditions led to fits that were much flatter, thus more equal probabilities across orientations. Static HUVECs did display slight peaks around 30° and 50°, but these do not seem to follow an explainable pattern. HUVECs exposed to shear stress appeared to generate a fit that was lower than that of HSVECs, although the actual pixel direction data could not show a statistically significant difference between the two. The fit diversion combined with the slight peaks in the static HUVECs samples could be hint to the possibility of the HUVECs used not being as sensitive to shear stress or “good at alignment” as

the HSVECs. This could be due to higher slightly passaging numbers for the HUVECs (P10-13 compared to P5-7 for HSVECs) or their developmental and biological nature. Although, in principle, HUVECs could alternatively be considered less mature than HSVECs from older patients since they come from the umbilical vein.

Lastly, Directionality analysis was found to be highly similar between different flow chamber experiments. **Figure S4** in the Appendix shows the confidence in the reproducibility of biological replicates using this method.

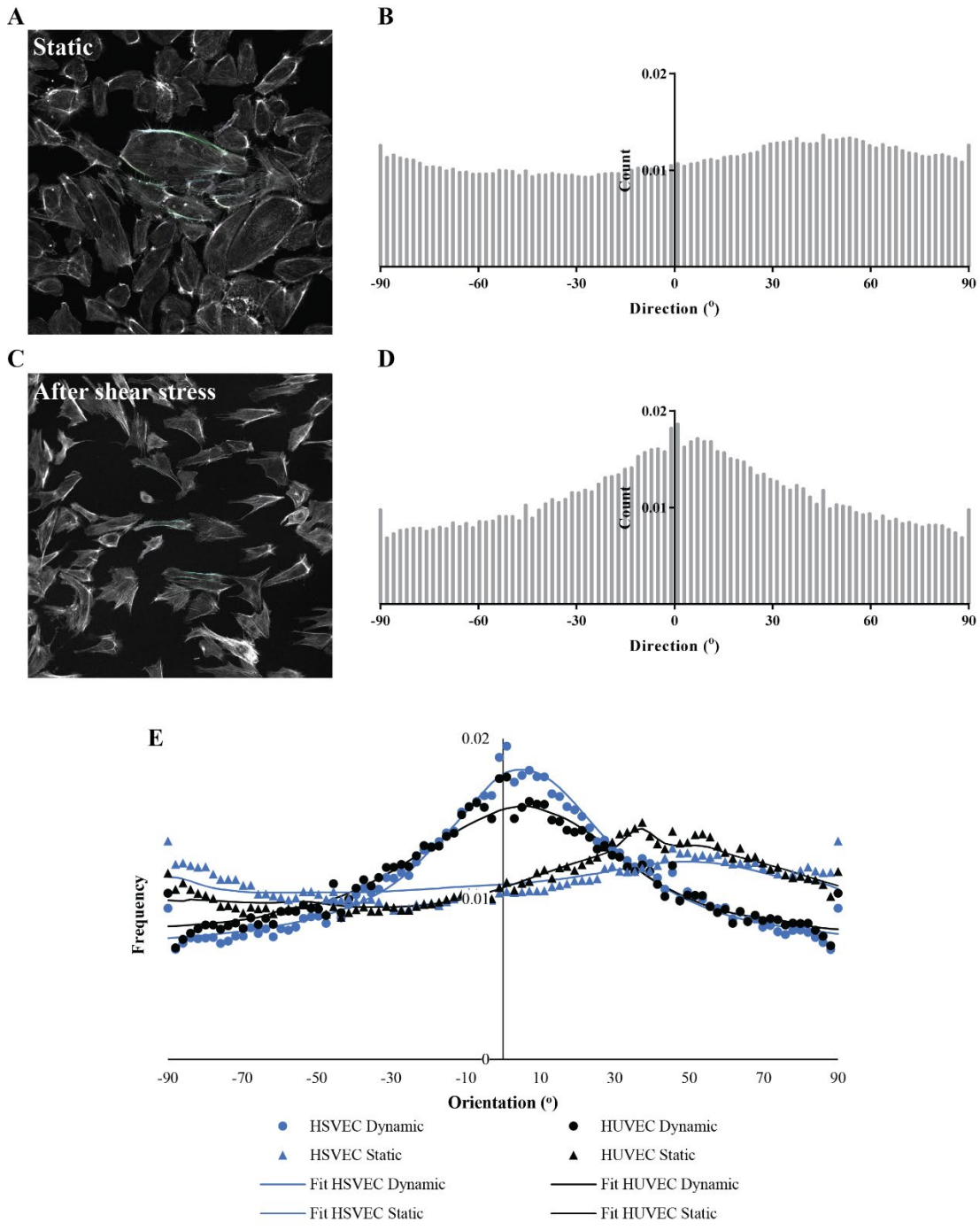

Figure 18: *Results from Directionality analysis on ImageJ. showing representative images of HUVECs under static culture conditions (A) and after exposure to shear stress in the flow chamber (C) stained with phalloidin to investigate actin filament alignment used to compute their Fourier power spectra. The graphs show the preferred orientation of structures in the input images at angles from -90° to 90°, with 0° being horizontal. The static samples (n=50) (B) show a more even distribution for the directions, whereas dynamic samples (n=175) (D) show a preferred orientation around 0°C. (E) shows the similarity in alignment between HUVECs and HSVECs, as well as the respective fit for a probability distribution function of directionality.*

Quantification of nuclear alignment in response to flow

Changes in nuclear shape and alignment in the direction of the flow are more subtle than cytoskeletal ones since nuclear shape is typically more uniform than cell shape. However, robust quantitative assessment of nuclear alignment was an important objective in this thesis. Hence, using nuclear envelope staining combined with the Particle Analysis tool in ImageJ™ images of HUVECs and HSVECs under static and dynamic conditions were compared. SuperPlots, seen in **Figure 19**, were generated to visualize the distribution of aspect ratios, circularity and roundness values as well as measures of the angle made between the major axis of ellipsoidal-shaped nuclei. There were no significant differences between any of the averages for two groups and two conditions, but this was to be expected due to the large standard deviations combined with low statistical power from few true biological replicates (recall **Figure 16**). Similar distributions were observed for HSVECs and HUVECs in all types of measurements, suggesting no difference in nuclear shape and alignment between admittedly "younger" HUVECs and HSVECs harvested from older donors. Hence, both types of cells could be considered as healthy controls in future experiments.

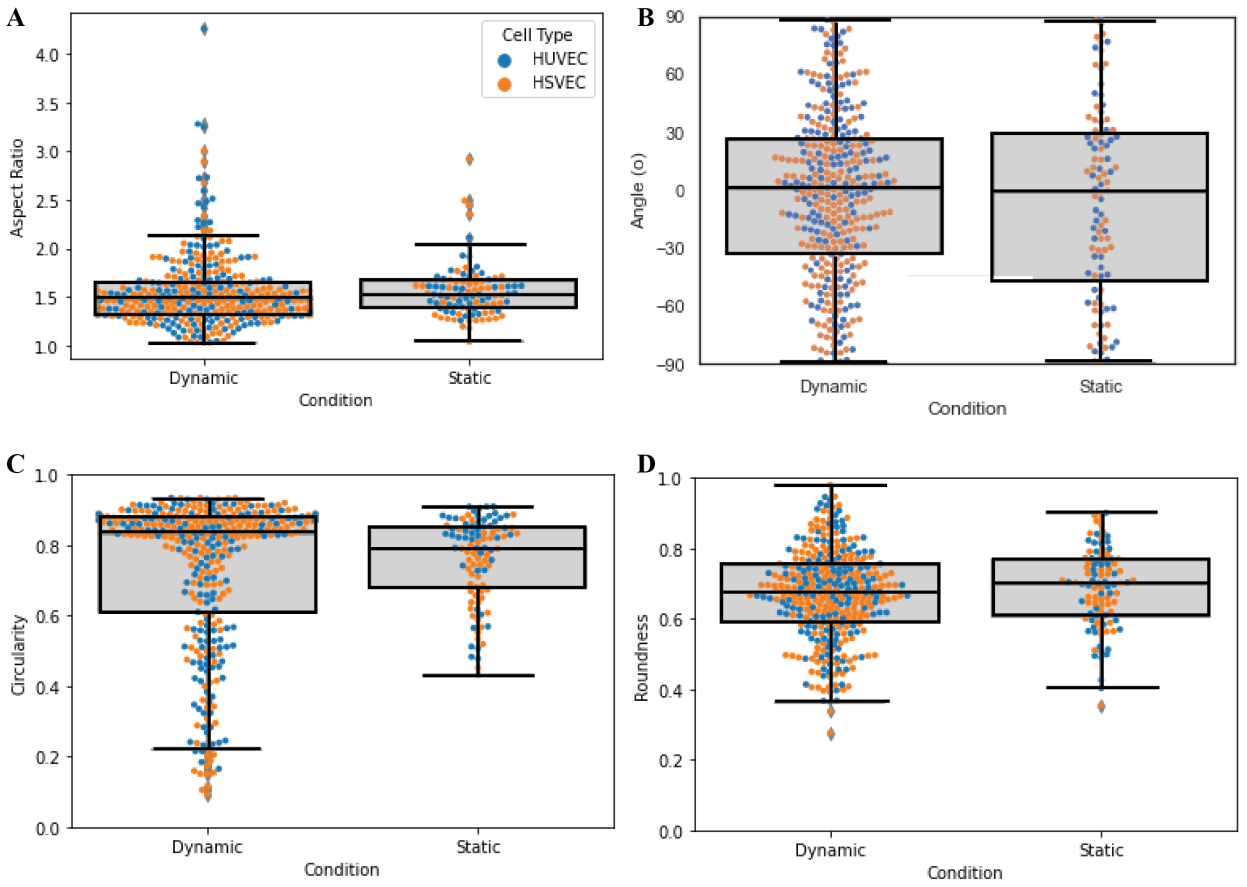

Figure 19: *SuperPlots from Particle Analysis in ImageJ to compare nuclear shape between static and dynamic samples . The aspect ratio (A), the angle the major axis makes with the horizontal axis (direction of the flow) (B), the circularity (C) and the roundness (D) of HUVECs (in blue) and HSVECs (in orange) under static and dynamic conditions are depicted in beeswarm plots overlayed on corresponding boxplots.*

Further analysis of the angle made between the major axis of a nucleus and the direction of the flow shows a preferred orientation at 0^{o} following exposure to shear stress. In **Figure 20** the presence of a broad peak for the dynamic nuclei as opposed to the flatter, thus more isotropic, distribution for static nuclei. This conclusion highlights the need for rigorous statistics when it comes to image analysis since a significant result could have been overlooked by the fact that the averages for both distributions were close to zero, and low number of biological replicates gave low statistical power to differences of variance calculation when the distributions are so wide. Using a probability density function fitting via kernel density estimation (KDE), on the other hand, showed that nuclei exposed to shear stress have a statistically significant greater probability of being found oriented with the flow than under static conditions.

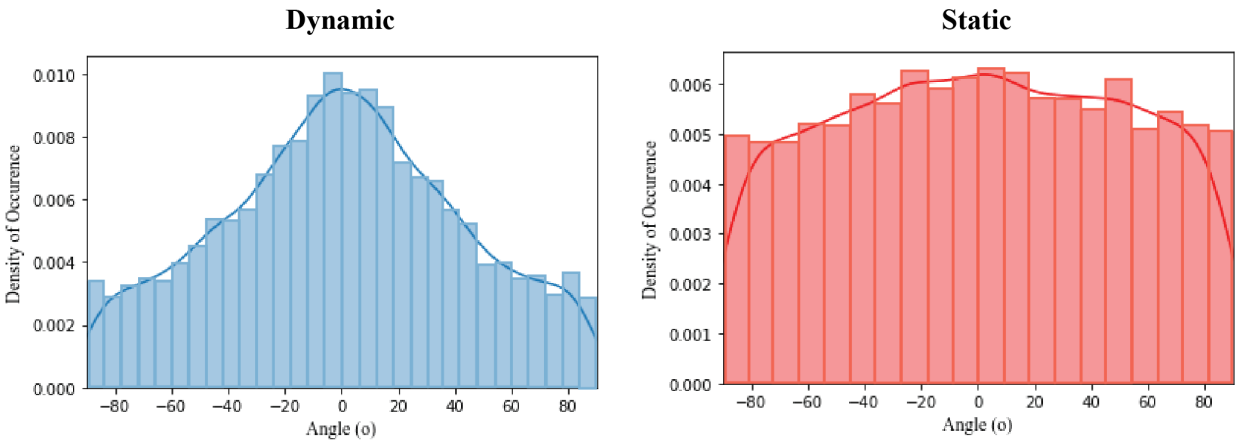

Figure 20: *Histograms comparing the orientation of the major axis of combined HSVEC and HUVEC nuclei with and without exposure to shear stress. The plots are fitted with a kernel density estimation (KDE) to estimate the probability density function of finding a nucleus within a given angle range. Nuclei exposed to dynamic conditions appear to have a greater probability to be oriented in the direction of the flow, whereas the static conditions seem to generate more randomly distributed major axis orientation (according to simple t-tests on the KDEs with Gaussian approximation for angles between -30º and 30º).*

Inflammation of Endothelial Cells Exposed to Shear Stress

The methods to investigate the immune response via cytokine secretion, cell death and adhesion of leukocytes in a flow chamber system were developed in the context of examining ECs cultured on surfaces functionalized with fibronectin-derived peptides. An adult and "aged" model compared to conventionally used HUVECs was applied in these studies, with the perspective of future application to HGPS-iPSC-ECs.

For cytokine quantification, the concentrations of pro-inflammatory IL-6 and anti-inflammatory IL-11 were measured using ELISA kits. The calibration curves for both experiments can be found in the Appendix (**Figures S4** and **S5**). For each experimental condition two samples of the perfused media were taken after high shear stress exposure and two more samples after the circulation of NB4 cells for 1 hour. **Figure 21 A** and **B** show that samples under the same condition and from the same experiment (same colour) gave approximately the same concentrations for both cytokines. However, the variation between experimental batches within each condition was extremely high. This suggests manipulation discrepancies such between experiments may significantly impact cytokine levels measured. For example, the low ratio of number of studied cells to flowing media volume may have led to large discrepancies (for the scale) of cytokine concentrations from only slight changes in

perfused volume or seeding density. Further evidence of this is found in the graph for IL-6 that shows that some of the concentrations were calculated to be negative from the calibration, indicating that those concentrations were below the detection limit of the test, although a high sensitivity test was selected. There was also no significant difference, even when results were pooled for the concentrations of IL-6 and IL-11 between samples before the addition of NB4s and after. For 1-hour long perfusion, a high circulating concentration of NB4s stimulated with ATRA did not significantly contribute to raising the concentrations inflammatory cytokines. Together, these findings suggest that results from ELISAs of different flow chamber experiments should not be pooled for statistical analysis due to low reproducibility and that immune cells may need much more than 1 hour to secrete detectable levels of interleukins in this system.

Cytotoxicity induced by shear stress exposure was also quantified from circulating media sample using an LDH calorimetric assay. Even with lyophilization to achieve higher LDH concentrations, the absorbance readings remained below or close to detection limits of the assay. Triplicate samples were generated from each flow chamber experiment (different colours seen in **Figure 21 C**) and for each condition to assess reproducibility. Although readings for those triplicates did seem to cluster, in some instances, they covered a wide range of absorbance values. The variation between different experiments for a single condition was also too large to identify any statistical difference between conditions. As for the comparison between pre and post-NB4 perfusion, the absorbance readings for samples taken after the 1-hour perfusion seemed generally lower than the ones before, although the statistical power behind this statement depends on the choice of n between true biological replicates (in this case 7 flow chamber experiments), or the number of triplicated conditions pooled. Choosing the latter would mean that post-NB4 readings were statistically lower than pre-NB4, which is a surprising result considering that the perfusion added more cells into the system, thus increasing the concentration of cells that could leak LDH into the media, and that using live-cell imaging, NB4 cell death was visible during the perfusion, with an increased presence of cell debris. It is possible that even with the lyophilization and reconstitution step, the concentration of LDH was too low to show differences between conditions.

The leukocyte adhesion assessment of inflammation using ATRA-stimulated NB4 cells perfused onto ECs after their exposure to high shear stress consisted of counting the number of cells attached to the endothelial monolayer from phase contrast microscopy images. The

assumption behind this approach is that a higher number of adhered NB4s correlates with higher inflammation. **Figure 21 E** displays representative images of the before and after NB4 microscopy pictures from which leukocytes were counted. They are boxed in green in the picture on the lower right corner. NB4 not only adhered to the ECs, but also to the culture surface not covered by ECs. This was a slight caveat for the experiments focussing on comparing different surface treatments, but for future experiments with HGPS-iPSC-ECs, the culture surface would be kept constant. More importantly, although NB4 counting could not be automated and required a trained eye, as seen in **Figure 21 D**, statistically significant differences were found between certain surface treatments[2]. The variability between different flow chamber experiments was small enough to allow for reasonable pooling of counts from different conditions. This finding suggests that this leukocyte adhesion study could be robust and reproducible enough to use in future experiments with aged ECs under flow.

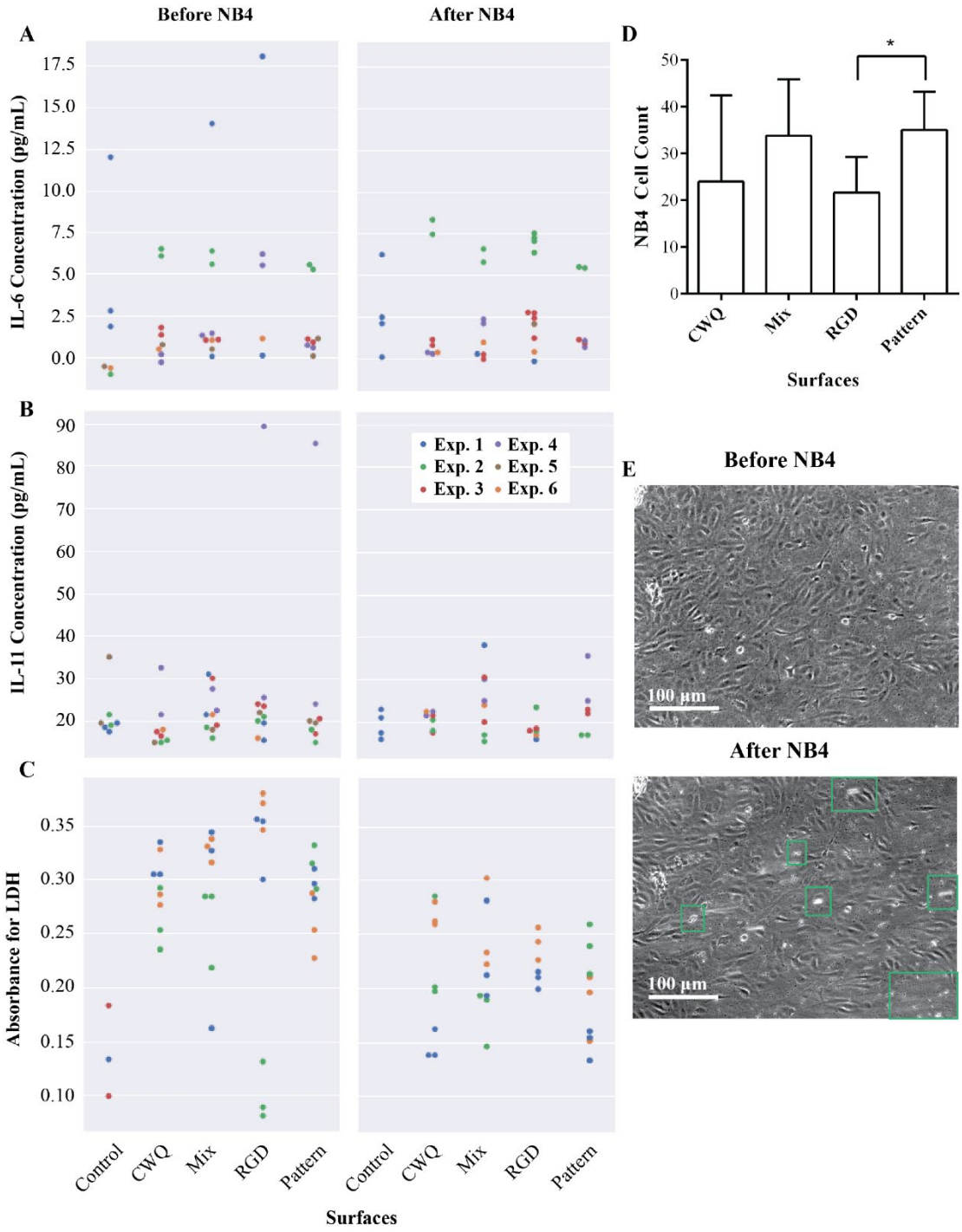

Figure 21: *Summary figure of the quantification of inflammation in response to shear stress of ECs on various surfaces using NB4 perfusion. Control stands for only media flowing. (A) displays proinflammatory cytokine IL-6 concentration and (B)anti-inflammatory IL-11 concentrations, quantified via ELISAs from cell culture media samples following shear stress exposure. Samples were taken before and after leukocyte adhesion studies. (C) shows results for LDH cytotoxicity assays obtained with a plate reader. The different colours illustrate the different flow chamber experiments, considered here biological replicates. (D) shows a histogram of manual cell count of NB4 cells adhered to the culture surface and EC monolayer following 1h-perfusion. (E) shows representative images of a sample section used for NB4 counting.*

6. DISCUSSION

The overarching goal of this thesis was to develop a platform to investigate vascular aging in ECs exposed to shear stress. The work done toward this objective generated a set of methods that can be used in combination with one-another to specifically investigate the effect of the HGPS mutation on ECs, under both static and dynamic culture conditions and potentially vascular aging in general. These methods are summarized in **Table 4** and **Figure 22**.

To achieve this, the first step was to obtain ECs from iPSCs with and without the HGPS mutation using a directed-differentiation protocol followed by $CD144^+$ magnetic cell sorting. Major advantages of using this *in vitro* approach include cost and time effectiveness compared to animal models, improvements upon serially-passaged HUVECs to mimic aging, and bypassing the low availability of ECs from HGPS patients due to the rarity of the disease and the invasiveness of vascular biopsies. The monolayer differentiation protocol from Sahara *et al.* was chosen to improve reproducibility compared to embryoid bodies-based protocols[116]. The protocol yielded lower than expected numbers of ECs, with an efficiency under 20% for both HGPS and non-HGPS iPSC lines. The resulting ECs displayed limited growth and survival after cryopreservation, which severely limited the number of experiments that could be performed with single batches, introducing reproducibility concerns. Furthermore, artificially "pushing" iPSCs down the differentiation pathway using chemical signals could lead to unwanted aging mechanisms that have yet to be identified. Healthy iPSC-ECs used as controls could in fact be themselves aged. For the future of this project, there is an clear need to improve upon this differentiation protocol to obtain more ECs which can be further expanded to improve technical feasibility of subsequent studies. The characterization iPSC-ECs using the specific combination of surface markers CD144, CD146, CD309, CD105, CD31, CD34 and TRA-1-60 using flow cytometry is unique to this thesis. The lack of significant difference across the cell lines used in the differentiation suggested that the protocol was reproducible for both HGPS and non-HGPS cell lines from various donors. Aside from CD144, which clearly segregated the population in two, the other chosen markers did not generate clearly negative and positive populations. This characterization method also showed variability in the absolute result when measurements were taken using different flow cytometers although trends remained the same. Additionally, the choice of antibody, in terms

of manufacturer, clone and conjugate also impacted reproducibility between experiments. On the other hand, the immunocytochemistry protocol developed to visualize intracellular vWF in iPSC-derived ECs and HUVECs generated highly reproducible images that confirmed endothelial phenotype. Further investigation of receptors involved in the arteriovenous specification cascade in EC development could lead to the choice of different markers of differentiation that would also show whether the ECs obtained are closer to the venous or arterial fate.

Since the long-term goal of this project was to determine whether progeria ECs respond differently to hemodynamic stress, the first stage was to see if progerin could be detected in HGPS-iPSC-ECs. Detection of progerin using immunostaining was chosen as a method over western blot since the staining protocol could be performed using small samples, requiring lower numbers of cells. The detection was also performed at the protein level and not merely at the mRNA upregulation level, which would have been the case had qPCR been chosen as a method. The staining protocol established using a highly specific anti-progerin antibody generated reproducible positive and negative controls using HGPS-fibroblasts and healthy fibroblasts respectively. This method was found to be more qualitative since quantification of progerin could not be achieved reliably using only fluorescence intensity. More importantly, using this method, progerin was detected in HGPS-iPSC-ECs, which is a novel and potentially controversial finding since progerin has mainly been detected in VSMCs as opposed to ECs[105]. Additionally, low progerin signals were also observed in iPSC-ECs from donor without the mutation. This observation further suggests that the differentiation protocol may have "aged" the ECs. Further investigation is required to verify that progerin was correctly labelled, and not some other aberrant form of lamin A that could be associated with vascular aging. Given previous observations of progerin expression in aged ECs, it is possible for mutations to accumulate with time and lead to progerin expression. ECs obtained from iPSCs could accumulate progerin due to a mutation occurring during the differentiation itself. This should be further investigated at the DNA and mRNA level at different stages of the differentiation protocol. Overall, the consecutive use of the differentiation protocol and of the progerin staining led to novel findings that open the door to future investigation.

The third aim of this thesis consisted of putting in place a unique platform allowing the Hoesli lab to study HGPS-iPSC-ECs under biologically relevant shear stress. Using a flow chamber system allowed to expose ECs to shear stress. The incubation chamber designed to be mounted on

a microscope successfully maintained conditions of 37ºC and 5% CO_2 which enabled perfusions longer than 24 hours, while imaging. A parallel-plate flow chamber system developed by Hoesli *et al.* was chosen to facilitate imaging due to the use of a flat glass slide as a culture surface and optically transparent cover. This allowed for both live-cell imaging and easy sample staining, mounting and confocal imaging after disassembly. This constitutes a significant advantage over most 3D models used in perfusion studies, while also being a limitation since glass slides are not biologically representative of vessel geometry and stiffness. Additionally, the chamber generated fully developed unidirectional laminar flow over the entirety of the culture area[2]. This meant that the endothelial cell monolayer was not exposed to turbulent or disturbed laminar flow often associated with more atheroprone regions of the vasculature. It also ensured that all the cells imaged within a sample were exposed to the same flow conditions, which was of high importance when imaging and quantifying alignment. The flow path design allowed for a range of biologically relevant shear stresses to be generated. Hence, by simply calibrating the pumps, the flow rate could be maintained at 0.2 dyn/cm^2 and subsequently at 22 dyn/cm^2 for different phases of a single experiment. The flow chamber system was developed to allow for four separate paths to be maintained, allowing for potentially four different conditions, or replicates. Although the system was highly adaptable, it was technically very difficult to set-up, with multiple fragile parts susceptible to catastrophic breakage and leakage. Hence, it required near full-time monitoring for the duration of the perfusion, which extended to over 24 hours. High variability was noted between different perfusion experiments. The complexity of the setup may have contributed to this. Linking the pumps, which are outside of the incubation cage, to the flow dampener, 8 media bottles and flow chamber required meters of tubing. This led to a requirement of about 50 mL of media for each circulation loop. Due to the small size of the sample flow chambers, the number of cells to circulating volume ratio was thus quite low. This drastically limited the tests which could be performed on the cells post shear stress exposure. For instance, cells would have been harvested in insufficient numbers to allow for proper western blotting and qPCR studies, considering the need for control among other things. Additionally, the small number of cells to media volume ratio also affected the concentration of secreted molecules, such as inflammatory cytokines and other extracellular signalling molecules, the quantification of which via ELISAs would be of great interest. Most importantly, flow chamber experiments

like the ones described in this thesis have never been performed using ECs derived from HGPS-iPSCs. The work in this thesis amounted to this being the next big step or objective, as discussed later.

The flow chamber system had to be appended with methods to investigate the effects of shear stress on EC morphology and function. These methods were conceptualized in two broad categories: (1) visualizing the alignment of cells in the direction of the flow and (2) quantifying inflammation of ECs in response to shear stress exposure. To investigate alignment in the direction of the flow, the first approach consisted of staining actin filaments of the cytoskeleton, taking representative images via fluorescence confocal microscopy and using the ImageJ Directionality software to quantify the extent of filament alignment. As hypothesized, static samples of both HSVECs and HUVECs generated images with mostly isotropic content, which led to flat directionality histograms. On the other hand, HSVECs and HUVECs that had been exposed to 22 dyn/cm^2 of shear stress generated histograms with peaks in the preferred direction of the flow. These results were highly reproducible between flow chamber experiments, which is a testament to the reproducibility of the methodology. Additionally, no significant difference was found between the behaviour of HSVECs and HUVECs, although they vary in origin and passage number. It would be interesting for future experiments to explore the possibility of ECs of arterial fate aligning more uniformly with shear stress and generating narrower orientation peaks. Overall, such quantification of cytoskeletal alignment could allow for the identification of differences in the extent of shape changes between different ECs, it has also not previously been performed using HGPS-iPSC-ECs. Other methods of investigating cell alignment in response to flow in a more dynamic method could be of interest. Using the live-cell imaging capabilities of the flow chamber set-up, phase-contrast time-lapse videos of ECs aligning could be quantified with undecimated wavelet transform-multivariate image analysis (UWT-MIA), as performed by Hoesli *et al.*[2] This could be an improvement upon the current method described in this thesis, which only offers insight before and after shear-stress exposure, and not into the dynamics of alignment.

The second approach to investigate EC response to shear stress relied on the assumption that nuclei sense mechanical forces from shear stress and align in the direction of the flow to minimize these forces[58]. Methods had to be developed to quantify these changes in nuclear shape and alignment, which more subtle and harder to distinguish compared to actin filaments. The challenge

consisted of identifying which automated image analysis measurements using nuclear staining and confocal microscopy could be used to see statistically significant differences between cells exposed to shear stress and static samples. It also involved the use of statistical and data visualization tools that could reflect these differences better than traditional averages and standard deviation. It was found from the generation of SuperPlots that the main measurement of interest was the angle formed between the long axis of an ellipsoid-shape nucleus and the axis of the flow. With a similar trend as the actin filaments, nuclei in static conditions showed no preferred orientation compared to those exposed to shear stress, which formed a broad peak in the direction of the flow. In the context of progeria, investigating specifically nuclear alignment could be of particular interest since nuclear defects are at the center of this accelerated aging disease. Considering that this thesis has shown the potential presence of progerin in HGPS-iPSC-ECs, future studies should study whether misshapen nuclei could lead to different alignment angles compared to healthy ECs.

The second category of investigations into the effects of shear on ECs focused on measuring their inflammatory response. As previously stated, the protocols discussed in this section were developed in the context of comparing the dynamic effects of various surface culture modifications[2], which was not the focus of this thesis. However, the results obtained highlighted the strengths and limitations of using such methods to investigate inflammation using the flow chamber system. Leukocyte adhesion on the endothelial monolayer was identified as one way of looking at inflammation functionally. Leukocyte adhesion is on of the hallmarks of inflammation, which is associated with vascular aging and atherosclerosis. A model of leukocyte adhesion was developed by perfusing NB4 cells stimulated with ATRA at a low flow rate in the flow chamber system after having exposed ECs to high shear stress. Although this had the advantage of being performed immediately after exposure and visualized via live-cell imaging with minimal modifications to the set-up, it remained that NB4 cells are merely a model cell line of leukocytes. Even after ATRA stimulation, they may not act like typical peripheral blood mononuclear cells (PBMCs) involved in the inflammatory cascade in blood vessels. Additionally, an unanticipated limitation was that the counting of adhered NB4 cells could not be automated with an image analysis software. NB4 cells mainly adhered to regions where the culture surface was exposed as opposed to the ECs themselves. A homogeneous endothelial monolayer was found to be technically nearly impossible to achieve,

even with high EC seeding density. It was not only difficult for an observer using phase contrast imaging to identify adhered NB4, but also questionable to include or exclude NB4 cells that were clearly adhering to the exposed surface as opposed to ECs. With these limitations in mind, the results obtained were sufficiently reproducible between biological replicates to give weight to this method. Furthermore, leukocyte adhesion assays using NB4 circulation have been used in the past to assess the inflammation of the endothelium[64], but not in the context of HGPS, nor with the flow chamber system used here.

Inflammation was further examined by quantifying the concentrations of proinflammatory cytokine IL-6 and anti-inflammatory IL-11 via ELISAs. Similarly, cytotoxic response to shear stress was quantified using an LDH calorimetric assay. For these purposes, cell media samples were collected following the exposure of ECs to shear stress, both before and after the addition of NB4 cells. Although most samples were found to be within the detection limits of each test, the variability between biological replicates of similar conditions suggested that pooling of replicated data could not lead to statistically significant differences between surface treatments, nor between the presence or absence of immune cells in circulation. This variability could be due to the low number of cells to volume ratio, which could drastically be altered by a slight change in either. In other words, since the number of cells was small, a change in the surface coverage or seeding density could lead to a significantly different secretion. Similarly, if the 50 mL-circulating volume was modified even slightly during the challenging perfusion, for such low concentrations of cytokines and LDH, the effects would seem drastic. Hence, when performing statistics, pooling should be avoided, but trends could be made visible by repeated comparisons within single experiment batches. This should be considered if further experiments are performed using these methods. Ultimately, the methods have been developed to combine the use of ELISAs and LDH assays with the flow chamber set-up, but the authors of this work recommend investigating other methods of quantifying inflammation on a molecular level. Perhaps focussing on visualization of intracellular inflammatory or cytotoxic markers with immunostaining would help avoid the low cell number to high flowing volume caveat. Additionally, the activity of AP-1, pathways like Notch/P13K and ERK/AKT as well as VEGF expression have been shown to respond to shear stress EC and could be investigated using the proposed platform.

Table 4: *Summary of methods developed*

Method	Advantages	Limitations	Novel Contribution
1. Differentiation of HGPS-iPSCs into ECs and reliable CD144$^+$ magnetic cell sorting	Using HGPS as a model for aging • Less time-consuming and expensive than animal models • Improvement upon serially passaged HUVECs • Limited supply of ECs from HGPS patients due to rarity of disease and invasiveness of vascular biopsies for the patients • Using few iPSC cell lines to avoid donor variability 2. Monolayer differentiation protocol chosen to improve reproducibility compared to 3D culture	1. Differentiation protocol from Sahara *et al.* yields lower than expected numbers of ECs (under 20% differentiation efficiency) 2. "Artificially pushing" iPSCs through differentiation into ECs could lead to some unwanted unknown aging mechanisms 3. Resulting ECs show limited growth and low survival after cryopreservation.	Applied *Sahara et al.* differentiation protocol to iPSCs from HGPS patients and non-HGPS iPSCs without significant difference in efficiency and final phenotype
1.1. Flow cytometry analysis of endothelial surface markers of differentiation	1. Confirmation of differentiation protocol reproducibility between cell lines 2. Small sample required for analysis allows for sampling for analysis at various time points with enough remaining cells for experiments	1. Different flow cytometers give different results, although show similar trends 2. Antibody choice impacts absolute results and reproducibility of experiments 3. Excluding CD144, surface markers chosen did not generate purely positive and negative groups of cells.	Specific combination of CD144, CD146, CD309, CD105, CD31, CD34 and TRA-1-60 is unique to this thesis
1.2. Optimized vWF staining and confocal microscopy	1. Confirmed endothelial phenotype of iPSC-ECs compared to HUVEC controls 2. Staining protocol generated highly reproducible images clearly localizing vWF		
1.3. Detection of progerin using immunostaining and confocal microscopy	1. Low cell numbers required for both staining and imaging (compared to using a western blot) 2. Reproducible generation of positive (HGPS-fibroblasts) and negative (healthy fibroblasts) controls. 3. Choice of anti-progerin antibody is highly specific, no staining to similarly structured lamin A 4. Detection at the protein level, not merely upregulation, which would be detected by qPCR	1. Difficult to quantify the presence of progerin using fluorescence intensity	1. Progerin was detected in HGPS-iPSC ECs, which is an important finding only recently confirmed in the literature. 2. Low progerin signals were detected in iPSC-ECs derived from donors without the HGPS mutation. Suggests that the differentiation protocol may be "aging" the ECs. More investigation is required to verify that it is really progerin that is labelled and not another aberrant form of lamin A that could be associated with vascular aging.

Method	Advantages	Limitations	Novel Contribution
2. Parallel-plate flow chamber system to expose ECs to shear stress	1. Flow chamber: • Expose cells to more biologically relevant hemodynamic conditions than static culture • Incubation chamber at 5% CO_2 and 37°C allows for multiple days of perfusion. 2. Choice of parallel-plate: • Fully laminar flow over cultured surface. Cells are not exposed to atheroprone turbulent flow • Allows for a range of shear-stresses by modulating pumps. Better than microfluidic devices that can require complete redesign • Separate flow paths allow for multiple experiments in one set-up • Allows for live-cell imaging and for easy sample staining, mounting and visualization. Advantageous compared to most 3D models.	1. Technically extremely challenging to set-up and fragile. Requires near full-time monitoring for the duration of the perfusion (almost 24h) 2. Flat glass surface is far from biological vessel geometry and stiffness. This is a limitation of the model 3. Small size of chamber leads to a small number of cells, limiting the tests that can be done (e.g. PCR, western blot). The small ratio of number of cells to volume of perfused media limits the assays that can be performed on secreted molecules (e.g. ELISAs) 4. High experiment-to-experiment variability	ECs derived from HGPS-iPSCs have not been cultured in a parallel-plate flow chamber system in the past.
2.1. Alignment quantification using fluorescence imaging			
2.1.2. Quantification of cytoskeletal alignment	Quantifiable method of investigating alignment of actin filaments in response to shear stress, automated with the use of ImageJ Directionality	Due to staining, restricted to either static or shear stress exposed samples, cannot track specific cells overtime	Cytoskeletal alignment of HGPS-ECs has not been investigated with this method previously
2.1.3. Visualization of nuclear shape and alignment	1. Quantifiable method of investigating nuclear alignment in response to shear stress 2. Could co-localize nuclei containing more progerin with those that are more deformed or do not align in the direction of the flow.	1. Changes in nuclear shape and alignment are subtle. Large sample size needed to ob significant trends 2. Due to staining procedure, restricted to with and without shear stress snapshots	HGPS-ECs have not previously been shown to display nuclear abnormalities, due to low progerin expression compared to VSMCs, but this thesis suggests otherwise.
2.2. Inflammation assessments			
2.2.1. NB4 perfusion	1. Highly functional method of investigating endothelial inflammation, one of the hallmarks of atherosclerosis and aging 2. Can be performed in the same flow chamber, immediately after exposure to high shear stress, and visualized with live-cell imaging	1. NB4 cell line merely models neutrophils 2. NB4 cells tend to adhere to the parts of the culture surface not covered by ECs 3. No method was identified to automate NB4 cell counting	Leukocyte adhesion assays using NB4 circulation have been used in the past to assess the inflammation of the endothelium[64], but not in the context of HGPS, nor with the flow chamber system used here.
2.2.2. ELISAs to quantify cytokines IL-6 and IL-11 from media	1. Well-developed and reliable assays for direct quantification of cytokines 2. Easy to collection, storage and assays	1. Low cell number-to-media volume ratio leads to low concentration of cytokines 2. High variability between experiments	-
2.2.3. LDH cytotoxicity assay on cell media to quantify cell death	1. Well developed and reliable assay 2. Easy to collect supernatants and perform assays at a later time	Low cell number-to-media volume ratio leads to low concentrations of LDH, requiring the addition of a lyophilization step	-

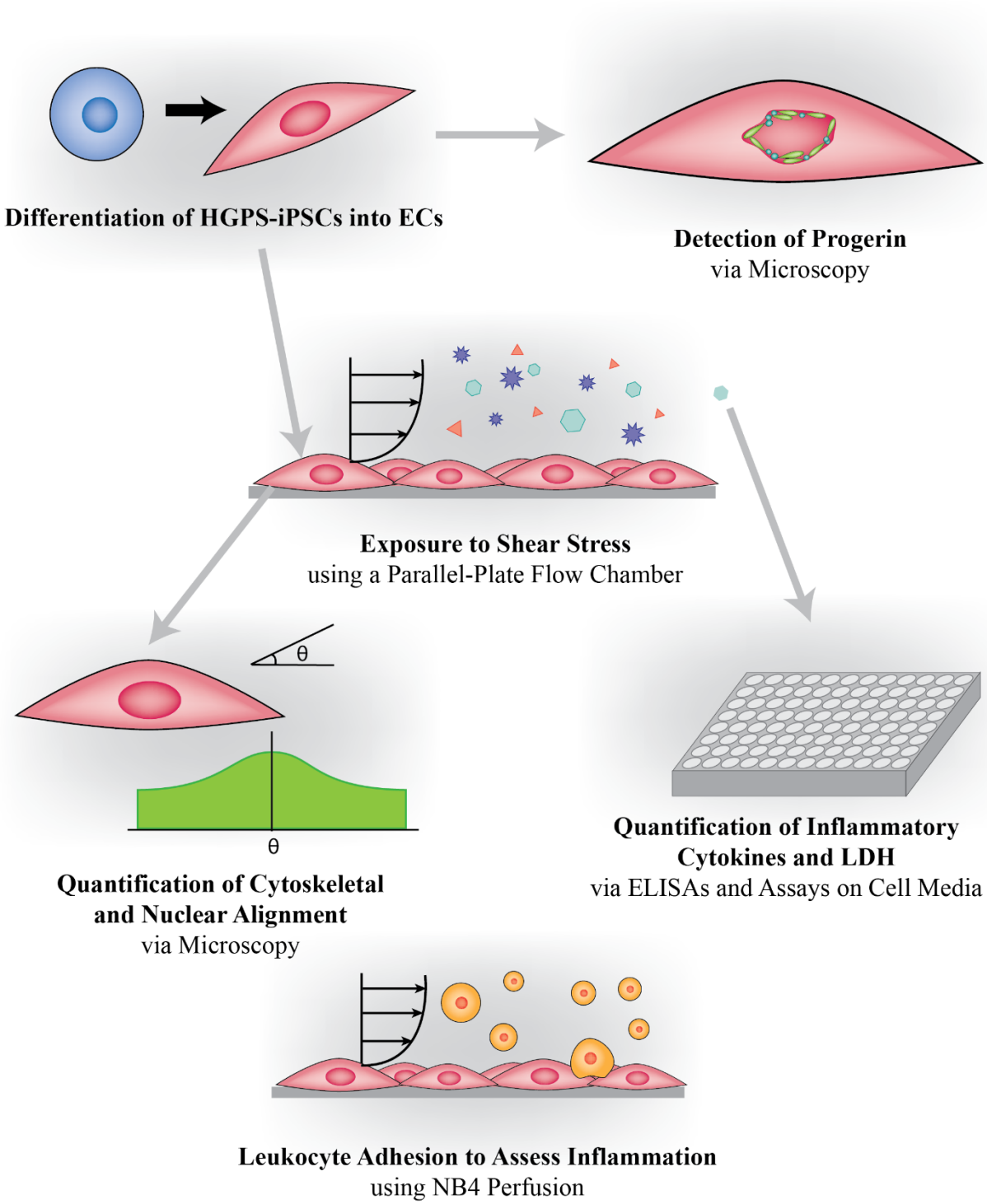

Figure 22: *Summary of the platform developed in this thesis with a unique combination of methods*

7. CONCLUSION

Aging is an important risk factor in the development of cardiovascular diseases, which are the leading cause of death around the world. Atherosclerosis, an inflammatory disease, is one of the hallmarks of cardiovascular diseases in aging. Endothelial dysfunction is an initiating event of atherosclerosis. Current in vitro models for studying vascular aging using ECs are often limited to biopsies from elderly patients, which do not help study the onset of disease, or to serially passaged ECs. Furthermore, typical models use static cell culture methods, ignoring the effect of hemodynamic forces on endothelial aging. This thesis sought to fill this gap in the research by investigating the response to shear stress of ECs in the context of vascular aging. The central hypothesis was that ECs derived from iPSCs of HGPS patients could model aged cells. As an accelerated aging disease hallmarked by atherosclerosis and fatal cardiovascular disease, HGPS has been used to learn about normal vascular aging.

The first specific aim to use a directed differentiation protocol by Sahara *et al.* to obtain ECs resulted in iPSCs from healthy donors and HGPS-iPSCs generating $CD144^{+}$ECs with only about 20% efficiency. The resulting ECs were studied using flow cytometry and vWF immunostaining to confirm their phenotype. However, they were found to have low growth and survival to cryopreservation, pointing to the need for an improved differentiation protocol for future experiments. Next, with the overarching goal of investigating the role of progerin and age-associated prelamin A accumulation on EC mechanosensitivity and the impact that may have on EC dysfunction initiating atherosclerosis, the first step was to detect the presence of progerin in ECs derived from HGPS-iPSCs. To do this, a robust staining visualization method for progerin was developed and confirmed with HGPS fibroblasts as positive controls of accumulation and healthy fibroblasts as negative controls. This thesis found that progerin was in fact accumulating in both HGPS-iPSC-ECs and slightly in healthy iPSC-ECs, which is a somewhat controversial finding since progerin has been mainly reported in VSMCs. Only two recent publications have shown similar progerin accumulation and nuclear abnormalities in HGPS-iPSC-ECs[20,138].

The second step was to expose HUVECs and HSVECs to biologically relevant shear stress by using a parallel-plate flow chamber system, previously developed by Hoesli *et al.* To assess the impact of shear stress on ECs, cytoskeletal and nuclear alignment quantification methods were developed using staining and image analysis techniques. Those experiments confirmed that under

dynamic conditions actin filaments align in the direction of the flow, and the major axis of nuclei show a similar trend of preferred orientation. One final objective consisted in determining whether inflammation in response to shear stress could be assessed using a leukocyte adhesion assay via the perfusion of NB4 cells in the flow chamber system, the quantification of inflammatory cytokines via ELISAs on media samples taken from the circulation loop and the measurement of cytotoxicity via LDH quantification. The results of these experiments demonstrated the limitations of these methods mainly due to the large volume of media required for the circulation loop. They suggested that perhaps future experiments should focus on the assessment of inflammation via immunocytochemistry of the endothelial layer from the flow chamber system.

Overall, the methods developed in this thesis can be used in combination with one another to form a successful platform to study vascular aging under hemodynamic conditions. The stage has been set for the next important step, consisting of introducing ECs derived HGPS-iPSC into the flow chamber, which was never done before. Combined with the finding that HGPS-iPSC-ECs did show some progerin accumulation, the platform developed could help shed some light into the progression of EC aging and the impact of endothelial dysfunction the response to shear-stress in the context of both HGPS and normal vascular aging, and even test medicines in the hopes of improving treatment options.

REFERENCES

1 N. Fekete, A. V. Béland, K. Campbell, S. L. Clark and C. A. Hoesli, *Transfusion*, 2018, **58**, 1800–1813.

2 C. A. Hoesli, C. Tremblay, P.-M. Juneau, M. D. Boulanger, A. V. Beland, S. D. Ling, B. Gaillet, C. Duchesne, J. Ruel, G. Laroche and A. Garnier, *ACS Biomater Sci Eng*, 2018, **4**, 3779–3791.

3 A. Wargenau, N. Fekete, A. V. Beland, G. Sabbatier, O. M. Bowden, M. D. Boulanger and C. A. Hoesli, *Colloids and Surfaces B: Biointerfaces*, 2019, **183**, 110447.

4 J.-P. Bastien, N. Fekete, A. V. Beland, M.-P. Lachambre, V. Laforte, D. Juncker, V. Dave, D.-C. Roy and C. A. Hoesli, *Journal of Translational Medicine*, 2020, **18**, 383.

5 Cardiovascular diseases (CVDs), https://www.who.int/news-room/fact-sheets/detail/cardiovascular-diseases-(cvds), (accessed February 9, 2021).

6 S. C. Government of Canada, Leading causes of death, total population, by age group, https://www150.statcan.gc.ca/t1/tbl1/en/tv.action?pid=1310039401, (accessed February 9, 2021).

7 Heart and Stroke Foundation, 2016.

8 J.-E. Tarride, M. Lim, M. DesMeules, W. Luo, N. Burke, D. O'Reilly, J. Bowen and R. Goeree, *Can J Cardiol*, 2009, **25**, e195–e202.

9 E. and S. D. Canada, Government of Canada — Action for Seniors report, https://www.canada.ca/en/employment-social-development/programs/seniors-action-report.html, (accessed February 9, 2021).

10 J. Ribas, Y. S. Zhang, P. R. Pitrez, J. Leijten, M. Miscuglio, J. Rouwkema, M. R. Dokmeci, X. Nissan, L. Ferreira and A. Khademhosseini, *Small*, 2017, **13**, 1603737.

11 M. Sawabe, *Geriatrics & Gerontology International*, 2010, **10**, S213–S220.

12 J. C. Wang and M. Bennett, *Circ Res*, 2012, **111**, 245–259.

13 M. Olive, I. Harten, R. Mitchell, J. K. Beers, K. Djabali, K. Cao, M. R. Erdos, C. Blair, B. Funke, L. Smoot, M. Gerhard-Herman, J. T. Machan, R. Kutys, R. Virmani, F. S. Collins, T. N. Wight, E. G. Nabel and L. B. Gordon, *Arterioscler Thromb Vasc Biol*, 2010, **30**, 2301–2309.

14 J. A. Brassard, N. Fekete, A. Garnier and C. A. Hoesli, *Biogerontology*, 2016, **17**, 129–145.

15 I. Bellantuono, G. Sanguinetti and W. N. Keith, *Biogerontology*, 2012, **13**, 63–75.

16 C. R. Burtner and B. K. Kennedy, *Nat Rev Mol Cell Biol*, 2010, **11**, 567–578.

17 J. Hutchinson, *Med Chir Trans*, 1886, **69**, 473–477.

18 PRF By The Numbers, https://www.progeriaresearch.org/prf-by-the-numbers/, (accessed February 9, 2021).

19 M. A. Merideth, L. B. Gordon, S. Clauss, V. Sachdev, A. C. M. Smith, M. B. Perry, C. C. Brewer, C. Zalewski, H. J. Kim, B. Solomon, B. P. Brooks, L. H. Gerber, M. L. Turner, D. L. Domingo, T. C. Hart, J. Graf, J. C. Reynolds, A. Gropman, J. A. Yanovski, M. Gerhard-Herman, F. S. Collins, E. G. Nabel, R. O. Cannon, W. A. Gahl and W. J. Introne, *N Engl J Med*, 2008, **358**, 592–604.

20 L. Atchison, N. O. Abutaleb, E. Snyder-Mounts, Y. Gete, A. Ladha, T. Ribar, K. Cao and G. A. Truskey, *Stem Cell Reports*, 2020, **14**, 325–337.

21 N. G. dela Paz and P. A. D'Amore, *Cell Tissue Res*, 2009, **335**, 5–16.

22 B. Alberts, *Molecular Biology of the Cell*, Garland Science, 2017.

23 W. C. Aird, *Circ Res*, 2007, **100**, 158–173.

24 W. A. Muller, S. A. Weigl, X. Deng and D. M. Phillips, *J Exp Med*, 1993, **178**, 449–460.

25 A. R. Schenkel, Z. Mamdouh, X. Chen, R. M. Liebman and W. A. Muller, *Nat Immunol*, 2002, **3**, 143–150.
26 G. Ostermann, K. S. C. Weber, A. Zernecke, A. Schröder and C. Weber, *Nat Immunol*, 2002, **3**, 151–158.
27 P. A. D'Amore, *Nature Medicine*, 2000, **6**, 1323–1324.
28 W. G. Roberts and G. E. Palade, *J Cell Sci*, 1995, **108 (Pt 6)**, 2369–2379.
29 T. Alon, I. Hemo, A. Itin, J. Pe'er, J. Stone and E. Keshet, *Nat Med*, 1995, **1**, 1024–1028.
30 D. T. Connolly, D. M. Heuvelman, R. Nelson, J. V. Olander, B. L. Eppley, J. J. Delfino, N. R. Siegel, R. M. Leimgruber and J. Feder, *J Clin Invest*, 1989, **84**, 1470–1478.
31 S. Soker, S. Takashima, H. Q. Miao, G. Neufeld and M. Klagsbrun, *Cell*, 1998, **92**, 735–745.
32 Z. Gluzman-Poltorak, T. Cohen, Y. Herzog and G. Neufeld, *J Biol Chem*, 2000, **275**, 18040–18045.
33 B. Millauer, S. Wizigmann-Voos, H. Schnürch, R. Martinez, N. P. Møller, W. Risau and A. Ullrich, *Cell*, 1993, **72**, 835–846.
34 A. J. Donato, R. G. Morgan, A. E. Walker and L. A. Lesniewski, *J Mol Cell Cardiol*, 2015, **89**, 122–135.
35 E. G. Lakatta, M. Wang and S. S. Najjar, *Med Clin North Am*, 2009, **93**, 583-Contents.
36 M. E. Widlansky, N. Gokce, J. F. Keaney and J. A. Vita, *Journal of the American College of Cardiology*, 2003, **42**, 1149–1160.
37 Libby Peter, Ridker Paul M., and Maseri Attilio, *Circulation*, 2002, **105**, 1135–1143.
38 C. Frantz, K. M. Stewart and V. M. Weaver, *J Cell Sci*, 2010, **123**, 4195–4200.
39 R. J. M. W. Rennenberg, A. G. H. Kessels, L. J. Schurgers, J. M. A. van Engelshoven, P. W. de Leeuw and A. A. Kroon, *Vasc Health Risk Manag*, 2009, **5**, 185–197.
40 High cholesterol - Symptoms and causes, https://www.mayoclinic.org/diseases-conditions/high-blood-cholesterol/symptoms-causes/syc-20350800, (accessed March 4, 2021).
41 M. Wang, L. Jiang, R. E. Monticone and E. G. Lakatta, *Trends Endocrinol Metab*, 2014, **25**, 72–79.
42 E. Chang and C. B. Harley, *Proc Natl Acad Sci U S A*, 1995, **92**, 11190–11194.
43 Matthews Charles, Gorenne Isabelle, Scott Stephen, Figg Nicola, Kirkpatrick Peter, Ritchie Andrew, Goddard Martin, and Bennett Martin, *Circulation Research*, 2006, **99**, 156–164.
44 E. Vasile, Y. Tomita, L. F. Brown, O. Kocher and H. F. Dvorak, *The FASEB Journal*, 2001, **15**, 458–466.
45 F. Fyhrquist, O. Saijonmaa and T. Strandberg, *Nature Reviews Cardiology*, 2013, **10**, 274–283.
46 D. J. Kurz, S. Decary, Y. Hong, E. Trivier, A. Akhmedov and J. D. Erusalimsky, *Journal of Cell Science*, 2004, **117**, 2417–2426.
47 K. N. Dahl, A. J. S. Ribeiro and J. Lammerding, *Circ Res*, 2008, **102**, 1307–1318.
48 V. Vogel and M. Sheetz, *Nat Rev Mol Cell Biol*, 2006, **7**, 265–275.
49 C. P. Johnson, H.-Y. Tang, C. Carag, D. W. Speicher and D. E. Discher, *Science*, 2007, **317**, 663–666.
50 P. A. Janmey and C. A. McCulloch, *Annu Rev Biomed Eng*, 2007, **9**, 1–34.
51 M. P. Sheetz, *Nature Reviews Molecular Cell Biology*, 2001, **2**, 392–396.
52 S. Wiesner, K. R. Legate and R. Fässler, *CMLS, Cell. Mol. Life Sci.*, 2005, **62**, 1081–1099.
53 A. L. Hazel and T. J. Pedley, *Biophys J*, 2000, **78**, 47–54.

54 G. Helmlinger, R. V. Geiger, S. Schreck and R. M. Nerem, *J Biomech Eng*, 1991, **113**, 123–131.
55 J. Zhou, Y.-S. Li and S. Chien, *Arterioscler Thromb Vasc Biol*, 2014, **34**, 2191–2198.
56 T. Dechat, S. A. Adam, P. Taimen, T. Shimi and R. D. Goldman, *Cold Spring Harb Perspect Biol*, , DOI:10.1101/cshperspect.a000547.
57 S. Osmanagic-Myers, T. Dechat and R. Foisner, *Genes Dev*, 2015, **29**, 225–237.
58 E. A. Booth-Gauthier, T. A. Alcoser, G. Yang and K. N. Dahl, *Biophys J*, 2012, **103**, 2423–2431.
59 Q. Lan, K. O. Mercurius and P. F. Davies, *Biochem Biophys Res Commun*, 1994, **201**, 950–956.
60 J. Hoffmann, J. Haendeler, A. Aicher, L. Rössig, M. Vasa, A. M. Zeiher and S. Dimmeler, *Circ Res*, 2001, **89**, 709–715.
61 C. Kriesi, M. Steinert, A. Marmaras, C. Danzer, V. Meskenaite and V. Kurtcuoglu, *Front Bioeng Biotechnol*, , DOI:10.3389/fbioe.2019.00091.
62 D. P. Bakker, A. van der Plaats, G. J. Verkerke, H. J. Busscher and H. C. van der Mei, *Appl. Environ. Microbiol.*, 2003, **69**, 6280–6287.
63 J. A. McCann, S. D. Peterson, M. W. Plesniak, T. J. Webster and K. M. Haberstroh, *Ann Biomed Eng*, 2005, **33**, 328.
64 K. K. McDonald, S. Cooper, L. Danielzak and R. L. Leask, *PLoS One*, 2016, **11**, e0167576.
65 Directionality, https://imagej.net/Directionality, (accessed March 9, 2021).
66 ImageJ Analyze Menu, https://imagej.nih.gov/ij/docs/menus/analyze.html, (accessed March 31, 2021).
67 R. D. Goldman, D. K. Shumaker, M. R. Erdos, M. Eriksson, A. E. Goldman, L. B. Gordon, Y. Gruenbaum, S. Khuon, M. Mendez, R. Varga and F. S. Collins, *Proc Natl Acad Sci U S A*, 2004, **101**, 8963–8968.
68 S. Kõks, S. Dogan, B. G. Tuna, H. González-Navarro, P. Potter and R. E. Vandenbroucke, *Mech Ageing Dev*, 2016, **160**, 41–53.
69 S. Drechsler, M. A. Lynch, S. Novella, H. González-Navarro, S. Hecimovic, E. Barini, V. Tucci, R. E. Castro, R. E. Vandenbroucke, M. Osuchowski and P. K. Potter, *Mechanisms of Ageing and Development*, 2016, **160**, 54–68.
70 S. Novella, A. P. Dantas, G. Segarra, X. Vidal-Gómez, A. Mompeón, M. Garabito, C. Hermenegildo and P. Medina, *Experimental Gerontology*, 2013, **48**, 1329–1337.
71 H. Liao, H. He, Y. Chen, F. Zeng, J. Huang, L. Wu and Y. Chen, *Cytotechnology*, 2014, **66**, 229–238.
72 Pearson Thomas A., Mensah George A., Alexander R. Wayne, Anderson Jeffrey L., Cannon Richard O., Criqui Michael, Fadl Yazid Y., Fortmann Stephen P., Hong Yuling, Myers Gary L., Rifai Nader, Smith Sidney C., Taubert Kathryn, Tracy Russell P., and Vinicor Frank, *Circulation*, 2003, **107**, 499–511.
73 Libby Peter and Ridker Paul M., *Circulation*, 1999, **100**, 1148–1150.
74 H. Alsaffar, N. Martino, J. P. Garrett and A. P. Adam, *American Journal of Physiology-Cell Physiology*, 2018, **314**, C589–C602.
75 N. C. Kirkiles-Smith, K. Mahboubi, J. Plescia, J. M. McNiff, J. Karras, J. S. Schechner, D. C. Altieri and J. S. Pober, *The Journal of Immunology*, 2004, **172**, 1391–1396.
76 A. Orazi, X. Du, Z. Yang, M. Kashai and D. A. Williams, *Lab Invest*, 1996, **75**, 33–42.
77 K. Mahboubi, B. C. Biedermann, J. M. Carroll and J. S. Pober, *J Immunol*, 2000, **164**, 3837–3846.

78 F. K.-M. Chan, K. Moriwaki and M. J. De Rosa, in *Immune Homeostasis: Methods and Protocols*, eds. A. L. Snow and M. J. Lenardo, Humana Press, Totowa, NJ, 2013, pp. 65–70.
79 H. Gilford, *Practitioner*, 1904, 188–217.
80 R. C. M. Hennekam, *Am J Med Genet A*, 2006, **140**, 2603–2624.
81 D. McClintock, D. Ratner, M. Lokuge, D. M. Owens, L. B. Gordon, F. S. Collins and K. Djabali, *PLoS One*, 2007, **2**, e1269.
82 A. E. Rusiñol and M. S. Sinensky, *J Cell Sci*, 2006, **119**, 3265–3272.
83 A. De Sandre-Giovannoli, R. Bernard, P. Cau, C. Navarro, J. Amiel, I. Boccaccio, S. Lyonnet, C. L. Stewart, A. Munnich, M. Le Merrer and N. Lévy, *Science*, 2003, **300**, 2055.
84 M. Eriksson, W. T. Brown, L. B. Gordon, M. W. Glynn, J. Singer, L. Scott, M. R. Erdos, C. M. Robbins, T. Y. Moses, P. Berglund, A. Dutra, E. Pak, S. Durkin, A. B. Csoka, M. Boehnke, T. W. Glover and F. S. Collins, *Nature*, 2003, **423**, 293–298.
85 A. Kalinowski, P. N. Yaron, Z. Qin, S. Shenoy, M. J. Buehler, M. Lösche and K. N. Dahl, *Biophys Chem*, 2014, **195**, 43–48.
86 Z. Qin, A. Kalinowski, K. N. Dahl and M. J. Buehler, *J Struct Biol*, 2011, **175**, 425–433.
87 A. I. Caplan, *J Orthop Res*, 1991, **9**, 641–650.
88 Gordon Leslie B., Kleinman Monica E., Massaro Joe, D'Agostino Ralph B., Shappell Heather, Gerhard-Herman Marie, Smoot Leslie B., Gordon Catherine M., Cleveland Robert H., Nazarian Ara, Snyder Brian D., Ullrich Nicole J., Silvera V. Michelle, Liang Marilyn G., Quinn Nicolle, Miller David T., Huh Susanna Y., Dowton Anne A., Littlefield Kelly, Greer Maya M., and Kieran Mark W., *Circulation*, 2016, **134**, 114–125.
89 The day has come, https://www.progeriaresearch.org/2020/11/20/fda-approval/, (accessed March 6, 2021).
90 Zokinvy (lonafarnib) - Now FDA Approved, https://www.zokinvy.com/, (accessed March 6, 2021).
91 PubChem, Lonafarnib, https://pubchem.ncbi.nlm.nih.gov/compound/148195, (accessed March 6, 2021).
92 A. Ocampo, P. Reddy, P. Martinez-Redondo, A. Platero-Luengo, F. Hatanaka, T. Hishida, M. Li, D. Lam, M. Kurita, E. Beyret, T. Araoka, E. Vazquez-Ferrer, D. Donoso, J. L. Roman, J. Xu, C. Rodriguez Esteban, G. Nuñez, E. Nuñez Delicado, J. M. Campistol, I. Guillen, P. Guillen and J. C. Izpisua Belmonte, *Cell*, 2016, **167**, 1719-1733.e12.
93 L. W. Koblan, M. R. Erdos, C. Wilson, W. A. Cabral, J. M. Levy, Z.-M. Xiong, U. L. Tavarez, L. M. Davison, Y. G. Gete, X. Mao, G. A. Newby, S. P. Doherty, N. Narisu, Q. Sheng, C. Krilow, C. Y. Lin, L. B. Gordon, K. Cao, F. S. Collins, J. D. Brown and D. R. Liu, *Nature*, 2021, **589**, 608–614.
94 Arteriosclerosis / atherosclerosis - Symptoms and causes, https://www.mayoclinic.org/diseases-conditions/arteriosclerosis-atherosclerosis/symptoms-causes/syc-20350569, (accessed March 6, 2021).
95 P. Scaffidi and T. Misteli, *Science*, 2006, **312**, 1059–1063.
96 K. Cao, C. D. Blair, D. A. Faddah, J. E. Kieckhaefer, M. Olive, M. R. Erdos, E. G. Nabel and F. S. Collins, *J Clin Invest*, 2011, **121**, 2833–2844.
97 C. D. Ragnauth, D. T. Warren, Y. Liu, R. McNair, T. Tajsic, N. Figg, R. Shroff, J. Skepper and C. M. Shanahan, *Circulation*, 2010, **121**, 2200–2210.
98 E. A. Booth, S. T. Spagnol, T. A. Alcoser and K. N. Dahl, *Soft Matter*, 2015, **11**, 6412–6418.

99 K. N. Dahl, P. Scaffidi, M. F. Islam, A. G. Yodh, K. L. Wilson and T. Misteli, *PNAS*, 2006, **103**, 10271–10276.
100 E. A. Booth-Gauthier, V. Du, M. Ghibaudo, A. D. Rape, K. N. Dahl and B. Ladoux, *Integr Biol (Camb)*, 2013, **5**, 569–577.
101 J. Lammerding, P. C. Schulze, T. Takahashi, S. Kozlov, T. Sullivan, R. D. Kamm, C. L. Stewart and R. T. Lee, *J Clin Invest*, 2004, **113**, 370–378.
102 M. J. Evans and M. H. Kaufman, *Nature*, 1981, **292**, 154–156.
103 K. Takahashi and S. Yamanaka, *Cell*, 2006, **126**, 663–676.
104 S. Yamanaka and H. M. Blau, *Nature*, 2010, **465**, 704–712.
105 J. Zhang, Q. Lian, G. Zhu, F. Zhou, L. Sui, C. Tan, R. A. Mutalif, R. Navasankari, Y. Zhang, H.-F. Tse, C. L. Stewart and A. Colman, *Cell Stem Cell*, 2011, **8**, 31–45.
106 J. C. Ho, T. Zhou, W.-H. Lai, Y. Huang, Y.-C. Chan, X. Li, N. L. Wong, Y. Li, K.-W. Au, D. Guo, J. Xu, C.-W. Siu, D. Pei, H.-F. Tse and M. A. Esteban, *Aging (Albany NY)*, 2011, **3**, 380–390.
107 G.-H. Liu, B. Z. Barkho, S. Ruiz, D. Diep, J. Qu, S.-L. Yang, A. D. Panopoulos, K. Suzuki, L. Kurian, C. Walsh, J. Thompson, S. Boue, H. L. Fung, I. Sancho-Martinez, K. Zhang, J. Yates and J. C. I. Belmonte, *Nature*, 2011, **472**, 221–225.
108 B. Zuo, J. Yang, F. Wang, L. Wang, Y. Yin, J. Dan, N. Liu and L. Liu, *Biol Open*, 2012, **1**, 1118–1127.
109 D. Constantinescu, H. L. Gray, P. J. Sammak, G. P. Schatten and A. B. Csoka, *STEM CELLS*, 2006, **24**, 177–185.
110 A. Banito, S. T. Rashid, J. C. Acosta, S. Li, C. F. Pereira, I. Geti, S. Pinho, J. C. Silva, V. Azuara, M. Walsh, L. Vallier and J. Gil, *Genes Dev*, 2009, **23**, 2134–2139.
111 P. Scaffidi and T. Misteli, *Nat Cell Biol*, 2008, **10**, 452–459.
112 S. Chiba, *STEM CELLS*, 2006, **24**, 2437–2447.
113 D. James, H. Nam, M. Seandel, D. Nolan, T. Janovitz, M. Tomishima, L. Studer, G. Lee, D. Lyden, R. Benezra, N. Zaninovic, Z. Rosenwaks, S. Y. Rabbany and S. Rafii, *Nat Biotechnol*, 2010, **28**, 161–166.
114 S. Levenberg, J. S. Golub, M. Amit, J. Itskovitz-Eldor and R. Langer, *Proc Natl Acad Sci U S A*, 2002, **99**, 4391–4396.
115 K.-D. Choi, J. Yu, K. Smuga-Otto, G. Salvagiotto, W. Rehrauer, M. Vodyanik, J. Thomson and I. Slukvin, *Stem Cells*, 2009, **27**, 559–567.
116 M. Sahara, E. M. Hansson, O. Wernet, K. O. Lui, D. Später and K. R. Chien, *Cell Res*, 2014, **24**, 820–841.
117 C. Patsch, L. Challet-Meylan, E. C. Thoma, E. Urich, T. Heckel, J. F. O'Sullivan, S. J. Grainger, F. G. Kapp, L. Sun, K. Christensen, Y. Xia, M. H. C. Florido, W. He, W. Pan, M. Prummer, C. R. Warren, R. Jakob-Roetne, U. Certa, R. Jagasia, P.-O. Freskgård, I. Adatto, D. Kling, P. Huang, L. I. Zon, E. L. Chaikof, R. E. Gerszten, M. Graf, R. Iacone and C. A. Cowan, *Nat Cell Biol*, 2015, **17**, 994–1003.
118 R. Tatsumi, Y. Suzuki, T. Sumi, M. Sone, H. Suemori and N. Nakatsuji, *Cell Transplant*, 2011, **20**, 1423–1430.
119 A. J. Rufaihah, N. F. Huang, J. Kim, J. Herold, K. S. Volz, T. S. Park, J. C. Lee, E. T. Zambidis, R. Reijo-Pera and J. P. Cooke, *Am J Transl Res*, 2013, **5**, 21–35.
120 N. Prasain, M. R. Lee, S. Vemula, J. L. Meador, M. Yoshimoto, M. J. Ferkowicz, A. Fett, M. Gupta, B. M. Rapp, M. R. Saadatzadeh, M. Ginsberg, O. Elemento, Y. Lee, S. L. Voytik-

Harbin, H. M. Chung, K. S. Hong, E. Reid, C. L. O'Neill, R. J. Medina, A. W. Stitt, M. P. Murphy, S. Rafii, H. E. Broxmeyer and M. C. Yoder, *Nat Biotechnol*, 2014, **32**, 1151–1157.
121 Orlova Valeria V., Drabsch Yvette, Freund Christian, Petrus-Reurer Sandra, van den Hil Francijna E., Muenthaisong Suchitra, Dijke Peter ten, and Mummery Christine L., *Arteriosclerosis, Thrombosis, and Vascular Biology*, 2014, **34**, 177–186.
122 G. Sriram, J. Y. Tan, I. Islam, A. J. Rufaihah and T. Cao, *Stem Cell Res Ther*, , DOI:10.1186/s13287-015-0260-5.
123 T. Q. Crawford and H. Roelink, *Dev Dyn*, 2007, **236**, 886–892.
124 W. M. Schopperle and W. C. DeWolf, *Stem Cells*, 2007, **25**, 723–730.
125 CD34 - an overview | ScienceDirect Topics, https://www.sciencedirect.com/topics/biochemistry-genetics-and-molecular-biology/cd34, (accessed March 3, 2021).
126 L. E. Sidney, M. J. Branch, S. E. Dunphy, H. S. Dua and A. Hopkinson, *Stem Cells*, 2014, **32**, 1380–1389.
127 L. Pierelli, G. Bonanno, S. Rutella, M. Marone, G. Scambia and G. Leone, *Leuk Lymphoma*, 2001, **42**, 1195–1206.
128 R. V. Hoch and P. Soriano, *Development*, 2003, **130**, 4769–4784.
129 K. A. Fitzgerald, L. A. J. O'Neill, A. J. H. Gearing and R. E. Callard, *The Cytokine Factsbook and Webfacts*, Elsevier, 2001.
130 P. J. Newman and D. K. Newman, *Arterioscler Thromb Vasc Biol*, 2003, **23**, 953–964.
131 Leroyer Aurélie S., Blin Muriel G., Bachelier Richard, Bardin Nathalie, Blot-Chabaud Marcel, and Dignat-George Françoise, *Arteriosclerosis, Thrombosis, and Vascular Biology*, 2019, **39**, 1026–1033.
132 K. Holmes, O. L. Roberts, A. M. Thomas and M. J. Cross, *Cellular Signalling*, 2007, **19**, 2003–2012.
133 D. Vestweber, *Arterioscler Thromb Vasc Biol*, 2008, **28**, 223–232.
134 F. Peyvandi, I. Garagiola and L. Baronciani, *Blood Transfus*, 2011, **9**, s3–s8.
135 Available Cell Lines, https://www.progeriaresearch.org/available-cell-lines/, (accessed February 24, 2021).
136 C. A. Hoesli, A. Garnier, P.-M. Juneau, P. Chevallier, C. Duchesne and G. Laroche, *Biomaterials*, 2014, **35**, 879–890.
137 S. J. Lord, K. B. Velle, R. D. Mullins and L. K. Fritz-Laylin, *Journal of Cell Biology*, , DOI:10.1083/jcb.202001064.
138 G. Matrone, R. A. Thandavarayan, B. K. Walther, S. Meng, A. Mojiri and J. P. Cooke, *Cell Cycle*, 2019, **18**, 2495–2508.
139 S. Seo, H. Fujita, A. Nakano, M. Kang, A. Duarte and T. Kume, *Dev Biol*, 2006, **294**, 458–470.
140 L.-R. You, F.-J. Lin, C. T. Lee, F. J. DeMayo, M.-J. Tsai and S. Y. Tsai, *Nature*, 2005, **435**, 98–104.
141

APPENDICES

APPENDIX A – ARTERIOVENOUS SPECIFICATION

Specification to the arterial fate was found to be initiated by Sonic hedgehog in mice and zebrafish experiments[21]. In zebrafish specifically, fetal liver kinase 1-positive angioblasts migrate to the midline when Shh is secreted by cells in the notochord and the floor plate and when vascular endothelial growth factor (VEGF or VEGF-A) is expressed by the somites[21]. VEGF is the main signalling molecule in the endothelium. It is an endothelial mitogen and angiogenic factor, in addition to stimulating EC migration and survival, as well as controlling vessel permeability via the induction and maintenance of fenestrations[21,28–30]. VEGF is known to bind to two main receptor tyrosine kinases: fms-like tyrosine kinase 1 (or VEGFR1) and most importantly Flk1 or VEGFR2; as well as two non-tyrosine kinases receptors: neuropilin-1 and neuropilin-2 [21,31–33]. Interestingly, in hypoxic conditions, almost every type of cell in the body increases levels of hypoxia-induced factor 1α, a transcription factor stimulating the transcription of VEGF[22]. Following this signal, angiogenesis can take place when each new vessel originates from a capillary sprout, where endothelial *tip cells* lead the way[22]. Returning to embryonic development, VEGF signaling via the VEGFR2/NP-1 complex leads to the activation of Notch and extracellular signal-regulated kinases signaling pathways[21]. The signals for transcriptional regulation of EC specification are complex but a few key markers have been investigated. For instance, activator protein 1 binding site was identified as a promoter for the Notch4 gene in humans and Forkhead box c 1 and 2 have been found to regulate arterial cell specification upstream of Notch signaling[21,139].

In venous fate specification, a member of the orphan nuclear receptor superfamily called COUP-TFII is expressed[140]. This inhibits NP-1, part of the VEGFR2/NP-1, thus supressing the Notch signalling pathway and leading to venous EC identity[21]. Additionally, phosphatidylinositiol-3 kinase (PI3K/Akt, Akt standing for protein kinase B) signaling blocks mitogen-activated protein kinase (ERK) pathway activation, essentially promoting venous fate.

These pathways are summarized in **Figure S1**.

APPENDIX B – SUPPLEMENTARY FIGURES

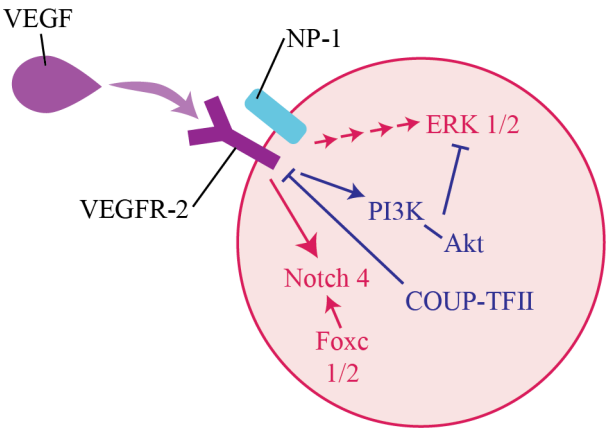

Figure S1: *Schematic of arteriovenous specification* by the developmental expression of different genes encoding ligands, receptors and transcriptional factors adapted from dela Paz and D'Amore[21]. In pink is summarized the main factors involved in arterial fate specification, and in blue the ones promoting venous fate

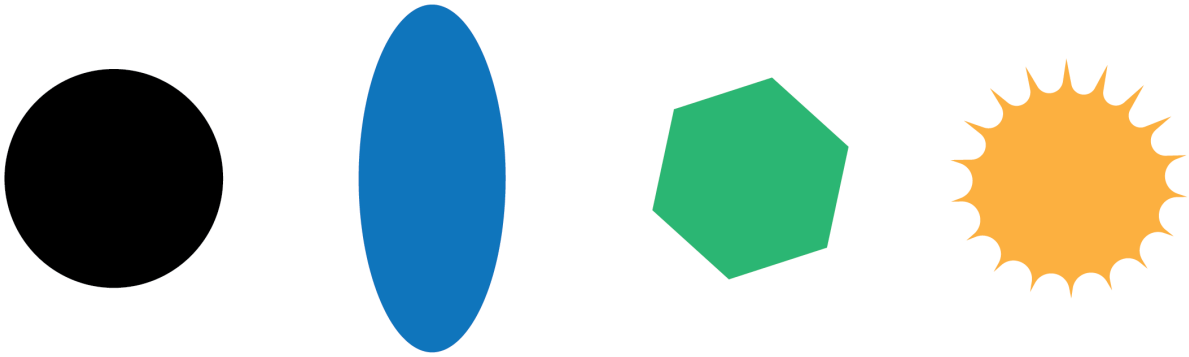

Circularity ~1 Roundness ~1	Circularity ~0.7 Roundness ~0.5	Circularity ~0.8 Roundness ~1	Circularity ~0.1 Roundness ~1

Figure S2: *Schematic demonstrating the impact of shape changes on the values for circularity and roundness. The images were fed to ImageJ and analyzed using the Particle Analysis tool.*

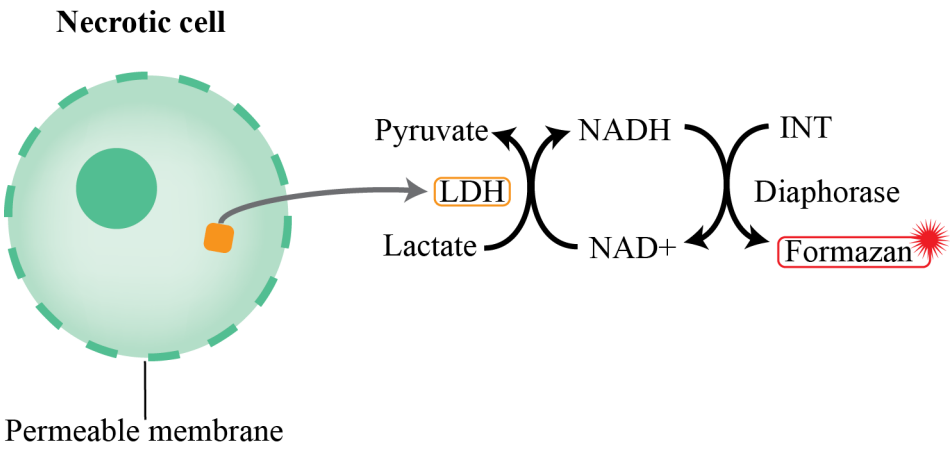

Figure S3: *Schematic of the coupled enzymatic reaction behind cytotoxicity assay detecting the leakage of the soluble LDH enzyme in the cytosol. LDH produces reduced nicotinamide adenine dinucleotide (NADH) as it catalyzes the oxidation of lactate to pyruvate*[78,141]*. This reaction can be detected calorimetrically at 490nm due to the accumulation of a red formazan product created when INT, a tetrazolium salt, is reduced by diaphorase using NADH*[78,141]*. The figure is adapted from Thermo Scientific Thermo Scientific*[141]*.*

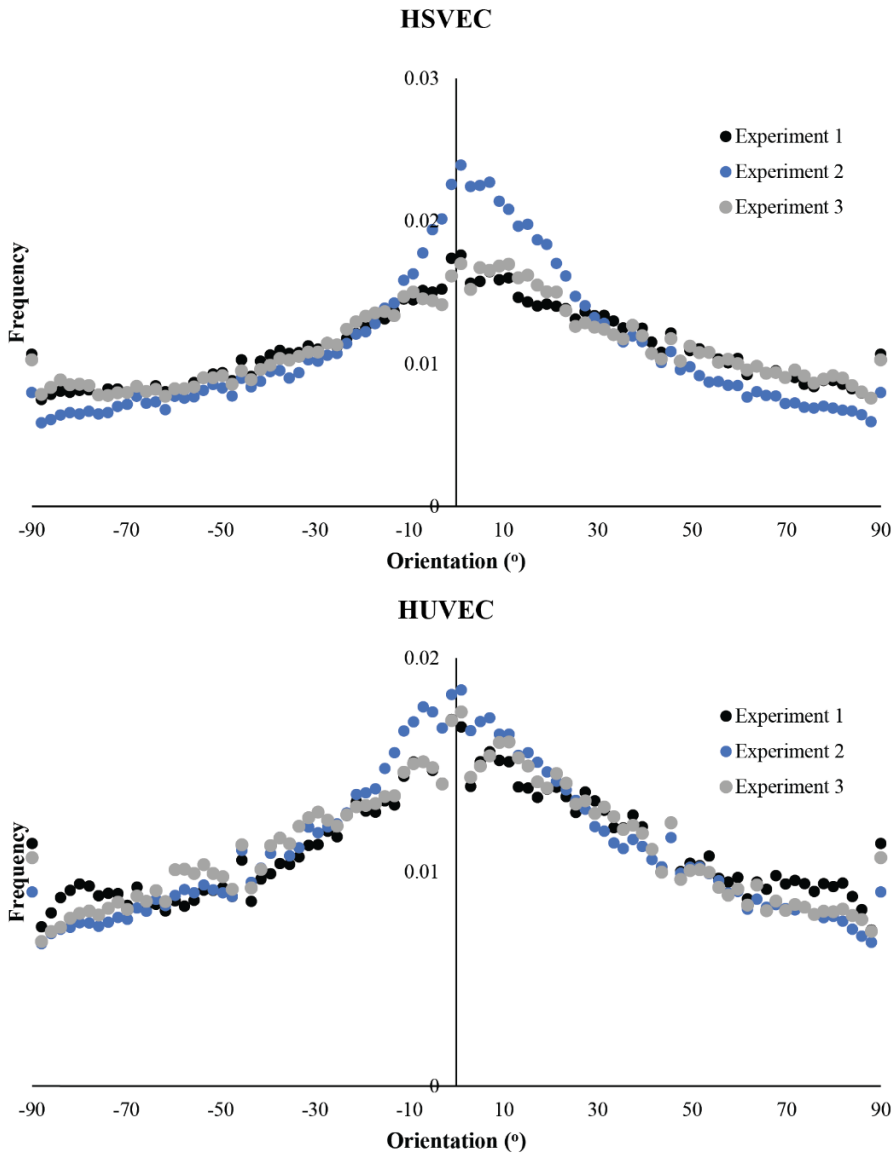

Figure S4: *Graphs comparing the extent of actin filament alignment between biological triplicates for both HSVECs and HUVECs.The similarity between triplicate experiments, especially for HUVECs indicates that the staining protocol and subsequent use of Directinality in ImageJ™ give reproducible results to quantify cytoskeletal alignment.*

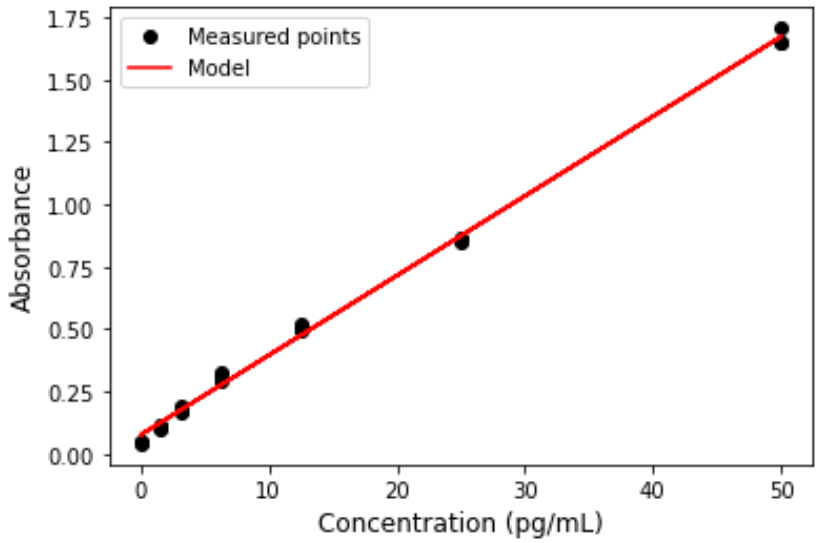

Figure S5: *IL-6 calibration curve from ELISA. First order equation:* $absorbance = 0.03193[concentration] + 0.07528$ *with a coefficient of determination* R^2 *of 0.997.*

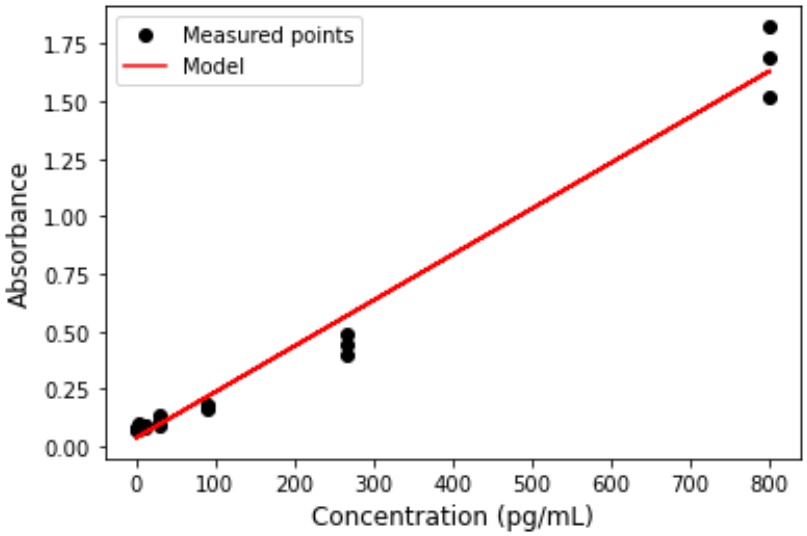

Figure S6: *IL-11 calibration curve from ELISA. First order equation* $absorbance = 0.001991[concentration] + 0.038299$ *with a coefficient of determination* R^2 *of 0.98.*